Fall 2014

Treatment plan optimization for rotating-shield brachytherapy

Yunlong Liu
University of Iowa

Recommended Citation

Liu, Yunlong. "Treatment plan optimization for rotating-shield brachytherapy." PhD (Doctor of Philosophy) thesis, University of Iowa, 2014.
https://doi.org/10.17077/etd.bs4adro4

Follow this and additional works at: https://ir.uiowa.edu/etd
Part of the Electrical and Computer Engineering Commons

TREATMENT PLAN OPTIMIZATION FOR ROTATING-SHIELD BRACHYTHERAPY

by

Yunlong Liu

A thesis submitted in partial fulfillment of the
requirements for the Doctor of Philosophy
degree in Electrical and Computer Engineering
in the Graduate College of
The University of Iowa

May 2014

Thesis Supervisor: Associate Professor Xiaodong Wu

Graduate College
The University of Iowa
Iowa City, Iowa

CERTIFICATE OF APPROVAL

PH.D. THESIS

This is to certify that the Ph.D. thesis of

Yunlong Liu

has been approved by the Examining Committee for the thesis requirement for the Doctor of Philosophy degree in Electrical and Computer Engineering at the May 2014 graduation.

Thesis Committee: ______________________
Xiaodong Wu, Thesis Supervisor

____
Ryan T. Flynn

____
Erwei Bai

____
Mona K. Garvin

____
Hantao Zhang

I dedicate this thesis to my wife, my daughter and my parents. The completion of this work would not have been possible without their love, understanding and support.

ACKNOWLEDGEMENTS

I sincerely thank my advisor Dr. Xiaodong Wu for his continuous guidance and support throughout my Ph.D. study at University of Iowa. I would also like to thank Dr. Ryan T. Flynn and Dr. Yusung Kim from the Department of Radiation Oncology, University of Iowa Hospital and Clinics for imparting to me their broad view of research in the intensity-modulated brachytherapy.

The environment at University of Iowa has been immensely supportive. I have benefited from the interactions with many of the faculty members here, including Dr. Hantao Zhang, Dr. Weiyu Xu, Dr. Milan Sonka, Dr. Soura Dasgupta, Dr. Jon Kuhl, Dr. Mona Garvin and Dr. Mathews Jacob. I would also like to thank Dina Blanc and Cathy Kern from the Electrical and Computer Engineering Department for their help through my life of study at University of Iowa. And I would like to thank Gareth Smith the Radiation Oncology Department who proofread several my publications.

Special thanks go to Dr. Ryan T. Flynn, Dr. Erwei Bai, Dr. Mona Garvin and Dr. Hantao Zhang, who served on my defense committee.

Part of the research results presented in this thesis represents a joint work between the Department of Electrical and Computer Engineering and the Department of Radiation Oncology, University of Iowa.

This research was supported in part by the NSF grant CCF-0844765 and the NIH grant K25-CA123112.

ABSTRACT

In this thesis, we aim to develop fundamentally new techniques and algorithms for efficiently computing rotating-shield brachytherapy (RSBT) treatment plans. We propose that these algorithms will pave the way for making RSBT available in clinical practices.

RSBT is an intensity modulated high-dose-rate brachytherapy (HDR-BT) technique. Theoretically, RSBT offers advantages over the conventional HDR-BT. Although this technique is promising in theory, its application in practice is still at an early stage. The RSBT technique entails rotating a radiation-attenuating shield about a brachytherapy source to directionally modulate the radiation in an optimized fashion. The unshielded brachytherapy source used in conventional HDR-BT delivers radially symmetric dose distributions, thus the intensity modulation capability of the conventional HDR-BT is limited. With the capability of making anisotropic radiation, RSBT will revolutionize the brachytherapy technique through superior dose conformity, increased flexibility and inherent accuracy. Due to the enhanced power of intensity-modulation, RSBT will also enable dose escalation without increasing toxicity to the organs-at-risk, thus improving quality of life for millions of cancer patients.

Although the first conceptual RSBT method was proposed more than ten years ago, there are still tremendous challenges for applying it in clinical practices. Creating efficient and automated treatment planning system is one of the major

technical obstacles for making RSBT deliverable in the clinic. The time-critical nature of the application significantly increases the difficulty of RSBT treatment planning, demanding innovative techniques for information integration. Therefore, we propose that fundamentally novel technology and algorithms for RSBT treatment planning can make RSBT clinically accessible.

The fundamental concept used for this thesis is to decompose the dose optimization step for RSBT treatment planning into two steps, namely anchor plan optimization and optimal sequencing. The degree of freedom in anchor plan optimization is controlled at a low level compared to single-step dose optimization, and the optimal sequencing algorithms can efficiently calculate treatment plans by reusing the solutions from anchor plan optimization. Thus, by decomposing the dose optimization, the computational complexity in the two-step method is greatly reduced compared to the single-step method. In the anchor plan optimization, an abstract RSBT delivery model is assumed. The abstract RSBT delivery model assumes that only beams with fixed small azimuthal emission angle, which are called beamlets, will be used during the delivery. An anchor plan is created based on this assumption that only these beamlets will be used. Generally, an anchor plan will be of high quality in the sense of dose distribution, but of low quality in the sense that it has prohibitory long delivery time. In the optimal sequencing step, beamlets will be superposed into beams to reduce the delivery time. By limiting the delivery time to a clinically acceptable level, the anchor plans turn into deliverable plans. Unlike anchor plan optimization, where an abstract RSBT delivery model is assumed, the optimal sequencing step depends on more concrete RSBT delivery models. Specifically, we will study three methods of RSBT, namely the single rotating-shield brachytherapy (S-RSBT), the dynamic rotating-shield brachytherapy (D-RSBT) and the paddle rotating-shield brachytherapy (P-RSBT).

We proposed a novel anchor plan dose optimization method as well as novel optimal sequencing methods for each of the RSBT delivery methods studied in this work. We have implemented all the proposed algorithms and experimented with them using real medical data. With the methods proposed in this thesis, the optimization time for creating delivery plans can be controlled within 15 minutes based on the data from our experiments. Compared to the conventional brachytherapy techniques, the three methods studied in this work can produce more conformal dose distributions at an acceptable level of delivery time increase. With 15 min/fx delivery time, S-RSBT, D-RSBT and P-RSBT averagely increased the D_{90}(the minimum dose received by the hottest 90% of the tumor) by 17, 9 and 5 Gy compared to conventional interstitial plus intracavitary brachytherapy, whose D_{90} is 79 Gy. The best choice depends on the specified delivery time or quality requirement, as well as the complexity of building the equipment. Roughly speaking, among the three RSBT methods studied in this thesis, P-RSBT has the most complex applicators as well as the highest plan qualities. S-RSBT has the simplest applicators, and its plan qualities is generally better than D-RSBT with limited delivery time ($<$ 20 min/fx). With sufficient delivery time ($\sim$ 30 min/fx), D-RSBT may be considered as the best solution in the sense of balancing the complexity of applicators and the dose qualities.

TABLE OF CONTENTS

LIST OF TABLES

Table

LIST OF FIGURES

Figure

CHAPTER 1
INTRODUCTION

The study of numerical and combinatorial optimization problems have been a key issue in the treatment planning area of radiation therapy. [30] This is becoming a significant research area as more and more newly proposed treatment techniques come into the field of radiation therapy. While the optimization problems in the external beam radiation therapy (EBRT) field are relatively well-studied, many medical publications in the brachytherapy field call for effective and efficient algorithmic solutions for various discrete or continuous optimization problems related to inverse planning. [15, 51] In this thesis, we study a number of numerical and combinatorial optimization problems identified in the research of *intensity-modulated brachytherapy* (IMBT). More specifically, these problems arise in the study of treatment planning for *rotating-shield brachytherapy* (RSBT), which is an advanced technique of IMBT. [15, 16, 51, 38, 37, 39, 73].

1.1 Overview of brachytherapy and high-dose-rate brachytherapy

Brachytherapy, which is also known as internal radiation therapy, is a form of radiation therapy. In contrast to the external radiation therapy (EBRT) (Figure 1.1(a)), which is the most common form of radiation therapy with radiation emitted outside body, the radiation source in brachytherapy is placed inside or next to the area requiring treatment (Figure 1.1(b)–(g)).

Depending on the dose rates, brachytherapy can be further classified into three categories [60, 7]: (i) low dose rate (LDR) where the dose rate is 0.4-2 Gy$\cdot$h^{-1} (Figure 1.1(b)). (ii) median dose rate (MDR) where the dose rate is 2-12 Gy$\cdot$h^{-1}. (iii) brachytherapy with dose rate higher than 12 Gy$\cdot$h^{-1} are considered as high dose rate brachytherapy (HDR-BT).

By using radiation sources that travel through intracavitary or interstitial catheters (Figure 1.1(c)–(g)), HDR-BT circumvents several drawbacks in the EBRT practices: (i) the area requiring treatment is variable day-to-day due to patient set-up and organ motion, and (ii) deposition of radiation into neighboring normal tissues before it reaches the target volume (a.k.a entrance dose).

However, like all other radiation therapy techniques, the dose conformity is important for brachytherapy as well. In the recent decade, the imaging revolution with ultrasound, computed tomography (CT) and magnetic resonance imaging (MRI) shifted the paradigm of the EBRT. [23] The progress of the medical imaging makes it possible to achieve more precise quality control over the treatment procedure. Thus, achieving more conforming dose distributions to the tumor and healthy structures becomes possible and desired. [14, 9, 12, 11]

With the support from imaging and modern computer technology, EBRT using sophisticated intensity modulation, such as 3D conformal radiation therapy (3DCRT) [6] and intensity modulated radiation therapy (IMRT) [21] nowadays increasingly forms an essential integral part of daily practice in a radiation oncology department. On the other hand, the intensity modulation technique in the field of brachytherapy has also been studied in several difference cancer sites including

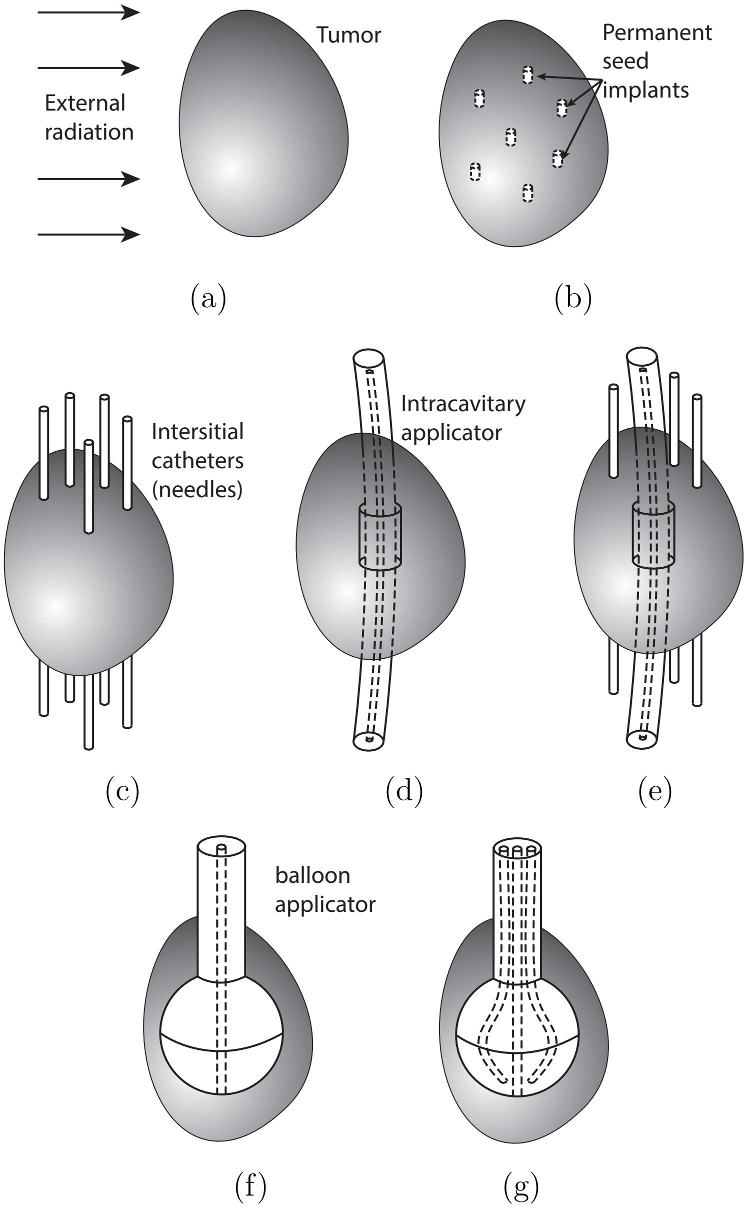

Figure 1.1: Radiation therapy techniques. (a) External radiation therapy. (b)Brachytherapy with permanent implants. (c) Brachytherapy with multiple interstitial catheters. (d) Brachytherapy with single catheter and single intracavitary applicator. (e) Interstitial plus intracavitary brachytherapy. (f) Brachytherapy with single-catheter balloon applicator. (g) Brachytherapy with multiple-catheter balloon applicator.

breast, [62, 2, 41] prostate, [42, 55, 55] and cervical cancer [12, 29, 57, 36] cases. However, compared to EBRT, the intensity modulation in brachytherapy is still on its early stage. [22] In the conventional HDR-BT, the dose distributions of the radiation sources are radially symmetric about the catheter axis, [30, 25] the dose that can be delivered to the target is limited by the surrounding organs-at-risk, especially in cases where the tumor is bulky (> 40 cm^3), laterally-extended, or non-symmetric. [46, 13, 57]

There have been several methods proposed to overcome this difficulty. For bulky tumors, the use of additional EBRT to the target for conventional intracavitary brachytherapy (ICBT) is an option recommended by the American Brachytherapy Society (ABS). However, due to the difficulties of accounting the dose with the presence of the ICBT applicators, the International MRI-Guided Brachytherapy for Locally Advanced Cervical Cancer (EMBRACE) protocol recommends against the use of parametrical EBRT boost for patients treated with MRI-guided, conformal brachytherapy. The use of interstitial brachytherapy (ISBT) is another option recommended by ABS. [61] By means of using supplementary interstitial brachytherapy plus ICBT (IS+ICBT), [13, 33, 56, 29] these applicators enables the enhanced tumor coverage under MRI-guidance. Yet, at the cost of more invasive treatment due to the presence of interstitial needles. And, even if the number of catheters, locations of catheters and source dwell times are computed in an optimized fashion, the resulting dose distributions will be still subject to the constraint that the source emits radially-symmetric dose distributions.

1.2 Overview of rotating-shield brachytherapy

Compared to the invasive or limited-capability intensity modulation techniques used in conventional HDR-BT, RSBT provides a new way of achieving more conformal dose to the targeted tumor with less invasive procedure. By using radially anisotropic sources instead of isotropic ones, RSBT delivers through shielded and rotating catheters, which results in unprecedented control over radiation dose distributions by removing the constraint that dose distributions have to be radially-symmetric about each individual catheter. [15, 51, 39]

In an RSBT delivery, the radiation source is placed in sequence along the tandem path longitudinally with distance between dwell positions of $\Delta\lambda$. At each dwell position, the shield is rotated about the center of the applicator axis. After a full rotation at one dwell position, the source moves with the shield to the next dwell position along the path and repeat the delivery process. By partially shielding the radiation source and creating directional high-dose-regions, the shield is capable of azimuthally modulating the dose intensity.

In this thesis, we consider three different way of partially shielding the source for RSBT, namely single rotating-shield brachytherapy (S-RSBT), dynamic rotating-shield brachytherapy (D-RSBT) and paddle rotating-shield brachytherapy (P-RSBT). These three methods have different ability to do the intensity modulation, as well as different complexities to manufacturing the delivery systems. Thus, the best choice may vary depending on the delivery time requirements, the dose quality requirements, and the cost requirements.

1.2.1 Single rotating-shield brachytherapy

Single rotating-shield brachytherapy (S-RSBT) is the first form of rotating-shield brachytherapy (RSBT) that have been proposed [15] and it is the most intensively studied one [16, 51, 73, 39]. It has been studied with single-catheter [15] and multi-catheter [16], with 2D [15] and 3D [51] treatments, also with cervical cancers [73] and rectal cancers [67].

Among the three methods that are going to be studied in this thesis, the applicator model of S-RSBT is the simplest. Conceptually, S-RSBT requires only a single rotatable shield with a fixed azimuthal emission angle $\Delta\varphi$ (Figure 1.2). However, due to the different shape of the tumors, the best $\Delta\varphi$ should be case dependent. Thus, being different from the previous work where the $\Delta\varphi$ has only a single choice of 45° [67], we assume that the shield of RSBT is detachable, and there are multiple different shields available, each of them has a fixed zenith emission angle and a fixed azimuthal emission angle. While the zenith emission angles are always assumed to the same through this work, we do not put a limit on the selection of the azimuthal emission angle of S-RSBT to fully exploit its power. With this assumption, the user of S-RSBT has the flexibility to choose a proper shield with the best $\Delta\varphi$ for each specified clinical case.

1.2.2 Dynamic rotating-shield brachytherapy

Compared to S-RSBT, D-RSBT introduces a second shield layer for the already partially shielded source. While the second layer essentially complex the design

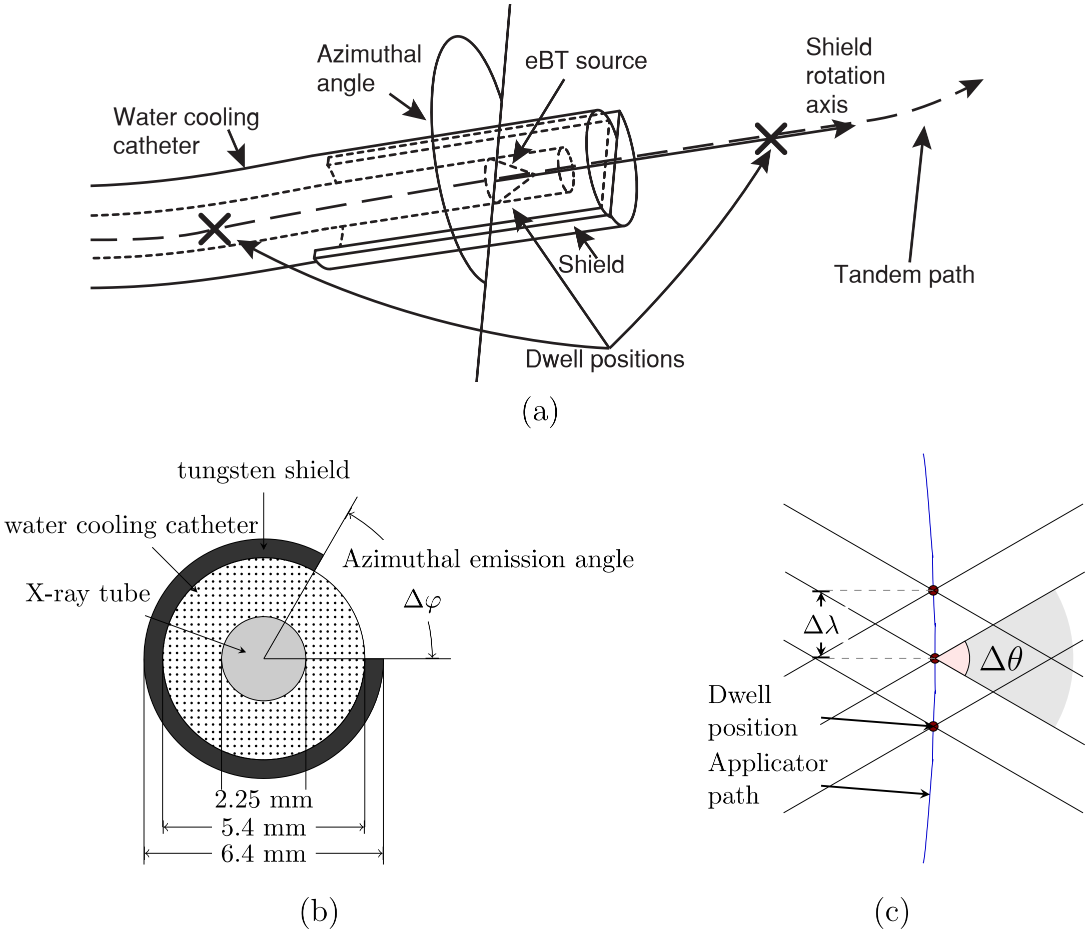

Figure 1.2: A conceptual model of an S-RSBT applicator with partially shielded eBT source. (a) Projection view. (b) Cross view (drawn to scale). (c) Longitudinal section view with the beamlet arrangement.

of RSBT applicator, it makes the azimuthal emission angle variable during the delivery. The current design is capable to make any azimuthal emission angle between 0° and 180° by the rotating the inner and outer shields independently(Figure 1.3). The ability to access small beams makes D-RSBT capable to deliver more conformal dose distribution compared to S-RSBT, yet at the price of longer delivery time. The limitation on the maximal azimuthal angle restricts the ability of D-RSBT with limited amount of delivery time.

1.2.3 Paddle rotating-shield brachytherapy

Instead of using shields with openings like S-RSBT and D-RSBT, P-RSBT uses a totally different way to form its rotatable shields. The shield of P-RSBT is formed by a set of radiation attenuating paddles. The paddles are assembled like a barrel. Each paddle can be operated (insert and retract) independently from others, forming exponentially different number of beams (Figure 1.4). Therefore, P-RSBT has a much larger degree of freedom compared to S-RSBT and D-RSBT; and theoretically it can form any beams that can be formed by S-RSBT and D-RSBT if the paddle is small enough. Moreover, it can form spatially discontinuous beams that cannot formed by S-RSBT and D-RSBT, giving it more flexibility on intensity modulation. Yet, the design of the P-RSBT may be considered to be the most complex one among the three, as the number of movable parts in P-RSBT is the largest.

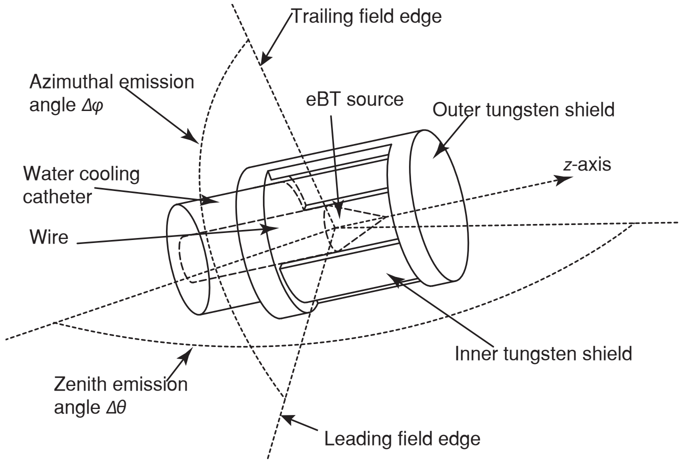

(a)

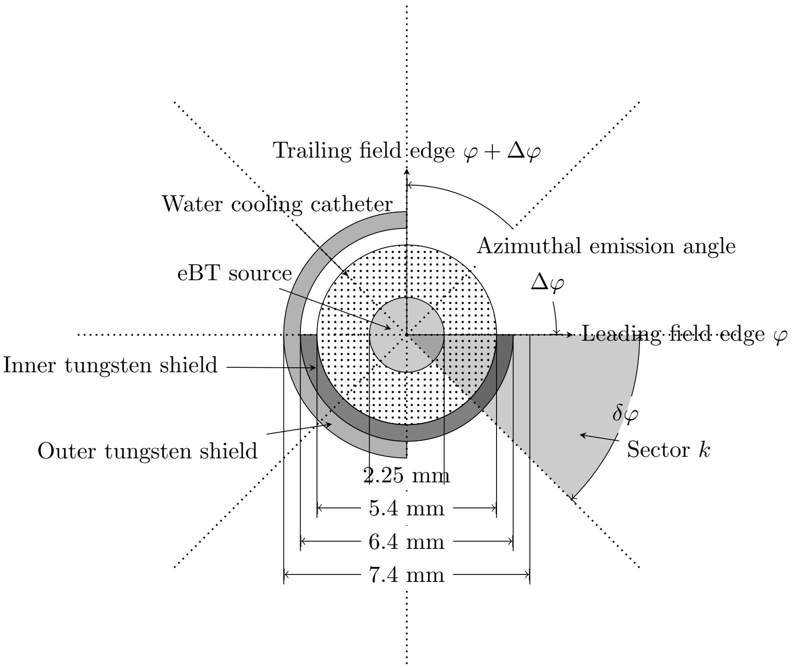

(b)

Figure 1.3: A conceptual design of a partially shielded eBT source for D-RSBT (a) 3D view, (b) cross section view.

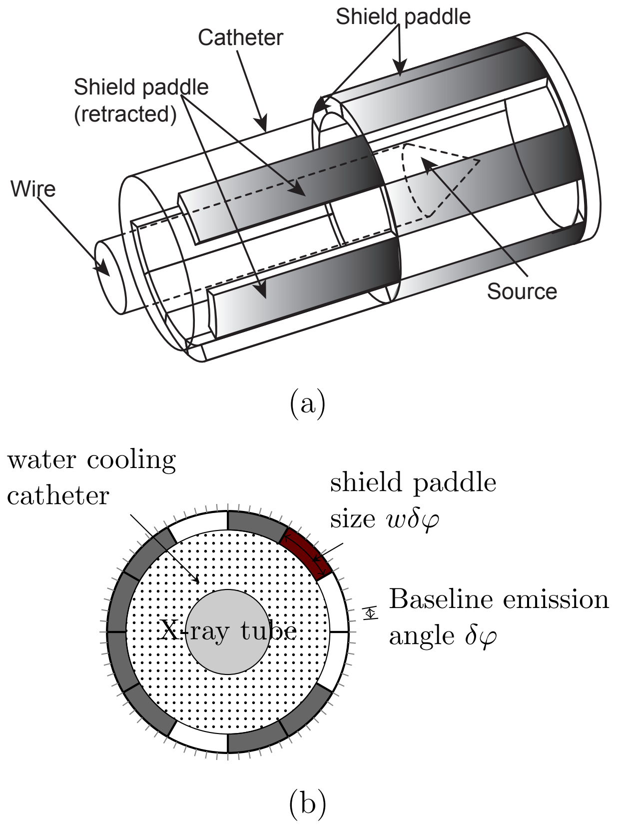

Figure 1.4: A conceptual design of a P-RSBT applicator (a) 3D view. For the purpose of legibility, not all paddle shafts are drawn. (b) Cross section view.

1.2.4 Unified treatment planning system for RSBT

For a given radiation source, it can be expected that the RSBT treatment planning and delivery is more time-consuming than conventional single-catheter brachytherapy delivery for multiple reasons. First, the radiation-attenuating shield blocks photons generated from the radiation source, increasing the amount of energy the source must emit during a treatment. [15] Since each eBT source has a finite lifetime, efficient usage of each source is necessary in order for the therapy to be cost-effective. Second, the treatment planning process for RSBT is more time-consuming than that for conventional brachytherapy. This is because the number of optimization variables for RSBT are greater than that of conventional brachytherapy due to the rotation capability and other possible degrees of freedom. For example, Shi *et al.* (2010) [51] reported multi-directional breast brachytherapy treatment planning and delivery times of 120 minutes and 37 minutes, respectively, while conventional brachytherapy treatment planning and delivery times were both about 5 minutes. Since patients tend to be under general or spinal anesthesia during brachytherapy treatment planning and delivery, prolonging these processes is expensive and inefficient. Therefore, to make the RSBT delivery clinically accessible, an efficient treatment planning procedure is required to reduce the delivery time of RSBT to an acceptable level with limited loss of quality.

Instead of making a completely different treatment planning system for each of the three RSBT method studied in this thesis, we proposed a unified method. The basic idea of this unified treatment planning system is based on the idea of abstract RSBT delivery model and anchor plans. In the abstract RSBT delivery model, the RSBT applicator is assumed to an S-RSBT applicator with a sufficiently small azimuthal emission angle called micro-azimuth-angle, denoted as $\delta\varphi$. The beams with azimuthal emission angle $\delta\varphi$ are called beamlets. By further assuming that all the azimuthal emission angle in S-RSBT and D-RSBT are integer multiples of $\delta\varphi$, any beams used in S-RSBT and D-RSBT can be considered as a superposition of a set of neighboring beamlets. By assuming each paddle in P-RSBT can cover a sector with angle that is a integer multiple of $\delta\varphi$, any beams can be formed by P-RSBT can be considered as a superposition of a set of beamlets as well.

This observation, which is called *beamlet superposition*, enables us separate the conventional *dose optimization* into *anchor plan optimization* and *optimal sequencing*. Therefore, a unified treatment planning system workflow is proposed for these three method as shown in Figure 1.5. The treatment planning system consists the following components:

1. Clinical data. When planning and delivering a brachytherapy, determining the tumor site and organs-at-risk is the first step. In this step, the planning target volume (tumor contours) and the organs-at-risk nearby will be extracted from 3D image datasets such as CT and MRI scans. The targets are typically manually contoured by experts. However, there are also several studies on computer-assisted segmentation and contouring [3, 8, 58, 54, 3].
2. Dose calculation. In this step, the source path and dwell positions need to be determined. Depending on the clinical cases and the equipment to be used

for delivery, the clinician will determine the positions to put the sources during the delivery as well as the travel path for the source (surgery might be involved). The source path varies depending on the apparatus used, such as tandem ovoid, [61] tandem with ring and interstitial needles [13]. Then, for any specified radiation source with specified dwell position and direction, the dose-rate at each voxel within the volume-of-interest (VOI) will be calculated. Monte-Carlo simulation [50, 49] and measurements [48] are typical methods used to obtains these values.

3. Anchor plan optimization. This step is the first main topic that will be covered in this thesis that distinguish our study from the previous HDR-BT treatment planning. In the anchor plan optimization, we assume that beamlets are the only beams will be used for delivery. This assumption significantly reduces the complexity of RSBT treatment planning with one-step dose optimization. Denoting $K = 360°/\delta\varphi$, the degree of freedom of one-step dose optimization is $\mathcal{O}(K)$ times more than the anchor plan optimization with S-RSBT, $\mathcal{O}(K^2)$ times more with D-RSBT and $\mathcal{O}(w2^{K/w})$ times more with P-RSBT, where $w\delta\varphi$ is size of the paddle.

   Anchor plan optimization is one of the most important step in the proposed treatment planning system. The output of the anchor plan optimizer, anchor plans (or equivalently, fluence maps) will be used as guidelines for the following optimal sequencing algorithms. Simply speaking, the quality of the anchor plan optimizer has a significant impact on the whole treatment planning system: if the anchor plan optimizer fails to generate anchor plans with acceptable quality, the quality of the final treatment plans cannot be expected to be satisfactory. According to preliminary studies, there are two major factors that affect the quality of the anchor plans: the dose distribution quality of the anchor plan itself and the "smoothness" of the fluence maps. Thus, an anchor optimization method that balances between the dose distribution quality and the smoothness of the fluence maps is desired.

4. Optimal sequencing. Anchor plans are generally of high dose quality, however, they cannot be used directly as delivery plan due to their prohibitory high delivery time. Thus, to make deliverable plans out of anchor plans, we propose optimal sequencing algorithms for each RSBT method studied in this thesis. The key idea of optimal sequencing is reducing the delivery time of the anchor plan by beamlet superposition. For example, if two beamlets with a same dwell time τ can be superposed by some RSBT delivery technique, the whole delivery time can be reduced by τ. However, if two beamlets with different dwell time is superposed, an error will be introduced while reducing the delivery time. Thus, the trade-off between delivery time and the dose quality should be considered by the optimal sequencing algorithm. Unlike the anchor plan optimization, where a universal abstract RSBT delivery model is used, the optimal sequencing algorithm depends on the concrete RSBT delivery model, as each different RSBT delivery method has a different way of superposing beamlets.

5. Plan evaluation. We evaluated the treatment plans by their delivery time and dose distribution quality. Specifically, the minimum dose received by the hottest 90% of the HR-CTV (D_{90}) under the constraint that the minimum doses to the hottest 2 cm^3 (D_{2cc}) of the rectum, sigmoid colon, and bladder could not exceed the tolerance doses [57, 47] of 75, 75, and 90 Gy, respectively.

1.3 Overview of the materials

1.3.1 The radiation source and dose calculation

We consider high-dose-rate electronic brachytherapy (eBT) sources as the HDR-BT sources for this thesis. For example, the 40-50 kVp eBT delivery system (Xoft Axxent^{TM}, Xoft Inc., Sunnyvale, CA).

In the previous RSBT studies by Ebert, [15, 16], the RSBT dose distributions was modelled from a partially-shielded radiation source with the dosimetric characteristics of ^{192}Ir, but shielded with an unknown material that provided a sufficiently low transmission rate for RSBT to be effective. Although the ideal transmission for an RSBT shield is dependent on the clinical case and the emission angle, a shield transmission of 50% was shown to be unacceptable. [15] An ^{192}Ir-based RSBT system for rectal cancer is currently under development, [67] and the minimum tungsten alloy shield thickness reported for the system is 10 mm, which, combined with the applicator required for delivery, may make using the system for RSBT at certain sites, such as cervical and prostate, challenging.

The advent of high-dose-rate eBT sources allows for small-diameter intracav-

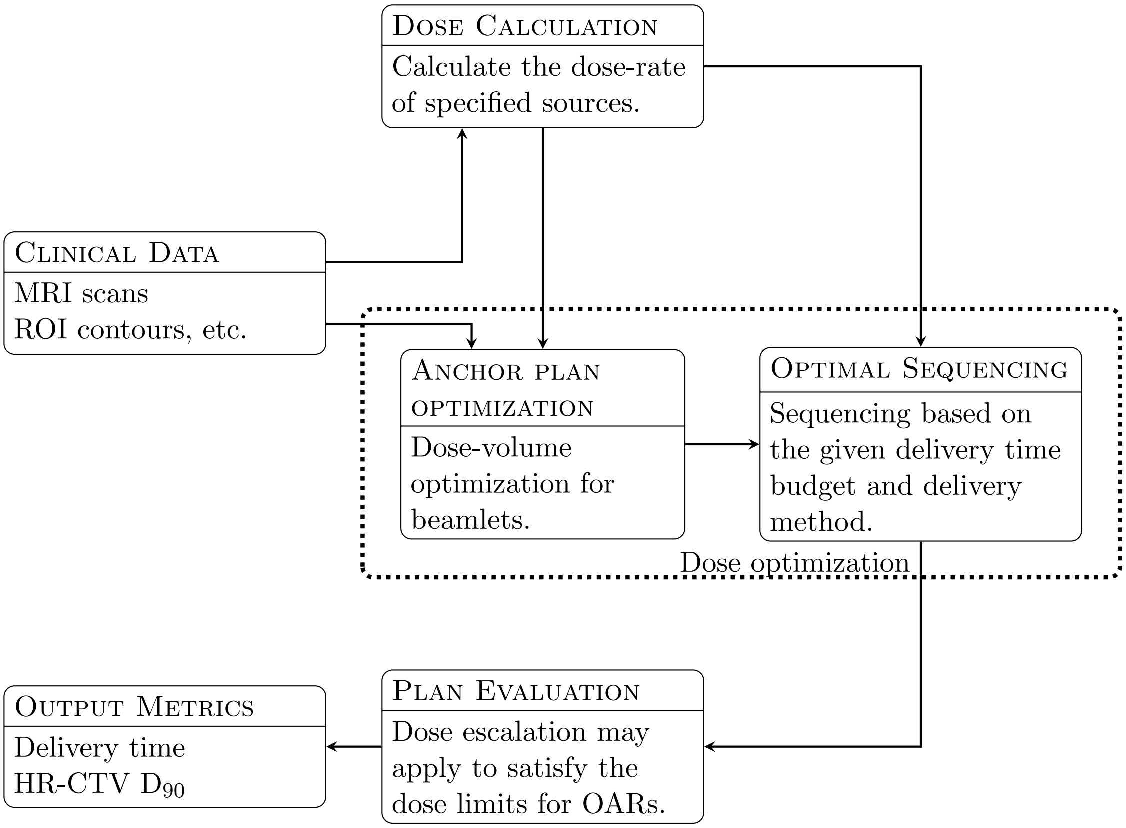

Figure 1.5: Unified treatment planning system. The dose calculator generates a set of beamlets $\dot{D}_i(j,k)$ based on the source path and the user-specified parameters: the source step length $\Delta\lambda$, the micro-azimuth-angle $\delta\varphi$, and the zenith emission angle $\Delta\theta$. Then the dose optimizer will generate an anchor plan which assigns a dwell time $\tau_{j,k}$ for each beamlet. The fluence map $\tau_{j,k}$ is an input for the optimal sequencer, and the optimal sequencer calculates the best way to approximately deliver the dose map specified by the anchor plan under the delivery time budget T_{max} with given delivery method.

itary RSBT applicators to be used for cervical cancer. The eBT device is a 2.25 mm diameter X-ray tube, contained in a 5.4 mm diameter water cooling catheter. [48] The transmission rate can be finely controlled, making delivery of less than 0.1% transmission possible when using a 0.5 mm tungsten shield. The eBT device with the rotating shield and applicator combination provide an RSBT system with an overall diameter of less than 7 mm (half the cross sectional area of a 10 mm diameter shield with a single layer of shield) as shown in Figure 1.2. Although there is no commercially available applicators with rotatable partial shields to the best knowledge of the author, there is a conceptual patented design. [53]

The TG-43 dose calculation model of Rivard et al (2006) [48] is used to calculate the beams. The dose rates at the points blocked by the shields are set to zero.

The RSBT delivery will be simulated by assuming a single-channel tandem applicator without ring or ovoids. It is also assumed that prior EBRT doses of 45 Gy in 25 fractions (fx) of 1.8 Gy each were delivered to the HR-CTV and OARs for all patients. The brachytherapy delivery was assumed to be applied over 5 fractions. The HR-CTV doses [Gy10] and OARs doses [Gy3] will be expressed as equivalent doses in 2 Gy per fraction of EBRT (EQD2), [13] using α/β values of 10 Gy and 3 Gy, respectively. [47] In the following sections, the HR-CTV and OARs doses will be measured with EQD2 and the subscripts will be omitted for brevity. The equation for calculating EQD2 is shown as Equation (1.1). [20]

$$\text{EQD2} = Nd\frac{1 + g\frac{d}{\alpha/\beta}}{1 + \frac{2}{\alpha/\beta}} \tag{1.1}$$

where parameter N indicates the number of fractions and the parameter d refers to the dose per fraction. As additional metric of delivery time will be considered, the parameter g, which is used to reflect the repair during the prolonged delivery process, is set to 1 for all cases.

1.3.2 Validations using clinical HDR-BT plans of cervical cancer

Cervical cancer cases will be the test cases in the experiment part of this thesis.

Of the nearly $12,000$ new cases of cervical cancer diagnosed annually in the U.S., about 57% ($6,800$) [45] are stage IB2 or higher. They are typically treated with a combination of cisplatin chemotherapy, external beam radiation therapy, and a brachytherapy boost to the tumor. [26] Cervical cancer brachytherapy has improved considerably in recent years through the use of magnetic resonance imaging (MRI)-guidance. [25, 47] Tumor regions that would be underdosed using intracavitary brachytherapy alone can be better visualized on MRI scans and treated with supplementary needle-based interstitial brachytherapy improving outcomes. [57, 12, 29, 36] In a 78-patient study of stage IB-IVA cervical cancer, patients with tumors of greater than 5 cm in size (40% of the patients), improved local tumor control and overall survival following additional needle-based interstitial brachytherapy. [46] Increased local tumor control at 3 years went from 64% to 82% ($p = 0.09$) and 3-year overall survival increased from 28% to 58% ($p = 0.003$) relative to conventional intracavitary methods. [15] As increasing the delivered tumor dose using supplementary interstitial brachytherapy has improved cervical cancer outcomes relative to intracavitary brachytherapy alone, it may be expected that RSBT based on eBT could be a less-invasive alternative to intracavitary plus interstitial brachytherapy, while still improving patient outcomes relative to intracavitary brachytherapy alone. RSBT for cervical cancer is considered in this thesis, although in principle RSBT may be delivered to breast, [36] prostate, [16] gynecological, and rectal [69] cancers.

Five cervical cancer cases with HR-CTV volume larger than 40 cm^3 were used in this work. The volumes of the HR-CTV were 41.28, 45.02, 76.65, 97.89 and 73.58 cm^3 respectively for case #1–#5. The HR-CTV and the organs-at-risk (OARs), namely the rectum, sigmoid colon, and bladder, were delineated on T2-weighted magnetic resonance image (MRI) by a radiation oncologist using the GEC-ESTRO recommendations. [25] The MRI resolution, which is also the voxel size, is 1mm × 1mm × 3mm. With RSBT delivery, theoretically, in the limit as the shield opening of beams approaches zero, treatment plan quality is maximized. The micro-azimuth-angle $\delta\varphi$ is thus set to 5°. The zenith emission angle is set to 180° for all cases and no modulation capability is assumed on the zenith direction.

The spacing parameter $\Delta\lambda$, is set to 5 mm which is consistent with the current clinical practice for HDR-BT in the radiation oncology department of University of Iowa.

1.4 Organization of the thesis

The rest of this thesis will be organized as follows. In chapter 2, an novel anchor plan optimization method named *Asymmetric Dose-volume Optimization with Total-variation Control* will be introduced, it will be also compared to two other existing methods including direct surface optimization and inverse-planning by simulated annealing. The optimal sequencing algorithm for S-RSBT named *Rapid Emission Angle Selection* will be described in chapter 3, to demonstrate its effectiveness and efficiency, exhaustive planning by surface optimization and volume optimization will be used for comparison. Chapter 4 studies the D-RSBT problem and two of its optimal sequencing algorithms, it also compares the quality of S-RSBT and D-RSBT under different circumstances. P-RSBT will be covered in chapter 5. Finally, in chapter 6, a brief conclusion and the discussion for future works will be made for this thesis.

CHAPTER 2
ASYMMETRIC DOSE-VOLUME OPTIMIZATION WITH TOTAL-VARIATION CONTROL

2.1 Introduction

Rapid RSBT delivery requires fast and efficient treatment planning and delivery software, in which efficient dose optimization is a key. The existing dose optimization algorithms for RSBT can be roughly classified into two categories: the dose-surface optimization (DSO) method [39, 73] and the inverse-planning simulated-annealing methods (IPSA). [15, 51, 39, 16] In conventional HDR-BT, the IPSA methods have been favored over other methods because of the potential improved clinical outcomes, [28, 35, 43] however, the computation time may be substantially increased. [51, 39] The increased computation time is mainly caused by the increased degree of freedom and the non-convex nature of the objective function used in the IPSA method. There are also several enhanced IPSA methods proposed to speed-up the computation. For example, instead of directly optimizing the dosimetric indices, the inverse planning by integer method solves relaxed linear programming problems iteratively by adding additional constraints. [52] Adaptive simulated annealing, which is also called very fast simulated re-annealing, was also previously applied in studies of external beam radiation therapy [59, 27] and brachytherapy planning [74]. Compared to other simulated annealing variants, adaptive simulated annealing exponentially decreases the cooling schedule to enable the fast convergence. Adaptive simulated annealing also performs periodic re-annealing to decrease the sensitivity to the initial conditions. These enhanced methods achieved comparable or better optimization results with lower computational time compared to IPSA in the conventional HDR-BT dose optimization. However, as these methods were designed for conventional HDR-BT, no directional intensity changes were considered during the optimization. The rotations magnify the degrees of freedom depending on the minimum size of rotation stride and may raise extra concerns such as the "smoothness" of the rotations. Thus, the absence of optimization for rotations may make these heuristics may not apply for RSBT. In short, finding an efficient dose optimization method tailored for RSBT while achieving comparable plan quality as the IPSA method is challenging and clinically important if the technique is to become practical.

The goal of this work is to develop a new dose optimization method named Asymmetric Dose-volume Optimization with Total-variation control (ADOT) for RSBT and to examine its performance by compared DSO and IPSA techniques.

2.2 Materials and methods

Previous studies on RSBT have shown that anchor plan generation is an important step in the whole RSBT inverse planning procedure as the anchor plan will serve as guidance for the subsequent optimal shield sequencing step and determines the quality of the final deliverable plan. [39] An anchor plan is defined as the treatment plan with a given azimuthal emission angle generated by some inverse optimization method. [39] The ADOT method developed in this work is tailored for the anchor plan optimization for RSBT. It takes into consideration both the dose distribution quality and the smoothness of dwell-time sequence of the anchor plan. As a vehicle to test ADOT, cervical cancer HDR-BT plans were used. As an optimization technique for RSBT, two different RSBT techniques are used; S-RSBT [39, 73] whose azimuthal emission angle is fixed during the delivery and D-RSBT [38, 37] whose azimuthal emission angle varies between $0°$ and $180°$.

2.2.1 Abstract RSBT delivery model

An abstract RSBT delivery model is essentially a S-RSBT delivery model (Figure 1.2) with efficiently small azimuthal emission angle $\Delta\varphi = \delta\varphi$, where $\delta\varphi$ is called micro-azimuth-angle.

In the RSBT delivery, the radiation source is placed in sequence along the tandem path longitudinally with distance between dwell positions of $\Delta\lambda$. The shield holding the radiation source has only one emission opening with fixed azimuthal and zenith emission angles, $\delta\varphi$ and $\Delta\theta$, respectively. At each dwell position, the shield is rotated about the center of the applicator axis. Each rotating increment is the azimuth angle $\delta\varphi$, that is, all the opening aperture (or equivalently, beam) at a same dwell position forms a partition of the cross section. After a full rotation at one dwell position, the source moves with the shield to the next dwell position along the path and repeat the delivery process. By partially shielding the radiation source and creating sectorial high-dose-regions, the shield is capable of azimuthally modulating the dose intensity. In the longitudinal direction, the zenith emission angle $\Delta\theta$ is set to constant 180° and no modulation ability is assumed .

With a given azimuthal emission angle $\delta\varphi$, the delivery plane around the radiation source at a dwell position is divided into $K = 360°/\delta\varphi$ sectors each with an equal angular size, where K is an integer (Illustrated as Figure 2.1). To quantitatively describe the structure of high-dose-regions formed by a partially-shielded source, we introduce the notation of beamlet. A beamlet, denoted by $\dot{D}_i(j,k)$, is defined as the dose rate at point $\vec{r}_i$ with the shielded source positioned at the j-the dwell position $\vec{s}_j$ ($j = 0,\ldots,J-1$) with the shield aligned with the k-th sector. The shield is positioned with the both field edges aligned with angle $k\delta\varphi$ and $(k+1)\delta\varphi$, respectively. Thus, the high-dose-region perimetrically described with an azimuthal emission angle $\delta\varphi$ and a zenith emission angle $\Delta\theta$. The TG-43 dose calculation model of Rivard et al (2006) [48] is used to calculate the beamlets. The source is assumed to be a shielded 50 kVp Xoft Axxent$^{\mathrm{TM}}$ (Sunnyvale, CA) and dose rates at the points blocked by the shields are set to zero.

The total dose received at point $\vec{r}_i$ can be calculated as a time-weighted sum of all beamlets:

$$d_i = \sum_{j,k} \dot{D}_i(j,k)\tau_{j,k} \tag{2.1}$$

where $\tau_{j,k}$ is the dwell time of beamlet $\dot{D}_i(j,k)$. We adopt the term fluence map (a.k.a intensity-map) [71, 72] from intensity-modulated radiation-therapy for the matrices formed by $\tau_{j,k}$. However, instead of being defined on a plane, the RSBT fluence map is conceptually defined on a cylinder (as illustrated in Figure 2.2).

Thus, the task for anchor plan optimization is to find the fluence map such that

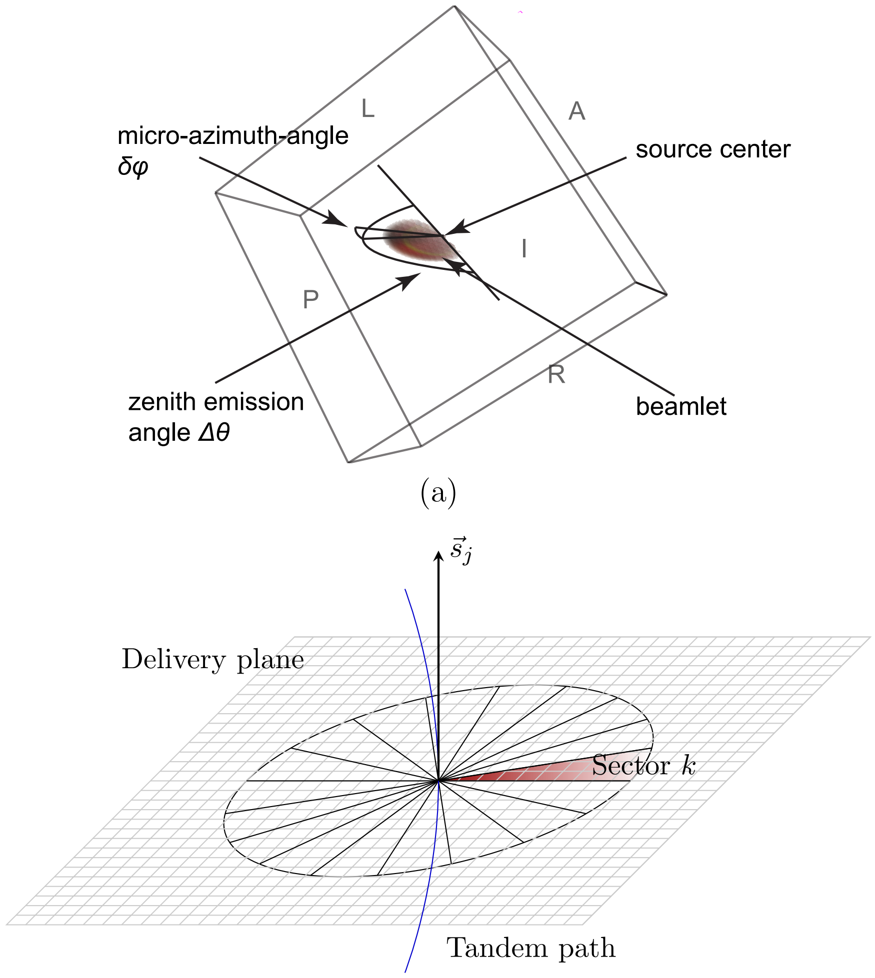

(a)

(b)

Figure 2.1: Illustration of a beamlet and the spatial arrangement of beamlets in 3D. (a) A 3D illustration of a beamlet. Letters A, P, L, R and I stands for anterior, posterior, left, right and inferior, respectively. (b) On the delivery plane which is orthogonal to the tangent of the radiation source path, the plane can be divided into $K = 360°/\delta\varphi$ sectors each with an equal angular size.

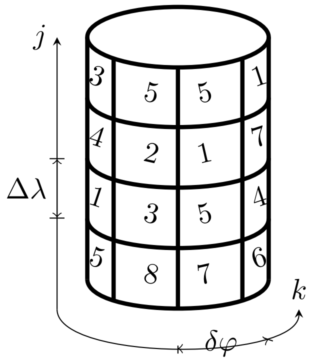

Figure 2.2: An example of an RSBT fluence map. Each number $\tau_{j,k}$ in the cell stands for the dwell time of the corresponding beamlet $\dot{D}_i(j,k)$. The j-axis denotes the radiation source path, and the k-axis stands for the sectors on the delivery plane which is orthogonal to the tangent of the radiation source path.

the dose distribution d_i is optimal with respect to a certain metric. The sequencing algorithm is then to convert a fluence map to a deliverable plan, which is not the focus of this chapter.

2.2.2 Asymmetric dose-volume optimization with total-variation control

In our ADOT method, we model the RSBT dose optimization as a total-variation minimization problem to compute an RSBT anchor plan. The objective function consists of two terms: one is the data fidelity term and the other is the smoothness term. The data term is the summation of the dose deviation penalties over all the voxels in volumes of interest (VOI), as shown in Equation (2.2).

$$F = \sum_{i \in \text{VOIs}} \left(\lambda_i^- H(s_i - d_i) + \lambda_i^+ H(d_i - s_i) \right) (d_i - s_i)^2 \tag{2.2}$$

where s_i is the prescribed dose, and λ_i^+, λ_i^- are coefficients for the overdosing and underdosing penalties, respectively, for each voxel i. $H(x) = \begin{cases} 1, & \text{if } x > 0 \\ 0, & \text{if } x \leq 0 \end{cases}$ is a Heaviside step function. By introducing the asymmetric factor $\lambda_i^- H(s_i - d_i) + \lambda_i^+ H(d_i - s_i)$ for the dose deviation penalty $(d_i - s_i)^2$, the ADOT model is able to differentiate overdosing from underdosing for different sites and locations. Intuitively, we can allow overdosing to HR-CTV but not underdosing by setting $\lambda_i^+ \ll \lambda_i^-$; and allow underdosing to OARs but not overdosing by setting $\lambda_i^+ \gg \lambda_i^-$.

The smoothness term is used to reducing the complexity of the dwell time sequence at each dwell position, which is important to improve the delivery efficiency and the quality of the delivered plan. Generating a deliverable plan from an anchor plans in RSBT delivery involves the combination of the neighboring beamlets, for example, combining $\dot{D}_i(j,k)$ with $\dot{D}_i(j,k+1)$ with dwell time $\tau_{j,k} = \tau_{j,k+1}$ results in a beam with azimuthal emission angle $2\delta\varphi$, and the whole delivery time can be reduced by $\tau_{j,k}$ due to this combination. However, in case that $\tau_{j,k} \neq \tau_{j,k+1}$, this combination will introduce an error while reducing the delivery time, and the smaller the difference between $\tau_{j,k}$ and $\tau_{j,k+1}$ is, the smaller the error will be. Thus, simplifying the sequence can be done by finding a dwell time sequence with the least variations in the neighboring dwell times, that is, to increase the sparsity of the sequence variations. This puts the RSBT dose optimization in the context of sparse signal reconstruction. Ideally, the L_0 minimization, which minimizes the number of non-zeros, serves as the best way for that sparse signal reconstruction. However, theoretically, minimizing the

L_0 "norm" is computationally intractable. Combining the L_0 norm with the D_{90} goal using the simulated-annealing method makes the computation even more challenging. Total-variation minimization can be a good alternative. We define the "smoothness" of the fluence map in the anchor plan as the sum of second-order total-variation at each dwell position,

$$\xi = \sum_{j\in[0,J-1]} \sum_{k\in[0,K-1]} \left(\tau_{j,k} - \tau_{j,(k-1)\%K}\right)^2 \tag{2.3}$$

where % stands for the modulus operation. Several studies on treatment planning for intensity-modulated radiation-therapy have shown that the total-variation form for the dose optimization successfully reduces the complexity of the fluence map by enhancing the sparsity of the fluence map variations, and desirably facilitating the dose delivery, while maintaining similar plan quality. [32, 31, 75, 76]

The objective function of our ADOT model takes the following form:

$$\min_{\tau_{j,k}} \ F + \beta\xi \tag{2.4}$$

$$\text{subject to } \tau_{j,k} \geq 0$$

where β determines the relative importance of the total-variation regulation term. Equation (2.4) can be considered as a quadratic convex programming problem and is solved by an in-house CPLEX-based optimizer. [10]

2.2.3 Experiment design

The performance of the ADOT method was evaluated from two different aspects: the quality of the anchor plans and the quality of the delivered plans using S-RSBT/D-RSBT.

For comparison, two other existing RSBT dose optimization methods were considered: DSO and IPSA. For the DSO, the method of linear least squares was applied to optimize the dose homogeneity on the HR-CTV surface. [39, 73, 17, 18, 19, 4] Specifically, the DSO method penalizes the total difference between the planned doses and the prescribed doses over all the voxels only on the HR-CTV surface. The IPSA directly optimizes the HR-CTV D_{90} subject to the constraints that none of the tolerance doses of the OAR D_{2cc} should be violated. Periodical re-annealing and greedy local search were applied alternatively to balance the convergence rate while maintaining the capability to escape from local optimums. A dummy OAR was added for IPSA calculation to avoid dose leakage through the volume of no interest. The dummy OAR includes all the voxels that do not belong to any OAR and locate within the range of 10-15 mm from the HR-CTV. The D_{2cc} limit of the dummy OAR was set to 90 Gy. To improve the efficiency of the IPSA method, the solutions output from the DSO method were used as the initial solutions. [39]

The anchor plans output by the dose optimizers are not deliverable directly due to the prohibitively long delivery times. To evaluate the deliverability of an anchor plan, we applied S-RSBT [39, 73] and D-RSBT [38, 37] shield sequencing methods to achieve a deliverable plan, and then evaluate the quality of the deliverable plan. The aim of both S-RSBT and D-RSBT is to achieve a deliverable plan with highest quality while subject to a given delivery time budget T_{max} by combining the neighboring beamlets in the anchor plans to from larger angular beams. Both methods may compromise the quality of the anchor plan. S-RSBT uses beams with a fixed azimuthal emission angle during the whole delivery process, while the emission angles of the beams used in D-RSBT can be varying. In both cases, the azimuthal emission angles are a multiple of micro-azimuth-angle $\delta\varphi$ used in the anchor plan. S-RSBT strives to find an azimuthal emission angle that achieves the best quality of the output deliverable plan. D-RSBT, in fact, finds the best combination of various azimuthal emission angles to deliver the anchor plan aiming to best approximate it. The maximum emission angle that can be used with D-RSBT in our experiment is 180°.

For each of the five clinical cases used in this thesis, we applied each of the ADOT, DSO and IPSA methods to compute an anchor plan. The quality of these anchor plans was compared based on the HR-CTV D_{90}, dose volume histograms (DVHs) and the dose distributions. We recorded the execution times for each method on each dataset for comparison. In addition, as a reference, the D_{2cc} of the OARs, and the total variations of the resulting plans were calculated.

We use delivery efficiency curves to compare the deliverability of the anchor plans produced by the three methods. A delivery efficiency curve is a Pareto curve where the x-axis refers the amount of the delivery times and the y-axis the HR-CTV D_{90} values, which indicates that for a given delivery time budget, what is the highest HR-CTV D_{90} of a deliverable plan using S-RSBT or D-RSBT for an anchor plan. This curve reflects the trade-off between the delivery time and dose distribution quality. A delivery efficiency curve is considered to be superior to another if it appears on the top-left to the other. For each patient case, six delivery efficiency curves were generated each for one of the three dose optimization methods (ADOT, DSO, and IPSA) and for either S-RSBT or D-RSBT.

There are two ways to interpret a delivery efficiency curve: (i) Given a D$_{90}$ goal (y-axis), the most appropriate delivery plan can be found at the leftmost point on the curve that is above the horizontal line ($y = D_{90}$ goal). According to the delivery efficiency curve, this point represents the minimal delivery time required to achieve the specified D$_{90}$. (ii) Given a delivery time budget (x-axis), the most appropriate delivery plan can be found at the top most point on the curve that is on the left of the vertical line ($x =$ time budget). This point represents the highest D$_{90}$ that can be achieved within the given time budget.

In our experiments, we appropriately set λ_i^- and λ_i^+ so that there was no penalty for overdose of the HR-CTV ($\lambda_i^+ = 0$) and no penalty for underdose of OARs ($\lambda_i^- = 0$). For each voxel in the HR-CTV with underdose and each voxel in OARs with overdose, we set the corresponding λ_i^- and λ_i^+ to the inverse squared distance between the voxel and the radiation source path. The prescribed dose of HDR-BT was set to 9 Gy through 5 fractions (equivalent with 115.5 Gy EQD2 in total with EBRT considered) for HR-CTV D$_{90}$. β was empirically selected as 100. To improve the computational efficiency of the dose optimizers, VOIs were considered for dose optimization in our experiments. More specifically, only those voxels located at a distance between 5 mm and 30 mm to the radiation source path or those within 10 mm away from the HR-CTV boundary surface were considered.

2.3 Results

As shown in Table 2.1, the average computational times for ADOT and DSO to generate an anchor plan are 75.8 and 3.7 seconds respectively, while we set 1800 seconds for IPSA to be terminated. The execution times on the five datasets with DSO and IPSA were quite consistent with a standard deviation of 0.2 and 0 seconds, respectively; while the computation times for ADOT range from 8.3 to 186.2 seconds.

Table 2.1: Dosimetric comparison for 5 clinical cases between the anchor plans generated with ADOT, DSO and IPSA optimizer.

Case	Method	HR-CTV D_{90} (Gy)	Bladder D_{2cc} (Gy)	Rectum D_{2cc} (Gy)	Sigmoid D_{2cc} (Gy)	Opt time (sec)	TV (h^2)
#1	ADOT	111	88	66	75	10	0.08
	DSO	97	79	62	75	4	0.04
	IPSA	107	90	60	75	1800	2.42
#2	ADOT	121	85	75	62	8	0.22
	DSO	107	90	75	52	4	0.15
	IPSA	123	90	75	60	1800	2.38
#3	ADOT	91	86	62	75	107	0.01
	DSO	82	73	56	75	4	0.09
	IPSA	92	90	66	75	1800	1.31
#4	ADOT	104	90	67	68	67	0.22
	DSO	85	77	64	75	4	0.59
	IPSA	100	90	75	75	1800	4.57
#5	ADOT	113	89	75	63	186	0.02
	DSO	100	86	75	59	4	0.17
	IPSA	116	90	75	75	1800	1.28
Avg	ADOT	108	87	69	69	76	0.11
	DSO	94	81	66	67	4	0.21
	IPSA	107	90	70	72	1800	2.39

Based on the anchor plan comparisons shown in Table 2.1, the ADOT method consistently achieves higher D_{90} compared to the DSO method. Compared to the IPSA method, the D_{90} achieved by ADOT method is higher in cases #1, #4 and #5, but lower for the others. The average D_{90} achieved by ADOT was 107.9 Gy, which was 13.7 Gy higher than that by DSO, and 0.5 Gy higher than that by IPSA. Visual comparison based on 2D dose distribution plots is shown in Figure 2.3 and the DVH plots are shown in Figure 2.4. The total-variations of the fluence maps for ADOT and DSO are comparable, with those of ADOT fluence maps being marginally lower than those of DSO plans on average. However, the total-variations in IPSA method are significantly higher (i.e., the corresponding fluence maps are much less smooth) compared to those in ADOT.

Both S-RSBT and D-RSBT convert a fluence map in the anchor plan to a clinically deliverable plan while scarifying the quality of the plan with a decreased HR-CTV D_{90}. The amount of D_{90} decrease is case dependent and depends on the amount of the allowed delivery time. In general, the amount of D_{90} decrease is associated with the total-variation of a fluence map. The higher the total-variation is, the less likely to achieve a deliverable plan with a high HR-CTV D_{90} as the allowed delivery time decreases.

The delivery efficiency curves for all five clinical cases with both S-RSBT and D-RSBT optimal sequencing are shown in Figure 2.5. Each subplot shows the delivery efficiency curves of one clinical case for the anchor plans output by ADOT, DSO and IPSA with one of the sequencing methods. It can be observed that, in most of the

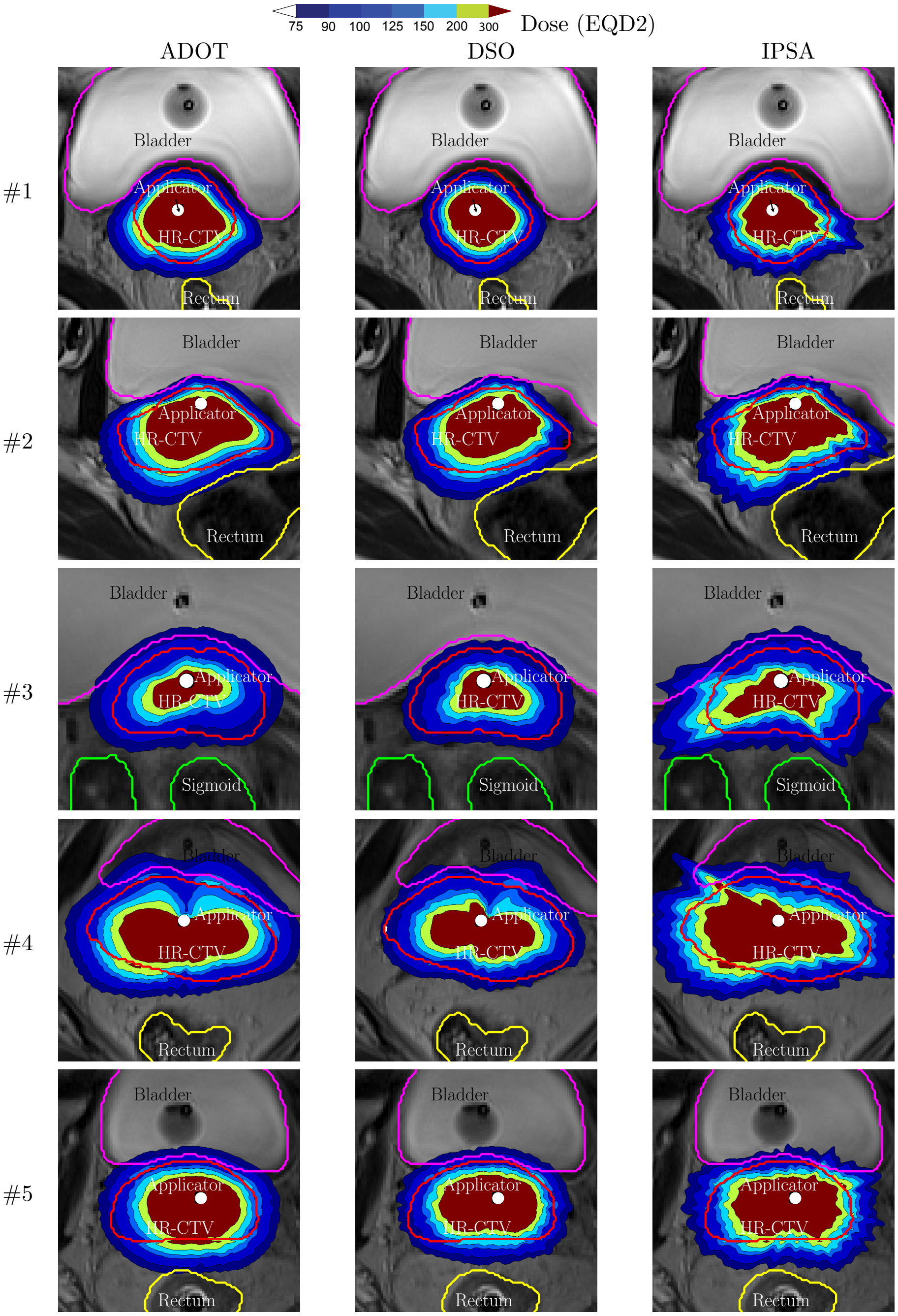

Figure 2.3: EQD2 dose distributions of anchor plans on a MRI slice for five patients with ADOT, DSO and IPSA dose optimization methods.

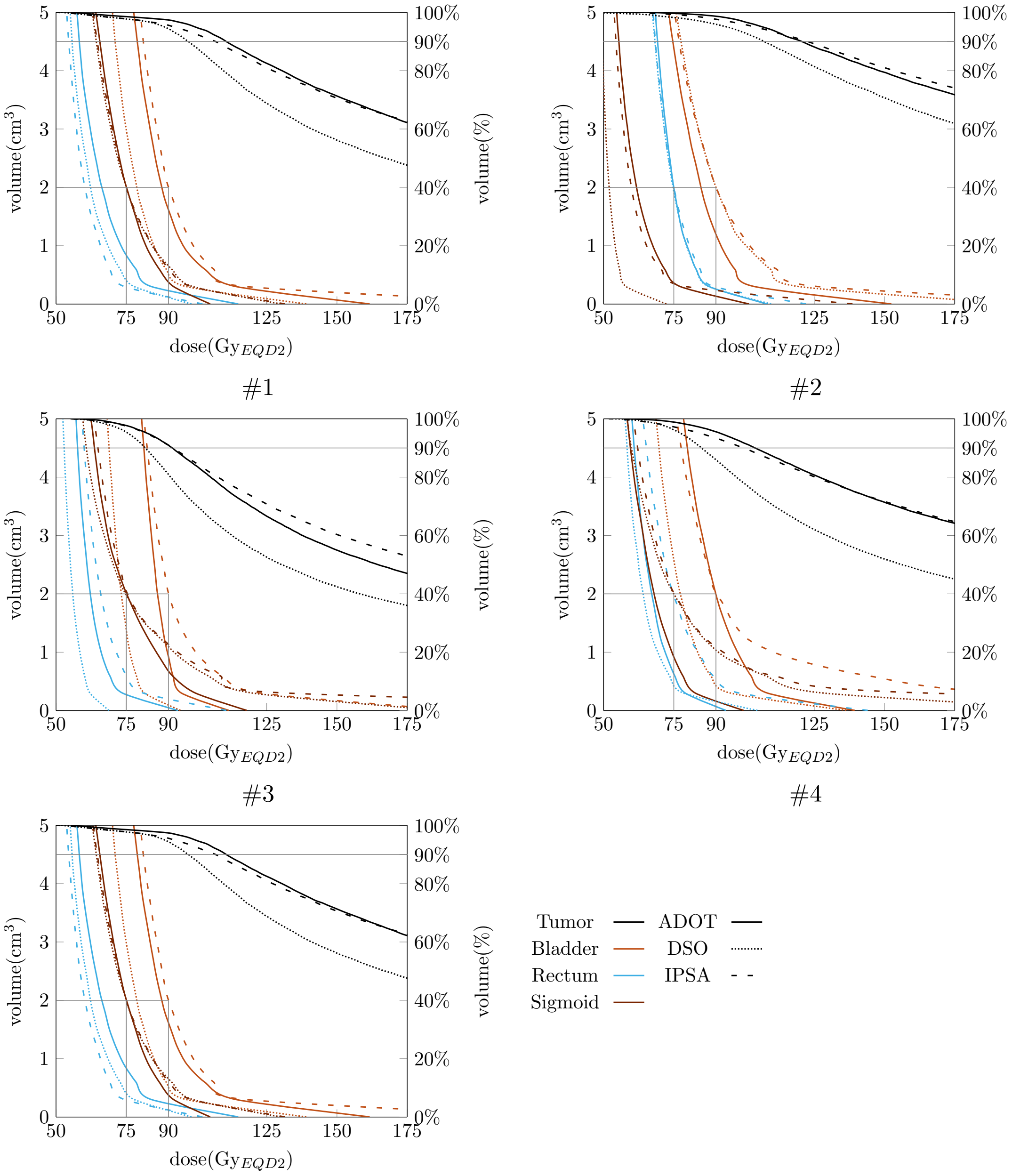

#1 #2 #3 #4 #5

Figure 2.4: DVH plots of anchor plans for five patients with ADOT, DSO and IPSA dose optimization methods.

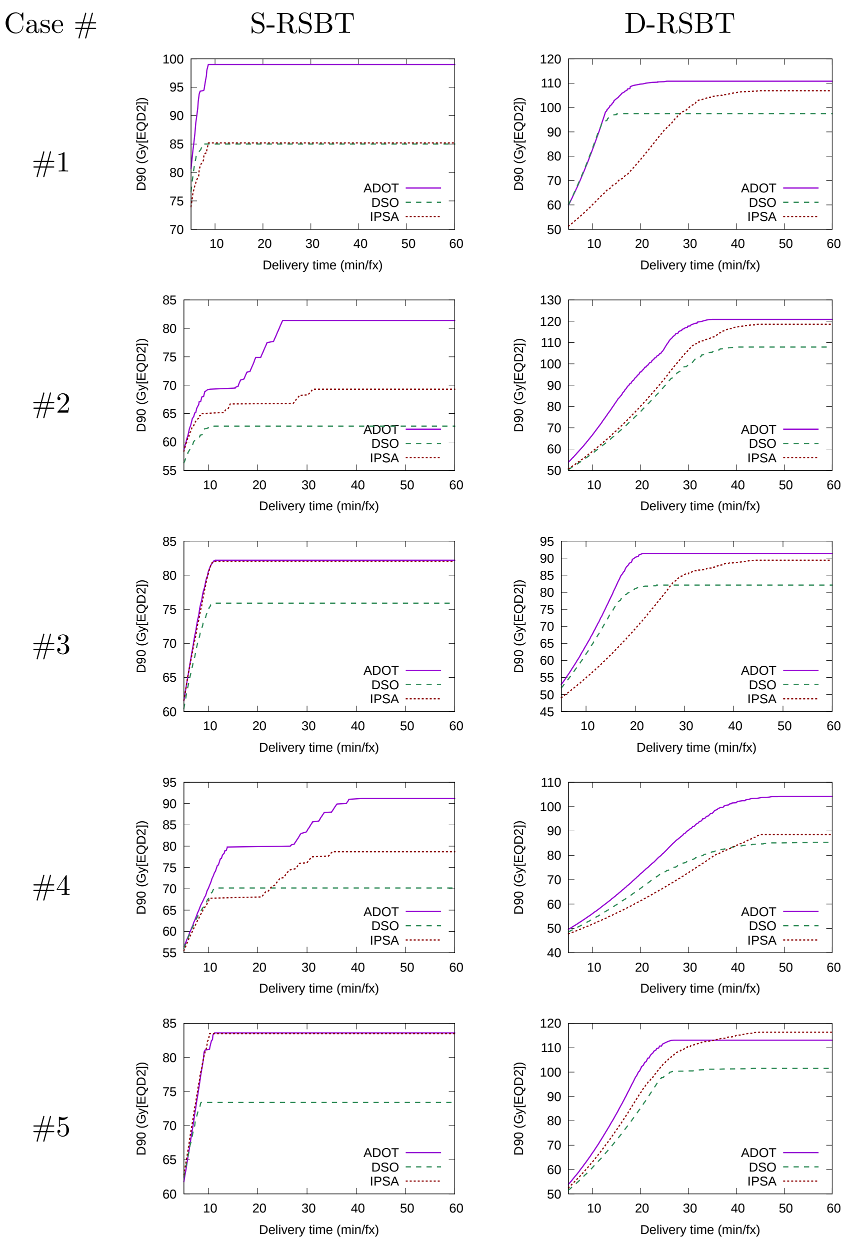

Figure 2.5: The comparison between delivery efficiency curves with S-RSBT and D-RSBT for anchor plans output by the ADOT, DSO and IPSA optimizers. The delivery time range was selected from 5–60 min/fx to show the trends of the delivery efficiency curves.

cases, the delivery efficiency curves of ADOT are better than the ones of DSO and IPSA. The curves of IPSA could be better than those of ADOT only with an extra-long delivery time. For example, in case #5, with delivery time larger than 40 min/fx, the D_{90} of IPSA is higher than the D_{90} of ADOT. For clinically acceptable delivery times, such as 10, 20 and 30 min/fx, the deliverable plans achieved by S-RSBT from anchor plans using ADOT are of 7.3, 10.4 and 12.5 Gy higher, on average, in HR-CTV D_{90}, respectively, than those by S-RSBT from anchor plans using DSO. For D-RSBT, the corresponding differences are 3.8, 12.4 and 13.1 Gy higher. Compared to the IPSA method, the anchor plans by ADOT are also of higher deliverability with respect to the HR-CTV D_{90} of the deliverable plans achieved by S-RSBT and D-RSBT. The corresponding differences are 4.0, 6.9 and 7.0 Gy higher in S-RSBT; 9.6, 17.8 and 9.7 Gy in D-RSBT.

2.4 Discussion

Note that the DSO model can be considered as a special case of the ADOT model, with only taking into account the voxels on the HR-CTV boundary surface. The experiments showed that the general ADOT model performed much better than DSO as expected, since there were more information incorporated. The IPSA method, as a stochastic heuristic method, was expected to achieve the highest HR-CTV D_{90} among the three methods. However, it showed a slightly lower D_{90} compared to ADOT. To explain this phenomenon, there are two possible reasons. First, simulated annealing algorithm can theoretically achieve the global optimum with sufficient running time. However, the running time of an IPSA algorithm is not upper bounded. With a given limit of 30 minutes, it is possible that the ADOT method performs better than IPSA. The second reason is the extra dummy OAR used to avoid dose leakage. Our experiments also showed that IPSA achieves 5.2 Gy higher D_{90} on average without the dummy OAR. But this change also significantly increases the average total-variation to 33.7 hour^2. The increased total-variation results in even lower D_{90} values after sequencing. With 20 min/fx delivery times, the average D_{90} will be 70.4 and 58.4 Gy for S-RSBT and D-RSBT, respectively. Thus, the dummy OAR should be considered as important component for IPSA as an implicit total-variation control mechanism. However, compared to the explicit total-variation control with a single parameter in ADOT, the dummy OAR involves a more complex setting of the parameters, including the voxels of the dummy OAR and its dose-volume tolerances.

Both the optimization time and the delivery time are important for RSBT planning due to its time-critical nature. In the previous study of S-RSBT planning, to ensure the dose quality with limited delivery time, three anchor plans were created with IPSA without using the dummy OAR. [39] The multiple anchor plans used can be considered as an alternative way for improving the smoothness of the fluence map by paying extra time in optimization. Based on the results shown in this chapter, substituting the previous IPSA method by ADOT for S-RSBT planning will reduce the optimization time cost and potentially reduce the delivery time while maintaining the D_{90} values. For the previous study on D-RSBT planning with IPSA, [38] we have the same observation. The ADOT method may also benefit other RSBT method such as dynamic modulated brachytherapy technique, [67] which has a similar mechanism as S-RSBT, given that the delivery plan can be induced from fluence maps.

Compared to IPSA method, ADOT takes much less optimization time with global optimum guaranteed with respect to its objective. However, the speed of ADOT method might be affected by the number of voxels and the number of beamlets used in computation. Defining VOIs is a good way to reduce the optimization time cost. However, if taking all the voxels in the HR-CTV and OARs into consideration, the average optimization time will increase to about 1500 seconds. The users yet need to be careful on defining proper VOIs. For example, if the VOIs of the 5 cases for this thesis were defined as only including voxels located at a distance of 5-30 mm to the radiation source path, the average HR-CTV D_{90} in the resulting anchor plans will be decreased by ∼8 Gy, and in case #2, the achieved HR-CTV D_{90} with ADOT will be 5 Gy less than that with the DSO method.

2.5 Conclusion

Compared with the DSO and IPSA methods, the ADOT method achieves a better balance between the optimization time and the dose quality of the anchor plans. More importantly, the anchor plan generated by the ADOT method is able to keep its total-variation at a low level with a marginal decrease of its HR-CTV D_{90}. This feature ensures that the anchor plans by the ADOT method can be converted to a deliverable plans with a high HR-CTV D_{90} using the S-RSBT or D-RSBT sequencing method.

CHAPTER 3
SINGLE ROTATING-SHIELD BRACHYTHERAPY WITH RAPID EMISSION ANGLE SELECTION

3.1 Introduction

Unlike the previous studies with S-RSBT, where a single [67] or a selected small set [73] of azimuthal emission angle(s) is available, in this thesis, it is assumed that S-RSBT users will have access to multiple shields with a range of azimuthal emission angles.

We extend the range of selection for the shields in S-RSBT because that the optimal azimuthal emission angle for S-RSBT is tumor-dependent, especially in the case of a target with an ellipsoidal cross section and a catheter that passes through the center of mass of the cross section. For a target with an ellipsoidal cross section with a width of three times the height, an azimuthal emission angle smaller than 180° will be necessary in order to treat the lateral tumor extensions without overdosing the normal tissue anterior and posterior to the tumor. For more cylindrical targets, as the width and height of the tumor approach each other, larger azimuthal emission angles become attractive, and the treatment times will decrease accordingly. In the case of a target with a cylindrical cross section, the ideal source is an unshielded one, and a conventional brachytherapy case is best.

The choice of an azimuthal emission angle is an important component in S-

RSBT planning. However, determining the ideal azimuthal emission angle for a given case is efficiently is not an intuitive task. Using exhaustive replanning with volume optimization (ERVO) is able to determine the ideal azimuthal emission angle, but the computational cost may not be acceptable and the treatment planning time would increase in proportion to the number of available shields; using exhaustive replanning with surface optimization (ERSO) as a heuristic can decrease the computational cost, but it may suffer the quality of the plan. In this work a Rapid Emission Angle Selection method (REAS) is presented that enables RSBT users to intuitively select an ideal balance between RSBT treatment time and dose distribution quality for a given clinical case.

3.2 Materials and methods

The key process in REAS is to separate the dose optimization stage into an anchor plan optimization stage and an optimal sequencing stage. In the anchor plan optimization stage as introduced in chapter 2, treatment plans are generated by assuming an abstract RSBT delivery model with a small azimuthal emission angle $\delta\varphi$. For any given azimuthal emission angle $\Delta\varphi = w\delta\varphi, w \in \mathbb{N}$, we use the optimal sequencing stage to reassemble the beamlets back into beams with the specified azimuthal emission angle. This decoupling process allows for the calculation of the dose optimization procedure independent of the azimuthal emission angle used for delivery. Optimal sequencing, the key part of REAS, requires less than two minutes of computational time for all 72 azimuthal emission angles used in this work except the one used for the anchor plan. A delivery efficiency curve is generated in about one minute, enabling the user to select the treatment plan that balances dose distribution quality and delivery time.

3.2.1 Radiation source model and dose calculation

The dose calculation model introduced in section 2.2.1 is adopted here with slight changes.

Define an S-RSBT beam, $\dot{D}_i(j,k,w)$, as the dose rate at the point $\vec{r}_i$ due to a shielded radiation source at dwell position $\vec{s}_j$ $(j = 0,\ldots,J-1)$. The shield has an azimuthal emission angle of $\Delta\varphi = w\delta\varphi$ and a zenith emission angle of $\Delta\theta$ (see Figure 1.2c). The irradiation direction of the beam is defined by φ_k, which is the lower of the two azimuthal angles defining the beam: $\varphi_k = (k\%K)\varphi(k = 0,\ldots,K-1)$, where $K = 2\pi/\delta\varphi$ is the number of different beams at a single dwell position. The % operation denotes modular arithmetic, enabling beamlet referencing with arbitrary integer k-values such that $\varphi_{k+K+1} = \varphi_{k+1}$. The upper azimuthal edge of beamlet k is located at angle $\varphi_k + \Delta\varphi$. The total dose delivered to point i from a shielded source with azimuthal and zenith emission angles of $\Delta\varphi$ and $\Delta\theta$, respectively, is calculated as a time-weighted sum of the appropriate beamlets over all dwell positions and emission angles:

$$d_i(w\delta\varphi,\Delta\theta) = \sum_{j=0}^{J-1}\sum_{k=0}^{K-1}\dot{D}_i(j,k,w)t_{j,k} \tag{3.1}$$

where $t_{j,k}$ is the dwell time, which is always greater than or equal to zero, for which the source is pointed in direction φ_k while it is located at dwell position $\vec{s}_j$.

In order to demonstrate the characteristics of the clinical cases used in this thesis, two conventional brachytherapy treatment plans for each case were also simulated: conventional intracavitary (ICBT) and interstitial plus intracavitary (IS+ICBT). A tandem applicator with ^{192}Ir was used for ICBT. for IS+ICBT, a Vienna tandem-and-ring style applicator [13] (Varian Medical Solution, Inc. Palo Alto, CA), with a ring radius of 21.25 mm and six holes for interstitial needles is used with a ^{192}Ir source were used. Interstitial needles will be used in all six holes except those one that will pass through the bladder.

3.2.2 Generating beams by combining beamlets

It was assumed that the micro-azimuth-angle, $\delta\varphi$, was small enough that all possible azimuthal emission angle $\Delta\varphi$ were integer multiples of it. It was also assumed that the shield window can only be aligned with directions which are integer multiples of $\delta\varphi$. As defined in section 3.2.1, beamlets are essentially beams with $\Delta\varphi = \delta\varphi$. The beamlets at a given dwell position $\vec{s}_j$ are assumed to be non-overlapping, thus the shadows cast by the shields of neighboring beamlets (k and $k+1$ for a given dwell position $\vec{s}_j$) do not overlap. An integer number, $w(w > 1)$, of neighboring baseline beamlets can be combined by superposition to produce a beamlet with a larger azimuthal emission angle as follows:

$$\dot{D}_i(j,k,w) = \sum_{p=0}^{w-1} \dot{D}_i(j,k+p) \tag{3.2}$$

generating a set of "w-beams". Equation (3.2) is exact for the case of zero shield transmission, which is a safe assumption for the case under consideration.

Consider the case in which the w neighboring beamlets, with indices from k to $k+w-1$, all share delivery times of $t_{j,k} = \tau$. It follows from Equation (3.2) that the w neighboring beamlets can be replaced with a single beamlet with an azimuthal emission angle $w\delta\varphi$ and a delivery time of $t^{w}_{j,k} = \tau$, where the t-superscript indicates that the delivery time is associated with a beam with an emission angle of $w\delta\varphi$. Conversely, a beam with an azimuthal emission angle of $w\delta\varphi$ and a delivery time of τ can be replaced with the beamlets with indices between k and $k+w-1$, which will have delivery times of $t^{1}_{j,k} = \tau$. Thus an entire set of dwell times associated with beam of azimuthal emission angle $w\delta\varphi$ can be also represented by the *fluence map*, which is the dwell times associated with beamlets:

$$t^{w\to 1}_{j,k} = \sum_{k'=0}^{K-1} t^{w}_{j,k'} \Pi\left(\frac{(k-k')\%K}{w}\right) \tag{3.3}$$

where $\Pi(a/w)$ is unity when $0 \leq a < w$ (a and w are both integers) and zero otherwise. The Π-function spreads the dwell times from the $w\delta\varphi$ beams over multiple beamlets. The modular arithmetic in its argument makes Π a periodic function of k' with period K. Equation (3.3) can be simplified by changing summation indices for k' to $p = k-k'$ as follows:

$$t^{w\to 1}_{j,k} = \sum_{p=0}^{K-1} t^{w}_{j,k-p} \Pi\left(\frac{p\%K}{w}\right) = \sum_{p=0}^{w-1} t^{w}_{j,k-p} \tag{3.4}$$

Since the sum over k' in Equation (3.3) is over one period $t^{w}_{j,k-p}$, which is a periodic function of k', the summation over p in the middle expression of Equation (3.4) can be done over the same range, even after changing variables.

3.2.3 Deliverable plan generation from anchor plans

As doing dose optimization is a computational-intensive work, it is challenging to generate plans with all possible w-values in times appropriate for clinical application. Our proposed method is to limit the number of calls to the dose optimizer, ideally, generating a single plan which is called the *anchor plan*. Then, an expedient treatment plan, which has a dwell time of $t^{w}_{j,k}$, is rapidly generated from an anchor plan by solving the following optimization problem:

$$\min \sum_{j=0}^{J-1}\sum_{k=0}^{K-1} \left(\lambda^{-}_{j,k} H(\tau_{j,k} - t^{w\to 1}_{j,k}) + \lambda^{+}_{j,k} H(t^{w\to 1}_{j,k} - \tau_{j,k})\right)(t^{w\to 1}_{j,k} - \tau_{j,k})^2$$

$$\text{subject to } t^{w\to 1}_{j,k} = \sum_{p=0}^{w-1} t^{w}_{j,(k-p)\%K}, \quad \forall j \in [0, J-1], k \in [0, K-1] \tag{3.5}$$

$$t^{w}_{j,k} \geq 0, \quad \forall j \in [0, J-1], k \in [0, K-1] \tag{3.6}$$

$$\sum_{j=0}^{J-1}\sum_{k=0}^{K-1} t^{w}_{j,k} \leq T_{max} \tag{3.7}$$

$$\tag{3.8}$$

where $H(x)$ is a Heaviside function and $\lambda^{+}_{j,k}, \lambda^{-}_{j,k}$ are coefficients for overdosing and underdosing at dwell position $\vec{s}_j$ and emission direction $k\delta\varphi$ of the beamlet respectively. In this work, $\lambda^{+}_{j,k}$ is proportional to the largest dose rate contribution (i.e. $\max_{i\in\text{OAR}} \dot{D}_i(j,k)$) to the OAR of the corresponding beamlet, and $\lambda^{-}_{j,k}$ is proportional to the largest dose rate contribution to the HR-CTV surface (i.e. $\max_{i\in\text{HR-CTV surface}} \dot{D}_i(j,k)$). $\tau_{j,k}$ is the fluence map comes from the provided anchor plan P. Theoretically, the correctness of the optimal sequencing algorithm introduced in this section is independent of the anchor plans, in the sense of its objective function. However, as described in chapter 2, to ensure the quality of the treatment plans generated by optimal sequencing algorithm, the anchor plan should keep a balance between the dosimetric quality and the smoothness of its fluence map. There are multiple ways to achieve this. In the first work that introduced the REAS method, [39] multiple anchor plans were used. The basic idea of multiple anchor plans is generating several different anchor plans from treatment plans with different azimuthal emission angles such as 90°, 180°, and 270°. Although no explicit smoothness parameter is used, this can be considered as an implicit smoothness control. In this work, the ADOT method is used. In contrast to the multiple anchor plans, ADOT method can reduce the time cost on generating anchor plans while maintain the quality loss at a reasonable level.

Due to the inevitable disagreement between $\tau_{j,k}$ and $t_{j,k}^{w \to 1}$ in most real-world cases, expedient treatment plan P^w may not reproduce the dose distribution of the anchor plan perfectly. The plan quality tends to degenerate as w increases. As a result, the expedient plan can be regarded as an approximation of the anchor plan. However, the approximation quality will decrease as w increases.

With the solution to Equation (3.8), $t_{j,k}^{w}$ is scaled to maximize D$_{90}$ in the HR-CTV without violating the OAR dose constraints. T_{max} is a constraint on the total delivery time of expedient plan which can be imposed to reduce treatment time at the expense of HR-CTV D$_{90}$. Obtaining expedient plans by solving the sequencing problem in Equation (3.8) is faster than the full optimization needed to obtain anchor plans (or other treatment plans), since the problem concerns dwell times only, rather than dwell times and beams.

3.2.4 Evaluation and comparison

To evaluate a planning method, the planning time and the plan quality were considered. The plan quality was established by maintaining a balance between the HR-CTV D_{90} and the corresponding delivery time under the constraint that all OAR D_{2cc} values are below tolerance. By plotting the best HR-CTV D_{90} can be achieved by the planning method against specified delivery time budgets, we generated a delivery efficiency curve for the planning method.

For the purpose of comparison, three different planning methods including REAS were applied to five clinical cases:

1. Exhaustive replanning with dose-volume optimizer (ERVO). With this method, the in-house dose-volume optimizer, using IPSA, was applied to all w-beamlets. To limit the time cost on doing ERVO, each single IPSA call is limited within 3 minutes.
2. Exhaustive replanning with surface optimizer (ERSO). Using DSO on all w-beamlets.
3. Rapid emission angle selection (REAS), based on anchor plans generated from ADOT.

For each clinical case and each planning method, a corresponding delivery efficiency curve was generated instead of a single plan. When using the ERVO method for example, the dose optimization with simulated annealing was applied to all 72 possible azimuthal emission angles. For each azimuthal emission angle, a delivery plan was generated with a delivery time (x-axis) and a HR-CTV D_{90} (y-axis). We called these plans (calculated directly with the dose optimizer or optimal sequencing) prime plans. The prime plans can be scaled with any scaling factor less than 1, resulting in a derived plan. A derived plan will have lower D_{90} and lower delivery time compared to the prime plan and the OAR dose will still be kept below the given threshold. By plotting derived plans with prime plans, we get continuous curves instead of discrete dots on the plots. The delivery efficiency curves for ERSO and REAS were generated by a similar method as described for ERVO.

3.3 Results

3.3.1 Planning time comparison

The ERVO method took about 5 hours to finish and was the most time-consuming method among the three methods studied in this work. The time costs for the ERSO and the REAS method are about 20 and 8 minutes, respectively. All three methods were applied to all 72 different azimuthal emission angles and were able to generate the corresponding delivery efficiency curve. When using the ERVO method, the time spent on dose optimization using the simulated annealing algorithm dominated the time cost, as each dose optimization took 3 minutes. It is important to note that the running time for the ERVO method depends on the pre-assigned computation time budgets as there is no guaranteed time for achieving an optimal solution with a simulated annealing based algorithm.

Because the ERSO method took less time; the whole procedure can be finished in around 20 minutes for all plans including the time needed to compute the beamlets.

The REAS optimal sequencing process required less than a second for each sequence. Therefore, the time cost of REAS method is dominated by the calculation of beamlets and the time cost on anchor plans. The whole process can be finished in about 8 minutes.

3.3.2 Plan quality comparison

We evaluated the conventional plans for both cases studied in this thesis, and the results are shown in Tables 3.1 and 3.2 . While IS+ICBT achieves higher D_{90} at the price of more invasive method, both method can only achieve D_{90} less than 87 Gy, which may result in suboptimal treatment outcomes. [11]

Table 3.1: List of conventional ICBT plans that were evaluated with HR-CTV D_{90}, OAR D_{2cc} and the delivery times.

Case	HR-CTV D_{90} (Gy)	Bladder D_{2cc} (Gy)	Rectum D_{2cc} (Gy)	Sigmoid D_{2cc} (Gy)	Delivery time (min/fx)
#1	73.1	90.0	56.7	64.0	4.7
#2	53.3	90.0	49.5	50.1	3.3
#3	67.5	90.0	55.3	69.9	6.0
#4	58.1	71.4	75.0	54.4	5.2
#5	61.9	90.0	57.8	53.1	4.5

For the three RSBT planning methods studied in this thesis, delivery efficiency curves were generated instead of single plans. The delivery efficiency curves for each patient with the three planning methods are shown in Figure 3.1.

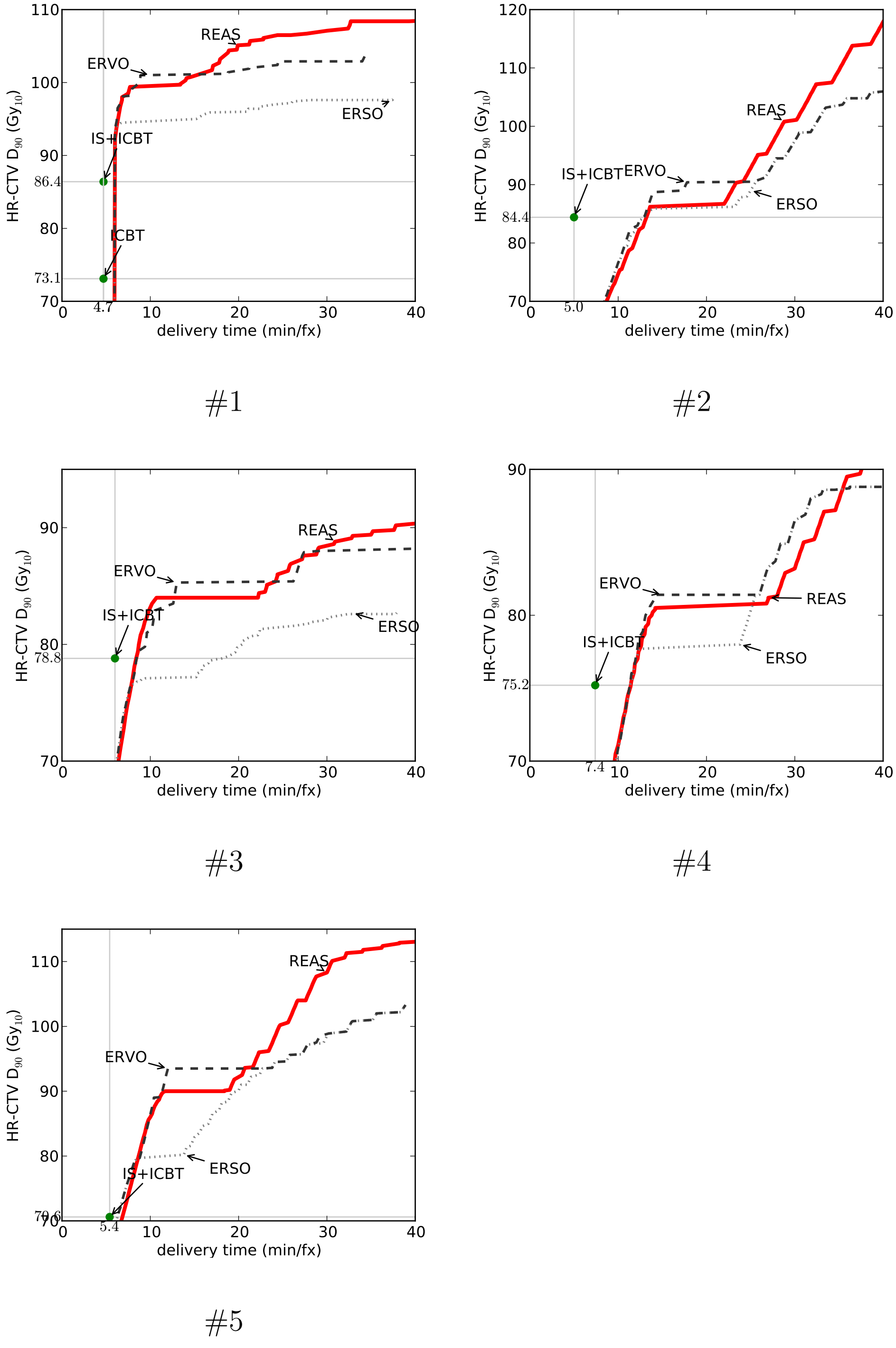

#1

#2

#3

#4

#5

Figure 3.1: Delivery efficiency curves for five clinical cases by using three different RSBT planning methods. ICBT/IS+ICBT plans are labeled for references.

Table 3.2: List of conventional IS+ICBT plans that were evaluated with HR-CTV D_{90}, OAR D_{2cc} and the delivery times.

Case	HR-CTV D_{90} (Gy)	Bladder D_{2cc} (Gy)	Rectum D_{2cc} (Gy)	Sigmoid D_{2cc} (Gy)	Delivery time (min/fx)
#1	86.4	90.0	56.1	70.2	4.7
#2	84.4	90.0	65.6	52.0	5.0
#3	78.8	82.8	57.4	75.0	6.0
#4	75.2	86.8	75.0	58.3	7.4
#5	70.6	90.0	58.6	56.4	5.4

As seen in Figure 3.1, the S-RSBT can achieve higher D_{90} than both ICBT (may not appear in the figure because of low D_{90}) and IS+ICBT at the price of longer delivery times. Both REAS and ERVO generate better delivery plans compared to ERSO method. It is also interesting to notice that although the ERVO method should do the best theoretically, REAS method has a better quality than ERVO in some cases. There are two possible reasons:

1. The running time of the IPSA is limited. While IPSA theoretically can achieve the global optimum with sufficient running time, the time cost might be unacceptable. And more importantly, the increased running time to each IPSA call will be magnified by the numbers of call to the dose optimizer. Thus, with limited time, the boost by IPSA algorithm from the initial solution might also be limited.
2. The dummy OAR (see section 2.2.3) limited the IPSA algorithm. This is the main difference between the IPSA algorithm used in this work and the one

used in the previous REAS study [39]. While the dummy OAR improves the smoothness of the fluence map, it may reduce the D_{90} as well.

The detailed quantitative comparisons between these methods with delivery time limited to 10–30 min/fx are shown in Tables 3.3–3.7. Take case #5 as an example, compared to ERSO method, ERVO can achieve 5 Gy higher D_{90} on average in the time interval 10–30 min/fx; and REAS method can achieve 6 Gy more. Excluding the contribution from EBRT, that is about 14% increase. On average of all 5 cases, the D_{90} achieved are 90.2, 86.0 and 90.4 Gy, respectively for ERVO, ERSO and REAS method. Thus, the increase on D_{90} from ERSO to REAS is about 4.4 Gy, which is about 10% more contribution from brachytherapy.

3.4 Discussion

By combining dose-volume optimization with the sequencing algorithm, the REAS method provides users a tool by way of the delivery efficiency curves to facilitate treatment planning in a reasonable time frame. Theoretically, the ERVO method can also provide users with the quality tools needed but at the cost of far greater computational times. The quality of the plans produced when using the REAS method are superior to those generated by ERSO according to the results of this chapter, and may be considered a closer approximation to the global optimum than the ERSO method.

The delivery efficiency curves seen in Figure 3.1 provide more information than simply describing the tradeoff between delivery time and dose quality. Based

Table 3.3: A part of the dosimetric comparison for case #1 between ERVO, ERSO and REAS methods with time budget set to 10–30 min/fx. The averages over delivery time were computed on all delivery time budgets in the range with 0.2 min/fx spacing.

Time budget (min/fx)		HR-CTV D_{90} (Gy)	Bladder D_{2cc} (Gy)	Sigmoid D_{2cc} (Gy)	Rectum D_{2cc} (Gy)	Delivery Time	$\Delta\varphi$
10	ERVO	101	89.9	66.8	75	8.9	215°
	ERSO	94.5	85.4	62.6	75	6.8	255°
	REAS	99.4	89.7	66.6	75	7.7	245°
15	ERVO	101	89.9	66.8	75	8.9	215°
	ERSO	94.5	85.4	62.6	75	6.8	255°
	REAS	100.8	88.9	67.5	75	14.7	130°
20	ERVO	101.4	89.9	63.6	75	18.8	105°
	ERSO	95.9	78	61.1	75	16.8	100°
	REAS	105.1	84.6	64.3	75	19.9	100°
25	ERVO	102.9	90	62.6	75	24.5	85°
	ERSO	97	79.2	60.4	75	24.1	70°
	REAS	106.5	84.6	63.3	75	24.4	85°
30	ERVO	102.9	90	62.6	75	24.5	85°
	ERSO	97.6	79	61.5	75	28.2	60°
	REAS	107.1	85.5	62.7	75	30	70°
Average achieved D_{90} ERVO: 101.7 Gy, ERSO: 96.0 Gy, REAS: 103.6 Gy							

Table 3.4: A part of the dosimetric comparison for case #2 between ERVO, ERSO and REAS methods with time budget set to 10–30 min/fx. The averages over delivery time were computed on all delivery time budgets in the range with 0.2 min/fx spacing.

Time budget (min/fx)		HR-CTV D_{90} (Gy)	Bladder D_{2cc} (Gy)	Sigmoid D_{2cc} (Gy)	Rectum D_{2cc} (Gy)	Delivery Time	$\Delta\varphi$
10	ERVO	76.6	89.5	62.5	53.4	10	190°
	ERSO	76.6	89.5	62.5	53.4	10	190°
	REAS	74.7	88.7	61.4	57.4	10	205°
15	ERVO	88.7	89.9	75	57.5	13.9	180°
	ERSO	85.9	89.1	75	53.5	14.3	165°
	REAS	86.2	90	73.6	64.7	13.6	190°
20	ERVO	90.4	90	75	66.8	17.8	170°
	ERSO	85.9	89.1	75	53.5	14.3	165°
	REAS	86.2	90	73.6	64.7	13.6	190°
25	ERVO	90.4	90	75	66.8	17.8	170°
	ERSO	89	80.9	73.7	51.4	25	100°
	REAS	92.8	74	73.4	53	25	105°
30	ERVO	97.5	86	74.1	52.6	30	90°
	ERSO	97.5	86	74.1	52.6	30	90°
	REAS	100.8	77.6	75	54.5	28.8	100°

Average achieved D_{90} ERVO: 89.2 Gy, ERSO: 87.1 Gy, REAS: 88.5 Gy

Table 3.5: A part of the dosimetric comparison for case #3 between ERVO, ERSO and REAS methods with time budget set to 10–30 min/fx. The averages over delivery time were computed on all delivery time budgets in the range with 0.2 min/fx spacing.

Time budget (min/fx)		HR-CTV D_{90} (Gy)	Bladder D_{2cc} (Gy)	Sigmoid D_{2cc} (Gy)	Rectum D_{2cc} (Gy)	Delivery Time	$\Delta\varphi$
10	ERVO	81	87.5	57.6	75	9.6	255°
	ERSO	77.1	74.8	55.7	75	9.5	230°
	REAS	83	90	60.7	73.8	9.9	265°
15	ERVO	85.3	89.4	66.1	75	13	215°
	ERSO	77.1	74.8	55.7	75	9.5	230°
	REAS	84	90	61.7	74.9	10.7	250°
20	ERVO	85.3	89.4	66.1	75	13	215°
	ERSO	79.7	78.7	58.6	75	19.8	115°
	REAS	84	90	61.7	74.9	10.7	250°
25	ERVO	85.3	89.4	66.1	75	13	215°
	ERSO	81.4	74.3	56.8	75	23.6	95°
	REAS	86	86.8	61.1	75	24.4	110°
25	ERVO	88	89.7	61.7	75	28.9	95°
	ERSO	82.1	73.8	56.4	74.8	30	75°
	REAS	88.3	86	61.2	75	29.1	95°
Average achieved D_{90} ERVO: 85.4 Gy, ERSO: 79.5 Gy, REAS: 85.0 Gy							

Table 3.6: A part of the dosimetric comparison for case #4 between ERVO, ERSO and REAS methods with time budget set to 10–30 min/fx. The averages over delivery time were computed on all delivery time budgets in the range with 0.2 min/fx spacing.

Time budget (min/fx)		HR-CTV D_{90} (Gy)	Bladder D_{2cc} (Gy)	Sigmoid D_{2cc} (Gy)	Rectum D_{2cc} (Gy)	Delivery Time	$\Delta\varphi$
10	ERVO	70.9	80.3	74.5	69.3	10	285°
	ERSO	70.9	80.3	74.5	69.3	10	285°
	REAS	71.1	88.8	63.6	57.8	10	285°
15	ERVO	81.4	90	74.7	74	14.2	240°
	ERSO	77.7	84.4	72.1	75	12.6	255°
	REAS	80.5	90	74	66.5	14.2	235°
20	ERVO	81.4	90	74.7	74	14.2	240°
	ERSO	77.7	84.4	72.1	75	12.6	255°
	REAS	80.5	90	74	66.5	14.2	235°
25	ERVO	81.4	90	74.7	74	14.2	240°
	ERSO	80.3	88.4	73.3	72	25	135°
	REAS	80.5	90	74	66.5	14.2	235°
25	ERVO	86.5	90	67.9	74.3	30	120°
	ERSO	86.5	90	67.9	74.3	30	120°
	REAS	83.2	87.6	66.2	60.6	30	120°
Average achieved D_{90} ERVO: 81.0 Gy, ERSO: 78.8 Gy, REAS: 79.9 Gy							

Table 3.7: A part of the dosimetric comparison for case #5 between ERVO, ERSO and REAS methods with time budget set to 10–30 min/fx. The averages over delivery time were computed on all delivery time budgets in the range with 0.2 min/fx spacing.

Time budget (min/fx)		HR-CTV D_{90} (Gy)	Bladder D_{2cc} (Gy)	Sigmoid D_{2cc} (Gy)	Rectum D_{2cc} (Gy)	Delivery Time	$\Delta\varphi$
10	ERVO	86.4	86.8	72.9	59.2	10	240°
	ERSO	79.7	90	64.5	55.2	8.8	230°
	REAS	86	84	74.7	60.6	10	265°
15	ERVO	93.5	90	75	74.2	12	230°
	ERSO	82.9	90	64	54	15	135°
	REAS	90	79.8	75	63.4	11.7	230°
20	ERVO	93.5	90	75	74.2	12	230°
	ERSO	90.1	89	63.2	55.3	20	110°
	REAS	91.8	84.4	75	60	19.5	135°
25	ERVO	94.5	90	63.5	56.2	24.1	95°
	ERSO	94.5	90	63.5	56.2	24.1	95°
	REAS	100.2	85.6	75	62	24.7	120°
25	ERVO	98.5	90	75	74.3	29.2	110°
	ERSO	98.5	89.5	67.5	57.5	30	80°
	REAS	108.3	88.1	74	64.8	30	105°
Average achieved D_{90} ERVO: 93.9 Gy, ERSO: 89.0 Gy, REAS: 95.0 Gy							

on our experimental results we found that: first, the delivery efficiency curves vary between cases, showing the selection of the azimuthal emission angle $\Delta\varphi$ should be case-dependent. moreover, it also depend on the time budgets and the treatment goals specified by the user. Second, smaller azimuthal emission angles do not guarantee better dose distributions. This conclusion seems to be counterintuitive, yet a simple explanation is that we are using a fixed azimuthal emission angle. If the larger azimuthal emission angle is not a multiple of the smaller one, we cannot always expect to get a better dose distribution by using the smaller angle. Supposing that Figure 3.2(a) shows the ideal dose distribution, then the dose distribution can be perfectly reproduced by set $\Delta\varphi = 3\delta\varphi$. However, with a smaller azimuthal emission angle $\Delta\varphi = 2\delta\varphi$, it is impossible to perfectly reproduce the dose distribution, as shown in Figure 3.2(b).

Although we only considered a single tandem applicator for all the RSBT planning within this work, the REAS method introduced here would also benefit from use in a multiple channel device such as those used in a tandem and ovoid applicator.

The RSBT system may be clinically implemented by using detachable partial shields. To fully exploit the potential of the REAS method, a set of different shields with all possible azimuthal emission angles is desired. In the cases studied in this work, this requirement leads to 70 different shields. While too many different shields may be economically inefficient for a clinical implementation, the number of shields may be reduced by using of a subset of all possible azimuthal emission angles instead

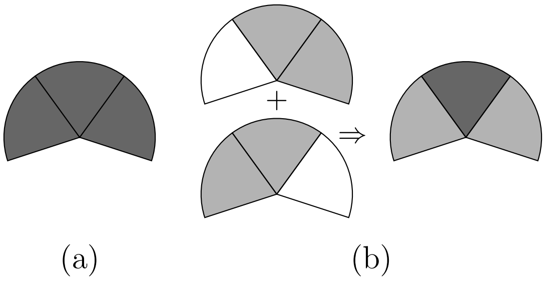

Figure 3.2: Situation in which a smaller azimuthal emission angle results in a worse dose distribution. (a) An dose distribution that can be perfectly reproduced with $\Delta\varphi = 3\delta\varphi$. (b) By using $\Delta\varphi = 2\delta\varphi$, it is impossible to perfectly reproduce the dose distribution shown in (a).

of the universal set. It was observed that more than 80% of the plans on the delivery efficiency that were clinically reasonable can be covered by azimuthal emission angles between 90° and 270°. Making use of this observation can reduce about half of the shields and make the required shields less than 30. The number of shields can be further reduced by increasing $\delta\varphi$. For example, with $\delta\varphi = 10°$, it is possible to reduce the number of shield to about 10.

3.5 Conclusions

Using the REAS technique introduced in this chapter, RSBT users will be able to strike a balance between the treatment time and the dose quality about 30 times faster than when using exhaustive dose-volume optimizations. It can even performs faster than exhaustive dose-surface optimizations. The REAS method can also boost the D_{90} by about 10% while maintaining the same delivery time compared to ERSO methods.

S-RSBT planning may benefit from the REAS technique and is more likely than conventional ICBT and IS+ICBT to yield better plans in the limited time available. Moreover, S-RSBT users will have the freedom to optimize the tradeoff between the delivery time and the HR-CTV dose conformity with S-RSBT by the selection of the azimuthal emission angle.

CHAPTER 4
DYNAMIC ROTATING-SHIELD BRACHYTHERAPY

4.1 Introduction

As the azimuthal emission angles in S-RSBT were assumed to be static during the delivery process, [15, 16, 51, 39, 73] it is possible that RSBT can be delivered using shields that are capable of varying the azimuthal emission angle during treatment delivery. We propose D-RSBT as a technique capable of using a variable azimuthal emission angle which is distinct from S-RSBT, which uses a constant azimuthal emission angle. The D-RSBT source is assumed to be an eBT source, shielded by two layers of rotatable tungsten alloy shields. On each of the shields, there is a 180° azimuthal shield angle opening. By rotating the shields, any azimuthal emission angle that is less than 180° can be formed during the treatment delivery (Figure 1.3). To enable D-RSBT to be used in clinical practice, a systematic approach that can fully exploit its capability is necessary.

While D-RSBT may theoretically be able to form any azimuthal emission angle less than 180° by rotating the shields (Figure 1.3), an assumption is made to simplify the study. The field edges, which are the boundaries of the non-shielded regions in the cross sectional view, are aligned with K discrete and evenly spaced azimuthal angles in the polar coordinate system centered at the eBT source. As a result, instead of having an infinite number of different shield arrangements at a single dwell position, the number of different arrangements is $K^2/2$ at a single dwell position.

In this work, we propose two different optimal sequencing methods, one uses the combinatorial approach and the other uses a numerical method.

4.2 Optimal sequencing with combinatorial optimization

Using combinatorial approach, we model the optimal sequencing problem as a geometric optimization problem called *Circular Integral Block Decomposition* (CIBD). For a specified dwell position $\vec{r}_j$, the corresponding row of fluence map $\tau_{j,k}$ is denoted as a nonnegative integral function t defined on an integral interval $\mathcal{C} = [0, n-1]$, where n is used instead of $K = 360°/\delta\varphi$ to comply with the convention of algorithm complexity analysis. Each entry of t is assumed to be a integer between 0 and H. While real number are allowed in fluence maps, it is still a safe assumption that all then entries of fluence maps are rational thus we can find a way to convert the fluence maps to be integral. With the leading field edge and trailing field edges aligned with direction $a\delta\varphi$ and $b\delta\varphi$, we can represent a beam with pair $[a, b],\ a, b \in \mathcal{C}, a \leq b$, where a *circular interval* $I_c(a, b)$ of $\mathcal{C}$ is defined as,

$$I_c(a,b) = \begin{cases} [a,b], & \text{if } a \leq b, \\ [a, n-1] \cup [0, b], & \text{otherwise.} \end{cases} \tag{4.1}$$

For an integer $h > 0$, a *block* $\langle a, b, h \rangle$, which is used to represent a beam with leading field edge and trailing field edges aligned with direction $a\delta\varphi$ and $b\delta\varphi$ and dwell time h, is defined as a *window function* $f(x)$ on the circular interval $I_c(a, b) \subseteq \mathcal{C}$, with

$$f(x) = \begin{cases} h, & x \in I_c(a,b) \\ 0, & \text{otherwise.} \end{cases} \tag{4.2}$$

h is called the *height* of the block $\langle a, b, h\rangle$, and its *width* is $(b - a + 1) \mod |\mathcal{C}|$. Note that if $b = |\mathcal{C}| - 1$ and $a = 0$, the width of the block is $|\mathcal{C}|$ instead of 0. Intuitively, the CIBD problem seeks to find a set $\mathbf{B}$ of blocks $\langle a_k, b_k, h_k\rangle$ that "approximates" the given function t by "tiling" them up, and in fact it is a simulation of the process of using beams to reproduce the dose distribution of the anchor plan.

The function $\mathcal{F}_{\mathcal{B}}(x)$ obtained by tiling up all the blocks in $\mathbf{B}$ is defined, as follows.

$$\mathcal{F}_{\mathbf{B}}(x) = \sum_{\langle a_k, b_k, h_k\rangle \in \mathbf{B}, x \in I_c(a_k, b_k)} h_k. \tag{4.3}$$

More precisely, given a nonnegative integral function t defined on an integral interval $\mathcal{C} = [0, n-1]$ and two integers $w > 0$ and $H > 0$, the CIBD problem seeks to compute a set $\mathbf{B}$ of blocks $\langle a_k, b_k, h_k\rangle$ such that (1) the width of each block is no larger than w; (2) the total height of the blocks in $\mathbf{B}$ is no larger than H, i.e., $\sum_{\langle a_k, b_k, h_k\rangle \in \mathbf{B}} h_k \leq H$; and (3) the approximation error $\mathcal{E}(\mathbf{B}) = \sum_{x=0}^{n-1} (\mathcal{F}_{\mathbf{B}}(x) - t(x))^2$ is minimized.

Figure 4.1 shows a CIBD problem instance. The function t is defined on an integral interval $[0, 3]$ specified on a circle in the counter-clock wise order, with $t(0) = 4, t(1) = 5, t(2) = 2$ and $t(3) = 4$. The function can be decomposed to a set of 4 blocks $\mathbf{B} = \{\langle 0, 1, 2\rangle, \langle 1, 3, 1\rangle, \langle 2, 3, 1\rangle, \langle 3, 1, 2\rangle\}$, while $w = 3$ and $H = 6$; and the approximation error $\mathcal{E}(\mathbf{B}) = 0$.

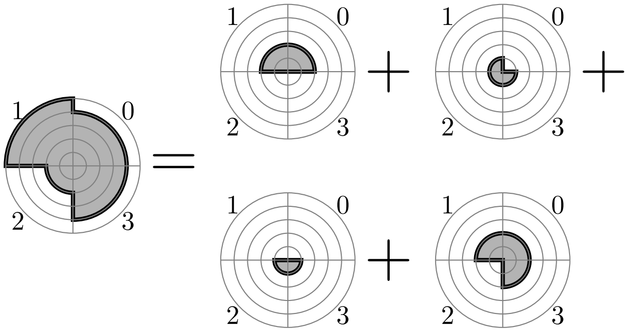

Figure 4.1: Illustration of a CIBD problem instance. On the left panel, a “pie-chart” is used depict a integral function t defined on an integral interval $[0, 3]$, and the function values are shown by the radius of the fans at the corresponding positions in the counter-clock wise order. This function t is equivalent to the sum of 4 blocks as shown by the 4 “pie-charts” on the right panel.

4.2.1 Canonical blocksets and admissible function pairs

It can be noticed that the solution of a CIBD problem can be represented by a set of blocks encoded by triplets. However, without additional information, this solution space is relatively unstructured. In this section, first we will show that any solution to a CIBD problem can be equivalently substituted by a canonical blockset. Simply speaking, both the first and the second component of the triplets in a canonical blockset can be sorted into non-decreasing order simultaneously. And this property can be extended with the circularity taken into consideration. Then we will show the equivalence between the canonical blocksets and the admissible function pairs. And finally, we will formulate the problem into a convex cost integer dual network flow problem by revealing the structure of this problem.

The key idea behind the canonical blocksets is the *equivalence*. By defining the equivalence in the CIBD solution space, the solution space is partitioned into equivalence classes. And for each equivalence class, we select a single solution that has a monotone structure to represent the whole class. We name this solution as canonical blockset. Therefore, instead of searching the whole solution space of CIBD, we can limit our search within the subspace that only contains canonical blocksets.

To start with, we have the following definitions for blocksets: feasible, equivalent and canonical.

Note that the CIBD problem is defined on a circular interval $\mathcal{C} = [0, n-1]$, and a window function (a block) is defined on a sub-interval $[a_k, b_k] \subset \mathcal{C}$ with $a_k, b_k \in [0, n-1]$. Without loss of generality, we unify the representation of a block, that is, a block is a feasible one if and only if $\langle a_k, b_k, h_k \rangle$ with $b_k > a_k \geq 0, (b_k - a_k) \leq w, a_k < n$ and $h_k > 0$. Thus, we will have $a_k \in [0, n-1]$ and $b_k \in [0, n+w-1]$.

Definition 4.1. *A blockset* $\mathbf{B}$ *is* feasible *if and only if every* $B_k \in \mathbf{B}$ *is feasible.*

Definition 4.2. *Two blockset* $\mathbf{B}$ *and* $\mathbf{B}'$ *are* equivalent *if and only if* $\mathcal{F}_{\mathbf{B}} = \mathcal{F}_{\mathbf{B}'}$ *and* $H_{\mathbf{B}} = H_{\mathbf{B}'}$*, where* $\mathcal{F}_{\mathbf{B}} = \mathcal{F}_{\mathbf{B}'}$ *stands for a function equivalence:* $\forall x \in [0, n-1], \mathcal{F}_{\mathbf{B}}(x) = \mathcal{F}_{\mathbf{B}'}(x)$*; and* $H_{\mathbf{B}} = \sum_k h_k$ *stands for the total height of blocks in a blockset* $\mathbf{B}$.

Definition 4.3. *A feasible blockset* $\mathbf{B} = \{\langle a_k, b_k, h_k \rangle | k \in [1, K]\}$ *is* canonical *if and only if* $\mathbf{B}$ *satisfies the following properties:*

CB1. $\forall k \in [1, K-1], a_k \leq a_{k+1}, b_k \leq b_{k+1}$;

CB2. $b_K - n \leq b_1$*;*

With the definition of equivalence between blocksets (i.e. the solutions to CIBD), now we are at the point to introduce the first key theorem: we can always find a canonical blockset to represent an abitrary feasible solution to CIBD without affecting the objective and the constraints.Therefore, the CIBD problem can be solved by considering canonical blocksets only.

Theorem 4.1. *For any feasible blockset* $\mathbf{B}$*, there exists a canonical blockset* $\bar{\mathbf{B}} = \{\langle \bar{a}_k, \bar{b}_k, \bar{h}_k \rangle | k \in [1, \bar{K}]\}$ *such that* $\bar{\mathbf{B}}$ *and* $\mathbf{B}$ *are equivalent.*

Proof. Theorem 4.1 can be proved with a constructive method, i.e. a canonical block set $\bar{\mathbf{B}}$ which is equivalent to $\mathbf{B}$ can be constructed by $\mathbf{B}$ with a few transformations. The key idea in these transformations is that: for any pair of blocks that makes either property CB1 or CB2 violated, we can find a set of blocks to replace the pair of blocks such that no violation occurs within the new set of blocks introduced; and the updated blockset remains equivalent with the original one.

First, $\bar{\mathbf{B}}$ is copied from $\mathbf{B}$ thus they are obviously equivalent. Secondly, the blocks in $\bar{\mathbf{B}}$ can be sorted in ascending order according to $\bar{a}_k$: $\forall k \in [1, \bar{K} - 1], \bar{a}_k \leq \bar{a}_{k+1}$. However, the sorting does not necessarily make $\bar{b}_k \leq \bar{b}_{k+1}$.

As shown in Figure 4.2, suppose $\bar{B}_i(\bar{a}_i, \bar{b}_i, \bar{h}_i), \bar{B}_j(\bar{a}_j, \bar{b}_j, \bar{h}_j) \in \bar{\mathbf{B}}$ with $i < j$ and $\bar{a}_j \geq \bar{a}_i, \bar{b}_j < \bar{b}_i$, and there are 3 cases:

1. $\bar{a}_j = \bar{a}_i, \bar{b}_j < \bar{b}_i$. In this simplest case, swap the order of these two blocks as Figure 4.2(a) shows. As no change is made to the blockset $\bar{\mathbf{B}}$ except a reordering,

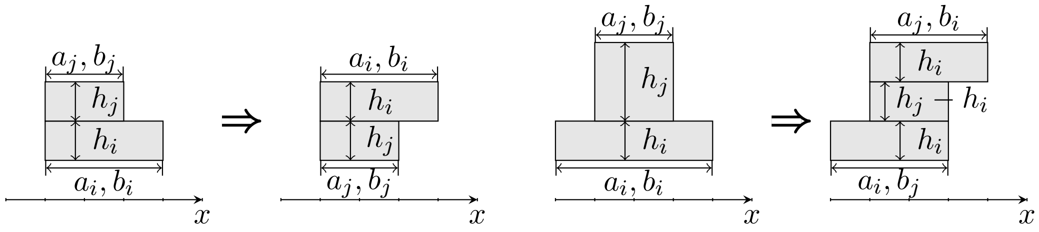

(a) $a_j = a_i, b_j < b_i$

(b) $a_j > a_i, b_j < b_i, h_j \geq h_i$

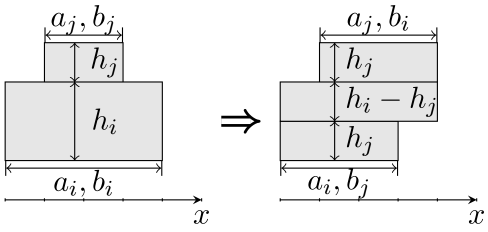

(c) $a_j > a_i, b_j < b_i, h_j < h_i$

Figure 4.2: Illustration of the canonical transformation, assuming that $j > i$. For each of the three cases that violate property CB1, the given block pairs can be substituted with a set of new blocks. The violation then will be fixed within the introduced new set of blocks, and the updated blockset is equivalent with the original one. Note that, property CB2 is essentially the same as CB1 with circularity considered.

the equivalence will not be affected.

2. $\bar{a}_j > \bar{a}_i, \bar{b}_j < \bar{b}_i, \bar{h}_j \geq \bar{h}_i$. In this case, 3 new blocks are used to substitute 2 blocks $\bar{B}_i, \bar{B}_j \in \bar{\mathbf{B}}$, namely $\bar{B}_{k_1} = \langle \bar{a}_i, \bar{b}_j, \bar{h}_i \rangle$, $\bar{B}_{k_2} = \langle \bar{a}_j, \bar{b}_j, \bar{h}_j - \bar{h}_i \rangle$ and $\bar{B}_{k_3} = \langle \bar{a}_j, \bar{b}_i, \bar{h}_i \rangle$ with $k_1 < k_2 < k_3$. One can easily verify that $\bar{a}_i \leq \bar{a}_j \leq \bar{a}_j$, $\bar{b}_j \leq \bar{b}_j \leq \bar{b}_i$ and

    (a) $C_{\bar{\mathbf{B}}'}(x) = \bar{h}_i = C_{\bar{\mathbf{B}}}(x), \forall x \in (\bar{a}_i, \bar{a}_j) \cup (\bar{b}_j, \bar{b}_i)$;

    (b) $C_{\bar{\mathbf{B}}'}(x) = \bar{h}_i + (\bar{h}_j - \bar{h}_i) + \bar{h}_i = \bar{h}_i + \bar{h}_j = C_{\bar{\mathbf{B}}}(x), \forall x \in (\bar{b}_i, \bar{b}_j)$;

   as $(\bar{a}_i, \bar{a}_j) \cup (\bar{b}_j, \bar{b}_i) \cup (\bar{b}_i, \bar{b}_j) = (\bar{a}_i, \bar{b}_i)$ in this case, $C_{\bar{\mathbf{B}}} = C_{\bar{\mathbf{B}}'}$. And $\sum_{\bar{B}'_i \in \bar{\mathbf{B}}'} h'_i = \bar{h}_i + (\bar{h}_j - \bar{h}_i) + \bar{h}_i = \bar{h}_i + \bar{h}_j = \sum_{B_i \in \bar{\mathbf{B}}} \bar{h}_i$, as Figure 4.2(b) shows.

3. $\bar{a}_j > \bar{a}_i, \bar{b}_j < \bar{b}_i, \bar{h}_j < \bar{h}_i$. This case is similar as case 2, and 3 new blocks are introduced but with different spans and heights: $\bar{B}_{k_1} = \langle \bar{a}_i, \bar{b}_j, \bar{h}_j \rangle$, $\bar{B}_{k_2} = \langle \bar{a}_j, \bar{b}_j, \bar{h}_i - \bar{h}_j \rangle$ and $\bar{B}_{k_3} = \langle \bar{a}_j, \bar{b}_i, \bar{h}_j \rangle$ with $k_1 < k_2 < k_3$. $\bar{a}_i \leq \bar{a}_j \leq \bar{a}_j$, $\bar{b}_j \leq \bar{b}_j \leq \bar{b}_i$ still stand and

    (a) $C_{\bar{\mathbf{B}}'}(x) = \bar{h}_j + (\bar{h}_i - \bar{h}_j) = \bar{h}_i = C_{\bar{\mathbf{B}}}(x), \forall x \in (\bar{a}_i, \bar{a}_j) \cup (\bar{b}_j, \bar{b}_i)$;

    (b) $C_{\bar{\mathbf{B}}'}(x) = \bar{h}_j + (\bar{h}_i - \bar{h}_j) + \bar{h}_j = \bar{h}_i + \bar{h}_j = C_{\bar{\mathbf{B}}}(x), \forall x \in (\bar{b}_i, \bar{b}_j)$;

   therefore, $C_{\bar{\mathbf{B}}} = C_{\bar{\mathbf{B}}'}$ stands for this case. And $\sum_{\bar{B}'_i \in \bar{\mathbf{B}}'} h'_i = \bar{h}_j + (\bar{h}_i - \bar{h}_j) + \bar{h}_j = \bar{h}_i + \bar{h}_j = \sum_{B_i \in \bar{\mathbf{B}}} \bar{h}_i$, as Figure 4.2(c) shows.

With the 3 cases shown above, it is clear that there exists $\bar{\mathbf{B}}$ which is equivalent to $\mathbf{B}$ and satisfies CB1: $\forall k \in [1, \bar{K} - 1], \bar{a}_k \leq \bar{a}_{k+1}, \bar{b}_k \leq \bar{b}_{k+1}$.

For CB2, it can be treated as the case when we have two blocks $\langle \bar{a}_1, \bar{b}_1, \bar{h}_1 \rangle$ and $\langle \bar{a}_{\bar{K}} - n, \bar{b}_{\bar{K}} - n, \bar{h}_{\bar{K}} \rangle$. It is clear that $\bar{a}_{\bar{K}} - n < 0 \leq \bar{a}_1$ and $\bar{b}_{\bar{K}} - n > \bar{b}_1$, and the same transformation in the 3 cases above can be still applied to make $\bar{b}_{\bar{K}} - n \leq \bar{b}_1$ satisfied. ■

We have already shown that the solution space of a CIBD problem becomes more organized by introducing the canonical blocksets. However, searching among the canonical blocksets is still too complicated. Suppose we have a number of $|\mathbf{B}|$ blocks in the solution represented by a canonical blockset and each block in the set is denoted by a triplet. Then we need $3|\mathbf{B}|$ variables to represent this solution. We may use the monotone property of canonical blockset to help the search, however, the size of the blockset could be large and we even don't know the exact number of $|\mathbf{B}|$.

In this section, we will show the one to one correspondence between canonical blocksets and *admissible function pairs*. And the later is consists of two monotonically non-decreasing functions and can be represented by $2n + w$ variables. We will also show how to further condense the representation of an admissible function pair into $2n$ variables and turn the whole problem into a convex cost integer dual network flow problem.

Again, we start with the definition of the admissible function pair. This definition is important as all the properties listed for admissible function pairs can converted into linear constraints later on.

For each canonical blockset $\mathbf{B} = \{B_1, B_2, \ldots, B_K\}$, a function pair $(\mathcal{L}, \mathcal{R})$ is defined, as follows:

$$\mathcal{L}(x) = \sum_{B_k \in \mathbf{B}, a_k \leq x} h_k, \ \forall x \in [0, n-1] \tag{4.4a}$$

$$\mathcal{R}(x) = \sum_{B_k \in \mathbf{B}, b_k \leq x} h_k, \ \forall x \in [0, n+w-1] \tag{4.4b}$$

Notice that $\mathcal{L}(n-1) = \sum_{k, a_k \leq n-1} h_k = \sum_{k=1}^{K} h_k = H_{\mathbf{B}}$. Also, by applying Equation (4.4) to Equation (4.3), we can represent $\mathcal{F}_{\mathbf{B}}(x)$ with function pair $(\mathcal{L}, \mathcal{R})$.

$$\mathcal{F}_{\mathbf{B}}(x) = \mathcal{F}_{(\mathcal{L},\mathcal{R})}(x) = \begin{cases} \sum_{k, a_k \leq x < b_k} h_k = \mathcal{L}(x) - \mathcal{R}(x), \ \forall x \in [w, n-1] \\ \sum_{k, a_k \leq x < b_k} h_k + \sum_{k, a_k \leq x+n < b_k} h_k = \mathcal{L}(x) - \mathcal{R}(x) \\ +\mathcal{L}(n-1) - \mathcal{R}(n+x), \ \forall x \in [1, w-1] \end{cases} \tag{4.5}$$

Definition 4.4. *A function pair* $(\mathcal{L}, \mathcal{R})$ *with* $\mathcal{L} : [0, n-1] \to \mathbb{Z}$ *and* $\mathcal{R} : [0, n+w-1] \to \mathbb{Z}$ *is* admissible *if and only if* $(\mathcal{L}, \mathcal{R})$ *satisfies the following properties:*

AD1: $\mathcal{L}$ *and* $\mathcal{R}$ *are non-negative,* $\mathcal{R}(0) = 0$*;*

AD2: $\mathcal{L}$ *and* $\mathcal{R}$ *are monotonically non-decreasing, i.e.* $\forall x \in [0, n-2], \mathcal{L}(x) \leq \mathcal{L}(x+1)$*;* $\forall x \in [0, n+w-2], \mathcal{R}(x) \leq \mathcal{R}(x+1)$*;*

AD3: $\forall x \in [0, n-1], \mathcal{L}(x) \geq \mathcal{R}(x)$*;* $\forall x \in [n, n+w-1], \mathcal{L}(n-1) \geq \mathcal{R}(x)$*; particularly,* $\mathcal{R}(n+w-1) = \mathcal{L}(n-1)$*;*

AD4: $\forall x \in [0, n-1]$, $\mathcal{L}(x) \leq \mathcal{R}(x+w)$*;*

AD5: $\forall x \in [0, n-1]$, $\mathcal{L}(x) \geq \mathcal{R}(x+1)$*;*

AD6: $\forall x \geq b_1 + n, \mathcal{R}(x) = \mathcal{L}(n-1)$, *where* $b_1 = \min \arg(\mathcal{R}(x) > 0)$.

In the second theorem we introduced in this section, we are going to show the one to one correspondence between canonical blocksets and admissible function pairs. The mapping between these two preserves the calculation of both the local sum of the block heights $\mathcal{F}_{\mathbf{B}}(x)$ and the total heights of blocks $H_{\mathbf{B}}$.

Theorem 4.2. *For any canonical blockset* $\mathbf{B}$*, we can find an admissible function pair* $(\mathcal{L}, \mathcal{R})$ *with* $\mathcal{F}_{\mathbf{B}}(x) = \mathcal{F}_{(\mathcal{L},\mathcal{R})}(x)$*,* $H_{\mathbf{B}} = \mathcal{L}(n-1)$*, and vice versa.*

Proof. The proof for Theorem 4.2 is constructive and we will prove it from both ways. First, starting from a canonical blockset $\mathbf{B}$, we will show the function pair $(\mathcal{L}, \mathcal{R})$ defined by $\mathbf{B}$ using Equation (4.4) is admissible. And second, starting from an admissible function pair $(\mathcal{L}, \mathcal{R})$, we will construct a canonical blockset $\mathbf{B}$ with $\mathcal{F}_{\mathbf{B}}(x) = \mathcal{F}_{(\mathcal{L},\mathcal{R})}(x)$, $H_{\mathbf{B}} = \mathcal{L}(n-1)$.

To prove that $(\mathcal{L}, \mathcal{R})$ defined by $\mathbf{B}$ using Equation (4.4) is admissible, we can verify the properties listed in Definition 4.4 one by one. Suppose function pair $(\mathcal{L}, \mathcal{R})$ is defined with canonical blockset $\mathbf{B} = \{\langle a_k, b_k, h_k\rangle | k \in [1, K]\}$,

1. According to the definition of $\mathcal{L}$ and $\mathcal{R}$, they are both defined as the sum of a set of non-negative values h_k, therefore, they are both non-negative. And as any feasible block $\langle a_k, b_k, h_k\rangle$ satisfies $b_k > 0$, $\mathcal{R}(0) = 0$;
2. Suppose we have $0 \le x_1 < x_2 \le n-1$, then it is clear that $\{k | a_k \le x_1\} \subseteq \{k | a_k \le x_2\}$, and as we know all $h_k > 0$, then we have $\mathcal{L}(x_1) = \sum_{k, a_k \le x_1} h_k \le \sum_{k, a_k \le x_2} h_k = \mathcal{L}(x_2)$. Therefore, we know $\mathcal{L}$ is monotonically non-decreasing in its domain. Similarly, we can prove $\mathcal{R}$ is also monotonically non-decreasing;
3. As any feasible block $\langle a_k, b_k, h_k\rangle$ satisfies $a_k < b_k$, $\{k | b_k \le x\} \subseteq \{k | a_k \le x\}$. Again, since we have any $h_k > 0$, we also have $\forall x \in [0, n-1]$, $\mathcal{L}(x) =$

$\sum_{k,a_k \le x} h_k \ge \sum_{k,b_k \le x} h_k = \mathcal{R}(x)$. In particular, $\mathcal{L}(n-1) = \sum_{k,a_k \le n-1} h_k = \sum_{k=1}^{K} h_k$ actually is sum of all h_ks in the blockset. Therefore, we have $\forall x, \mathcal{R}(x) \le \mathcal{L}(n-1)$, and $\mathcal{L}(x) \le \mathcal{L}(n-1)$ also stands. For the case $\mathcal{R}(n+w-1) = \mathcal{L}(n-1)$, it can be shown easily by the fact that $\forall k, a_k \le n-1, b_k \le n+w-1$;

4. According to the definition, a feasible block $\langle a_k, b_k, h_k \rangle$ also satisfies $b_k - a_k \le w$, therefore, $\{k | a_k \le x\} \subseteq \{k | b_k - w \le x\}$. That leads to $\forall x \in [0, n-1]$, $\mathcal{L}(x) = \sum_{k,a_k \le x} h_k \le \sum_{k,b_k - w \le x} h_k = \sum_{k,b_k \le x+w} h_k = \mathcal{R}(x+w)$;
5. This property actually stands for a trivial minimal window constraint $w_{min} = 1$. According to the definition of feasible blocks, we should have $b_k \ge a_k + 1$ and exclude any block with 0 width. Then $\{k | b_k - 1 \le x\} \subseteq \{k | a_k \le x\}$, and $\forall x \in [0, n-1]$, $\mathcal{L}(x) = \sum_{k,a_k \le x} h_k \ge \sum_{k,b_k - 1 \le x} h_k = \sum_{k,b_k \le x+1} h_k = \mathcal{R}(x+1)$;
6. As $b_1 = \min\arg(\mathcal{R} > 0) = \min\{b_k | k \in [1, K]\}$, and $\mathbf{B}$ is canonical, then $b_K = \max\{b_k | k \in [1, K]\} \le b_1 + n$, and $\forall x \ge b_1 + n$, $\mathcal{R}(x) = \sum_{k=1}^{K} h_k = \mathcal{L}(n-1)$.

Therefore, $(\mathcal{L}, \mathcal{R})$ satisfies all properties in Definition 4.4 and is admissible. $\mathcal{F}_{\mathbf{B}}(x) = \mathcal{F}_{(\mathcal{L},\mathcal{R})}(x)$ stands directly from the definition in Equation (4.5).

Given an admissible function pair $(\mathcal{L}, \mathcal{R})$, the canonical blockset $\mathbf{B}$ can be found with "horizontal rectangularization" (See Figure 4.3).

1. List all non-zero distinct values in $\mathcal{L}$ and $\mathcal{R}$ in ascending order as a list $\mathbb{L}$;
2. Set the current horizon as $\tilde{h} = 0$, $k = 1$;
3. Find the smallest number in $\mathbb{L}$ which is larger than $\tilde{h}$ as z;
4. Set $a_k = \arg\min x(\mathcal{L}(x) \ge z)$ and $b_k = \arg\min x(\mathcal{R}(x) \ge z)$; And we find a block $B_k = \langle a_k, b_k, h_k = z - \tilde{h} \rangle$, set $k = k + 1$.

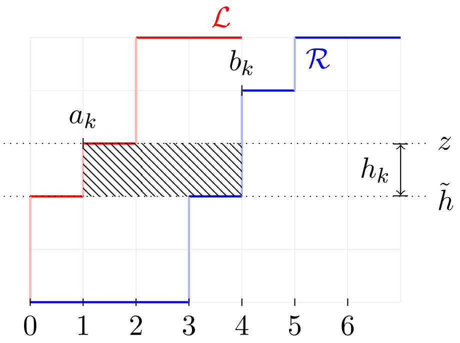

Figure 4.3: Illustration of applying horizontal rectangularization on $(\mathcal{L}, \mathcal{R})$. Simply speaking, for a given admissible function pair $(\mathcal{L}, \mathcal{R})$, we can find a set of horizontal lines by extending each horizontal "staircase" on function $\mathcal{L}$ or $\mathcal{R}$. And then find those blocks defined by adjacent horizontal lines and vertical "staircases" of $\mathcal{L}$ and $\mathcal{R}$.

5. Set $\tilde{h} = z$, and remove z from list $\mathbb{L}$. Return to step 3 until $\mathbb{L}$ is empty.

In order to show blockset $\mathbf{B} = \{B_k | k \in [1, K]\}$ found by algorithm "horizontal rectangularization" is canonical, notice that, the algorithm used a set of strictly ascending values in $\mathbb{L} = \{\mathcal{L}(x) | x \in [0, n-1]\} \cup \{\mathcal{R}(x) | x \in [0, n+w-1]\}$ together with the two monotonically non-descending rectilinear curves to form the blockset. This fact can easily leads to the properties that: (i) a_k and b_k are both non-descending; (ii) h_k are strictly positive. By given that $\mathcal{L}(n-1) = \mathcal{R}(n+w-1) = \max \mathbb{L}$, we can also notice that $0 \leq a_k \leq n-1$ and $0 \leq b_k \leq n+w-1$. Accompanied with the fact that $\forall x \in [0, n-1]$, $\mathcal{L}(x) \geq \mathcal{R}(x+1)$, $\mathcal{L}(b_k - 1) \geq \mathcal{R}(b_k)$, then we have $b_k - a_k \geq 1$; similarly, by using the property $\forall x \in [0, n-1]$, $\mathcal{L}(x) \leq \mathcal{R}(x+w)$, we can show that

$\mathcal{L}(a_k) \leq \mathcal{R}(a_k + w)$ and $b_k - a_k \leq w$.

For the last property $b_K - n \leq b_1$, if $(\mathcal{L}, \mathcal{R})$ satisfies $\forall x \geq b_1 + n, \mathcal{R}(x) = \mathcal{L}(n-1)$, it can be satisfied as $b_K = \arg\min x(\mathcal{R}(x) \geq \mathcal{L}(n-1)) \leq b_1 + n$. And $b_1 = \min\arg(\mathcal{R}(x) > 0)$ is just a trivial fact. Therefore, the blockset $\mathbf{B}$ formed by $(\mathcal{L}, \mathcal{R})$ that satisfies all properties listed in Definition 4.4 is canonical.

As shown in Figure 4.3, every vertical column locate at position x is defined by $\mathcal{L}(x)$ and $\mathcal{R}(x)$ (for the case $x \geq n$, it is defined by $\mathcal{L}(n-1)$ and $\mathcal{R}(x)$) will be partitioned to several blocks with $a_k \leq x$ and $b_k > x$. This makes Equation (4.5) go the opposite direction thus proves $\mathcal{F}_{\mathbf{B}}(x) = \mathcal{F}_{(\mathcal{L},\mathcal{R})}(x)$. And according to the fact $\mathcal{R}(0) = 0$, $\max(\mathbb{L}) = \mathcal{L}(n-1)$, we also have $\sum_k h_k = H_{\mathbf{B}} = \mathcal{L}(n-1)$. ■

Then, according to Theorem 4.2, the objective of the CIBD problem can be formulated as:

$$\begin{aligned}\min \mathcal{E}(\mathcal{L}, \mathcal{R}) = &\sum_{x=0}^{w-1} (\mathcal{L}(x) - \mathcal{R}(x) + \mathcal{L}(n-1) - \mathcal{R}(n+x) - t(x))^2 \\ &+ \sum_{x=w}^{n-1} (\mathcal{L}(x) - \mathcal{R}(x) - t(x))^2 \qquad (4.6)\end{aligned}$$

However, not all properties can be expressed with linear constraints defined with $(\mathcal{L}, \mathcal{R})$ since b_1 in (AD6) remains unknown until $(\mathcal{L}(x), \mathcal{R}(x))$ is known. Moreover, Equation (4.6) is not submodular since not all off-diagonal coefficients in the constraint matrix are non-positive with more than 2 variables in a single term of the quadratic objective function(Prop 2.6 [44]). Further the lack of submodularity makes this problem hard to solve.

We introduce the following transformation for admissible function pairs $(\mathcal{L}, \mathcal{R})$

to remove the variable b_1 from Equation (4.6):

$$\bar{\mathcal{R}}(x) = \begin{cases} \mathcal{R}(n+x) - \mathcal{L}(n-1),\ \forall x \in [0, b_1 - 1] \\ \\ \mathcal{R}(x),\ \forall x \in [b_1, n-1] \end{cases} \tag{4.7}$$

The CIBD problem is then formulated, as follows.

$$\min \mathcal{E}(\mathcal{L}, \bar{\mathcal{R}}) = \sum_{x=0}^{n-1} (\mathcal{L}(x) - \bar{\mathcal{R}}(x) - t(x))^2$$

$$\text{s.t.} \quad \mathcal{L}(x) \leq \mathcal{L}(x+1),\ \forall x \in [0, n-2] \tag{4.8a}$$

$$\bar{\mathcal{R}}(x) \leq \bar{\mathcal{R}}(x+1),\ \forall x \in [0, n-2] \tag{4.8b}$$

$$\mathcal{L}(x) \leq \bar{\mathcal{R}}(x+w),\ \forall x \in [0, n-w-1] \tag{4.8c}$$

$$\mathcal{L}(x) \leq \bar{\mathcal{R}}(x+w-n) + \mathcal{L}(n-1),\ \forall x \in [n-w, n-1] \tag{4.8d}$$

$$\bar{\mathcal{R}}(x) \leq \mathcal{L}(x-1),\ \forall x \in [1, n-1] \tag{4.8e}$$

$$\bar{\mathcal{R}}(0) \leq 0, \mathcal{L}(0) \geq 0, \mathcal{L}(n-1) \leq H \tag{4.8f}$$

To show that the CIBD problem can be correctly solved by find solutions to Equation (4.8), we need the following lemma.

Lemma 4.3. *For any admissible function pair* $(\mathcal{L}, \mathcal{R})$, $(\mathcal{L}, \bar{\mathcal{R}})$ *is feasible to Equation* (4.8) *with* $\mathcal{E}(\mathcal{L}, \mathcal{R}) = \mathcal{E}(\mathcal{L}, \bar{\mathcal{R}})$*; and for any feasible solution* $(\mathcal{L}, \bar{\mathcal{R}})$ *to Equation* (4.8), *there exist an admissible function pair* $(\mathcal{L}, \mathcal{R})$ *such that* $\mathcal{E}(\mathcal{L}, \mathcal{R}) = \mathcal{E}(\mathcal{L}, \bar{\mathcal{R}})$.

Proof. We start our proof from showing the one-to-one correspondence between admissible function pairs $(\mathcal{L}, \mathcal{R})$ and feasible solutions $(\mathcal{L}, \bar{\mathcal{R}})$ to Equation (4.8).

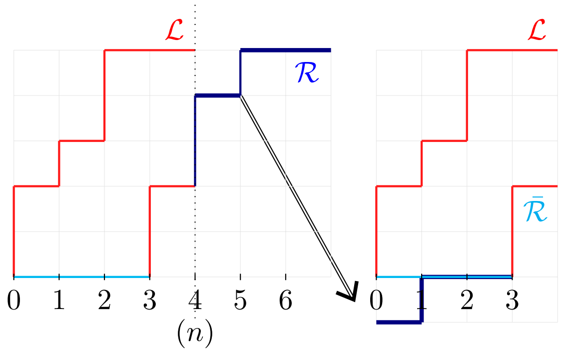

Figure 4.4: Visual illustration of mapping from $(\mathcal{L}, \mathcal{R})$ to $(\mathcal{L}, \bar{\mathcal{R}})$. In short, $(\mathcal{L}, \bar{\mathcal{R}})$ is obtained from $(\mathcal{L}, \mathcal{R})$ by shifting the part of $(\mathcal{L}, \mathcal{R})$ on the right of line $x = n$ with n units leftward and $\mathcal{L}(n-1)$ units downward.

According to Equation (4.7), any admissible function pairs $(\mathcal{L}, \mathcal{R})$ can be uniquely mapped to a solution $(\mathcal{L}, \bar{\mathcal{R}})$ by shifting $\mathcal{R}(x \in [n, n+w-1])$ n units leftward and $\mathcal{L}(n-1)$ units downward, as illustrated by Figure 4.4. Notice that, the domain of $\bar{\mathcal{R}}$ is reduced from $[0, n+w-1]$ to $[0, n-1]$ compared to $\mathcal{R}$ as the shifting operation overlapped the intervals $[0, w-1]$ and $[n, n+w-1]$. According to (AD6), $\forall x \in [0, b_1], \mathcal{R}(x) = 0$, and $\forall x \in [b_1, w-1], \mathcal{R}(n+x) = \mathcal{L}(n-1)$; i.e. $\forall x \in [0, w-1]$, either $\mathcal{R}(x) = 0$ or $\mathcal{R}(n+x) = \mathcal{L}(n-1)$ (or both). That serves as the key for making a unique mapping from $(\mathcal{L}, \bar{\mathcal{R}})$ back to $(\mathcal{L}, \mathcal{R})$ with the following equation:

$$\mathcal{R}(x) = \begin{cases} \bar{\mathcal{R}}(x),\ \ x \in [w, n-1] \text{ or } (x < w, \bar{\mathcal{R}}(x) \geq 0) \\ 0,\ \ x < w, \bar{\mathcal{R}}(x) < 0 \\ \mathcal{L}(n-1),\ \ x \geq n, \bar{\mathcal{R}}(x-n) \geq 0 \\ \mathcal{L}(n-1) + \bar{\mathcal{R}}(x-n),\ \ x \geq n, \bar{\mathcal{R}}(x-n) < 0 \end{cases} \tag{4.9}$$

Then we need to show all the properties of admissible functions pairs are properly encoded into the constraints in Equation (4.8). The verification is straightforward but tedious. Therefore, we only list the guidelines for the verfications here instead. Together with Equation (4.9), Equations (4.8a) and (4.8b) are used to enforce the non-decreasing property AD2; Equations (4.8c) and (4.8d) enforce the maximal window constraint AD4; Equation (4.8e) encodes AD5 which excludes infeasible blocks with 0 width; AD6 is enforced by $\bar{\mathcal{R}}(0) \leq 0$ based on Equations (4.7) and (4.9); the non-negativity AD1 can be inferred from $\mathcal{L}(0) \geq 0$, Equations (4.8a) and (4.8b); and $\mathcal{L}(n-1) \leq H$ is used to enforce the constraint on total height of blocks. AD3 is inferred by AD2 and AD5. ■

The optimization problem in Equation (4.8) is similar to the problem addressed by Ahuja's algorithm [1], except that the constraint matrices in Ahuja's problems are network matrices (i.e. every column contains two non-zero entries, one of them is +1, and the other is −1). The constraint matrices in Equation (4.8) are not network matrices unless $\mathcal{L}(n-1)$ is known. Thus, by enumerating $\mathcal{L}(n-1)$, Equation (4.8) can be solved in $\mathcal{O}(n^2 H \log n \log(nH))$ time. However, we can do much better by figuring out that $\mathcal{L}(n-1)$ can be determined in constant time $\mathcal{O}(1)$. To be more specific, we claim that $\mathcal{L}(n-1)$ can be assumed to be H in almost every cases.

Before proving this claim, we need to prove an additional lemma. As shown in [44, 34], a solution space $\mathbb{Z}^V$ is L$^\natural$-convex with unary linear constraints of forms $\mathbf{y}_u \leq c_u$ or $\mathbf{y}_u \geq d_u$, where $\mathbf{y} \in \mathbb{Z}^V$, u is an index of variable $\mathbf{y}$ and c_u, du are constants. Our task here is to prove that the L$^\natural$-convexity still holds with binary linear constraints of form $\mathbf{y}_u - \mathbf{y}_v \leq e_{uv}$, where u, v are indexes of variable $\mathbf{y}$ and e_{uv} is some constant.

Lemma 4.4. *A set $P = \{\mathbf{y} | \mathbf{y} \in \mathbb{Z}^V, \forall (u,v) \in E, \mathbf{y}_u - \mathbf{y}_v \leq e_{uv}\}$ is L$^\natural$-convex, i.e. set P satisfies **(SBS$^\natural$[Z])**(sec 5.5 [44])*

$$\textit{\textbf{(SBS}}^{\natural}\textit{\textbf{[Z])}}\ \mathbf{p},\mathbf{q} \in P \Rightarrow (\mathbf{p} - \alpha\mathbf{1}) \vee \mathbf{q}, \mathbf{p} \wedge (\mathbf{q} + \alpha\mathbf{1}) \in P\ (\forall \alpha \in \mathbf{Z}_+) \tag{4.10}$$

Proof. Suppose $\mathbf{p}, \mathbf{q} \in P$, and for an arbitrary constraint $C_{uv} : \mathbf{y}_u - \mathbf{y}_v \leq e_{uv}$, $\mathbf{p}_u - \mathbf{p}_v \leq e_{uv}$ and $\mathbf{q}_u - \mathbf{q}_v \leq e_{uv}$.

For $\mathbf{y} = (\mathbf{p} - \alpha\mathbf{1}) \vee \mathbf{q}$, $\mathbf{y}_u = \max\{\mathbf{p}_u - \alpha, \mathbf{q}_u\}$ and $\mathbf{y}_v = \max\{\mathbf{p}_v - \alpha, \mathbf{q}_v\}$, there are 4 cases on the value assignment:

1. $\mathbf{y}_u = \mathbf{p}_u - \alpha$ and $\mathbf{y}_v = \mathbf{p}_v - \alpha$, then $\mathbf{y}_u - \mathbf{y}_v = \mathbf{p}_u - \mathbf{p}_v \leq e_{uv}$.
2. $\mathbf{y}_u = \mathbf{p}_u - \alpha$ and $\mathbf{y}_v = \mathbf{q}_v$. Then $\mathbf{q}_v \geq \mathbf{p}_v - \alpha$, and $\mathbf{y}_u - \mathbf{y}_v = \mathbf{p}_u - \alpha - \mathbf{q}_v \leq \mathbf{p}_u - \alpha - (\mathbf{p}_v - \alpha) = \mathbf{p}_u - \mathbf{p}_v \leq e_{uv}$.
3. $\mathbf{y}_u = \mathbf{q}_u$ and $\mathbf{y}_v = \mathbf{p}_v - \alpha$. Then $\mathbf{p}_v - \alpha \geq \mathbf{q}_v$, and $\mathbf{y}_u - \mathbf{y}_v = \mathbf{q}_u - (\mathbf{p}_v - \alpha) \leq \mathbf{q}_u - \mathbf{q}_v \leq e_{uv}$.

4. $\mathbf{y}_u = \mathbf{q}_u$ and $\mathbf{y}_v = \mathbf{q}_v$, then $\mathbf{y}_u - \mathbf{y}_v = \mathbf{q}_u - \mathbf{q}_v \leq e_{uv}$.

For $\mathbf{y} = \mathbf{p} \wedge (\mathbf{q} + \alpha \mathbf{1})$, $\mathbf{y}_u = \min\{\mathbf{p}_u, \mathbf{q}_u + \alpha\}$ and $\mathbf{y}_v = \min\{\mathbf{p}_v, \mathbf{q}_v + \alpha\}$, there are also 4 cases on the value assignment:

1. $\mathbf{y}_u = \mathbf{q}_u + \alpha$ and $\mathbf{y}_v = \mathbf{q}_v + \alpha$, then $\mathbf{y}_u - \mathbf{y}_v = \mathbf{p}_u + \alpha - (\mathbf{p}_v + \alpha) \leq e_{uv}$.
2. $\mathbf{y}_u = \mathbf{p}_u + \alpha$ and $\mathbf{y}_v = \mathbf{q}_v$. Then $\mathbf{p}_u + \alpha \leq \mathbf{p}_v$, and $\mathbf{y}_u - \mathbf{y}_v = \mathbf{p}_u + \alpha - \mathbf{q}_v \leq \mathbf{q}_u - \mathbf{q}_v \leq e_{uv}$.
3. $\mathbf{y}_u = \mathbf{p}_u$ and $\mathbf{y}_v = \mathbf{q}_v + \alpha$. Then $\mathbf{q}_v + \alpha \leq \mathbf{p}_v$, and $\mathbf{y}_u - \mathbf{y}_v = \mathbf{p}_u - (\mathbf{q}_v + \alpha) \leq \mathbf{q}_u + \alpha - (\mathbf{q}_v + \alpha) = \mathbf{q}_u - \mathbf{q}_v \leq e_{uv}$.
4. $\mathbf{y}_u = \mathbf{q}_u$ and $\mathbf{y}_v = \mathbf{q}_v$, then $\mathbf{y}_u - \mathbf{y}_v = \mathbf{q}_u - \mathbf{q}_v \leq e_{uv}$.

Therefore, for arbitrary constraint $C_{uv} : \mathbf{y}_u - \mathbf{y}_v \leq e_{uv}$, if $\mathbf{p}, \mathbf{q}$ satisfy C_{uv}, then $(\mathbf{p} - \alpha\mathbf{1}) \vee \mathbf{q}, \mathbf{p} \wedge (\mathbf{q} + \alpha\mathbf{1})$ also satisfy C_{uv}. Thus $P = \{\mathbf{y} | \mathbf{y} \in \mathbb{Z}^V, \forall (u, v) \in E, \mathbf{y}_u - \mathbf{y}_v \leq e_{uv}\}$ is L$^\natural$-convex. ■

With the Lemma 4.4 proved, we can continue to show the key observation in this work. Simply speaking, we found that the optimal solutions tend to make the total height of blocks as high as possible.

Theorem 4.5. *If there exist some feasible solution to Equation* (4.8)*, i.e. dom* $\mathcal{E} \neq \emptyset$*, and* $H \leq \sum_{x=0}^{n-1} t(x)$*, then there exist a solution* $\mathbf{y}^* = (\mathcal{L}^*, \bar{\mathcal{R}}^*)$ *such that* $\mathcal{L}^*(n-1) = H$ *and* $\forall \mathbf{y} \in$ *dom* $\mathcal{E}$, $\mathcal{E}(\mathbf{y}^*) \leq \mathcal{E}(\mathbf{y})$.

Proof. Theorem 4.5 can be proved in a constructive way, i.e. suppose there exist some other optimal solution $\mathbf{y}' = (\mathcal{L}', \bar{\mathcal{R}}')$ such that $H' = \mathcal{L}'(n-1) \leq H$ and $\forall \mathbf{y} \in$ dom $\mathcal{E}$, $\mathcal{E}(\mathbf{y}') \leq \mathcal{E}(\mathbf{y})$, then we can find another solution $\mathbf{y}^* = (\mathcal{L}^*, \bar{\mathcal{R}}^*)$ with $\mathcal{L}^*(n-1) = H$

and $\mathcal{E}(\mathbf{y}^*) \leq \mathcal{E}(\mathbf{y}')$.

The construction of $\mathbf{y}^*$ differs in two different cases. For the first case, if $H \leq \sum_{x=0}^{n-1}(\mathcal{L}'(x) - \bar{\mathcal{R}}'(x))$, set $\mathbf{y}^* = (\mathcal{L}' + \delta, \bar{\mathcal{R}}' + \delta)$, where

$$\delta(x) = \begin{cases} \min\{-\bar{\mathcal{R}}'(0), H - H'\} & x = 0 \\ \\ \min\{\mathcal{L}'(x-1) - \bar{\mathcal{R}}'(x) + \delta(x-1), H - H'\}, & x > 0 \end{cases} \tag{4.11}$$

Essentially, the function δ is applied to $\mathbf{y}'$ in order to make the new solution $\mathbf{y}^* = (\mathcal{L}^*, \bar{\mathcal{R}}^*)$ satisfy $\mathcal{L}^*(n-1) = H$ without changing the objective value while preserving all the constraints.

Notice that, $\forall x > 0$, $\delta(x) = \min\{\mathcal{L}'(x-1) - \bar{\mathcal{R}}'(x) + \delta(x-1), H - H'\}$. If $\forall x > 0, \delta(x) = \mathcal{L}'(x-1) - \bar{\mathcal{R}}'(x) + \delta(x-1)$, according to Equation (4.8e), $\delta(x) \geq \delta(x-1)$; Otherwise, $\delta(x) = H - H'$. And according to Equation (4.11), $\forall x, \delta(x) \leq H - H'$, then $\delta(x) \geq \delta(x-1)$ still stands. Therefore, δ is an monotonically non-decreasing function on $[0, n-1]$. Also, as $\bar{\mathcal{R}}'(0) \leq 0$ and $H \geq H'$, $\delta(0) \geq 0$. That shows δ is a nonnegative function.

Now we can show how $\mathbf{y}^* = (\mathcal{L}' + \delta, \bar{\mathcal{R}}' + \delta)$ preserves the constraints listed in Equation (4.8).

For Equation (4.8a), since $\forall x \in [0, n-2], \mathcal{L}'(x) \leq \mathcal{L}'(x+1)$ and $\delta(x) \leq \delta(x+1)$, we have $\mathcal{L}'(x) + \delta(x) = \mathcal{L}^*(x) \leq \mathcal{L}'(x+1) + \delta(x+1) = \mathcal{L}^*(x+1)$. This shows Equation (4.8a) stands for solution $\mathbf{y}^*$. We can also prove the inequality for Equation (4.8b) and (4.8c) on $\mathbf{y}^*$ using a similar method.

For Equation (4.8d), $\forall x \in [n-w, n-1], \mathcal{L}'(x) \leq \bar{\mathcal{R}}'(x+w-n) + \mathcal{L}'(n-1)$, and clearly $\delta(x) \leq \delta(n-1) \leq \delta(x+w-n) + \delta(n-1)$. This shows $\mathcal{L}^*(x) \leq$

$\bar{\mathcal{R}}^*(x+w-n)+\mathcal{L}^*(n-1)$.

For Equation (4.8e), based on the definition of $\delta(x)$, we have $\bar{\mathcal{R}}^*(x)=\bar{\mathcal{R}}'(x)+\delta(x)\leq\bar{\mathcal{R}}'(x)+\mathcal{L}'(x-1)-\bar{\mathcal{R}}'(x)+\delta(x-1)=\mathcal{L}'(x-1)+\delta(x-1)=\mathcal{L}^*(x-1)$.

For the last inequality, $\bar{\mathcal{R}}^*(0)=\bar{\mathcal{R}}'(0)+\delta(0)\leq\bar{\mathcal{R}}'(0)-\bar{\mathcal{R}}'(0)=0$. $\mathcal{L}(n-1)\leq H$ is also satisfied as $\mathcal{L}^*(0)=\mathcal{L}'(0)+\delta(0)\geq\mathcal{L}'(0)\geq 0$. And $\mathcal{L}^*(n-1)=\mathcal{L}^(n-1)+\delta(n-1)$. Suppose $\delta(n-1)=H-H'$, then $\mathcal{L}^*(n-1)=H$ and $\mathcal{L}(n-1)\leq H$ is satisfied. Otherwise, $\delta(n-1)<H-H'$ and $\forall x\in[0,n-1],\delta(x)<H-H'$. Then $\delta(n-1)=\sum_{x=0}^{n-1}\left(\mathcal{L}'(x)-\bar{\mathcal{R}}'(x)\right)-\mathcal{L}'(n-1)\geq H-H'$ and this contradicts with the previous assumption. Therefore, $\mathcal{L}^*(n-1)=H$ whenever $H\leq\sum_{x=0}^{n-1}(\mathcal{L}'(x)-\bar{\mathcal{R}}'(x))$.

For the second case where $H>\sum_{x=0}^{n-1}(\mathcal{L}'(x)-\bar{\mathcal{R}}'(x))$, set $\mathbf{y}''=(\mathcal{L}'',\bar{\mathcal{R}}'')=(\mathcal{L}'+\delta,\bar{\mathcal{R}}'+\delta)$. Then, $\bar{\mathcal{R}}''(0)=0$ and $\forall x\in[0,n-1],\bar{\mathcal{R}}''(x)=\mathcal{L}''(x-1)$ (define $\mathcal{L}''(-1)=0$), and solution $\mathbf{y}''=(\mathcal{L}'',\bar{\mathcal{R}}'')$ will satisfy

$$\min\mathcal{E}'(\mathcal{L})=\sum_{x=0}^{n-1}(\mathcal{L}(x)-\mathcal{L}(x-1)-f(x))^2$$

$$\text{s.t.}\quad \mathcal{L}(x-1)-\mathcal{L}(x)\leq 0,\ \forall x\in[0,n-1] \tag{4.12a}$$

$$\mathcal{L}(n-1)\leq H \tag{4.12b}$$

$$\mathcal{L}(-1)=0 \tag{4.12c}$$

And $\mathcal{E}'(\mathcal{L}'')=\mathcal{E}(\mathcal{L}',\bar{\mathcal{R}}')$. By relaxing constraint in Equation (4.12c), Equation (4.12) is further degenerated to

$$\min\mathcal{E}''(\mathcal{L})=\sum_{x=0}^{n-1}(\mathcal{L}(x)-\mathcal{L}(x-1)-f(x))^2$$

$$\text{s.t.} \quad \mathcal{L}(x-1) - \mathcal{L}(x) \leq 0, \ \forall x \in [0, n-1] \tag{4.13a}$$

$$\mathcal{L}(n-1) \leq H \tag{4.13b}$$

It is easy to show that dom $(\mathcal{E}') \subset$ dom $(\mathcal{E}'')$ and $\forall \mathcal{L} \in$ dom $(\mathcal{E}'), \mathcal{E}'(\mathcal{L}) = \mathcal{E}''(\mathcal{L})$. Moreover, if $\mathcal{L} \in$ dom $(\mathcal{E}'')$ and $\mathcal{L}(-1) = 0$, then $\mathcal{L} \in$ dom $(\mathcal{E}')$.

Set $\mathcal{L}^\circ(n-1) = H$, finding the solution $\mathcal{L}^\circ$ with $\mathcal{E}''(\mathcal{L}^\circ) = 0$ to Equation (4.13) can be done with an intuitive linear time algorithm. According to Lemma 4.4, the domain of Equation (4.13) is $\mathrm{L}^\natural$-convex, and Equation (4.13) is $\mathrm{L}^\natural$-convex (sec 7.3 [44]) and

$$\mathcal{E}''(\mathcal{L}'') + \mathcal{E}''(\mathcal{L}^\circ) \geq \mathcal{E}''(\mathcal{L}'' \vee \mathcal{L}^\circ) + \mathcal{E}''(\mathcal{L}'' \wedge \mathcal{L}^\circ) \tag{4.14}$$

As $\mathcal{E}''(\mathcal{L}^\circ) = 0$ and $\mathcal{E}''(\mathcal{L}'' \wedge \mathcal{L}^\circ) \geq 0$, $\mathcal{E}''(\mathcal{L}'') \geq \mathcal{E}''(\mathcal{L}'' \vee \mathcal{L}^\circ)$.

Notice that $\mathcal{L}'', \mathcal{L}^\circ \in$ dom $(\mathcal{E}'') \Rightarrow (\mathcal{L}'' \vee \mathcal{L}^\circ) \in$ dom $(\mathcal{E}'')$. Since $H \leq \sum_{x=0}^{n-1} f(x)$, $\mathcal{L}^\circ(-1) \leq 0$ and $\mathcal{L}'' \in$ dom $(\mathcal{E}')$, $(\mathcal{L}'' \vee \mathcal{L}^\circ)(-1) = \mathcal{L}''(-1) = 0$. This shows that $(\mathcal{L}'' \vee \mathcal{L}^\circ) \in$ dom $(\mathcal{E}')$ and $\mathcal{E}(\mathcal{L}', \bar{\mathcal{R}}') = \mathcal{E}'(\mathcal{L}'') \geq \mathcal{E}'(\mathcal{L}'' \vee \mathcal{L}^\circ)$. Thus, $\mathbf{y}^* = (\mathcal{L}^*, \bar{\mathcal{R}}^*)$ can be assigned with $\forall x \in [0, n-1], \mathcal{L}^*(x) = (\mathcal{L}'' \vee \mathcal{L}^\circ)(x), \bar{\mathcal{R}}^*(x) = (\mathcal{L}'' \vee \mathcal{L}^\circ)(x-1)$. Clearly, $\mathcal{L}^*(n-1) = \mathcal{L}^\circ(n-1) = H$, and $\forall \mathbf{y} \in$ dom $\mathcal{E}$, $\mathcal{E}(\mathbf{y}^*) = \mathcal{E}'(\mathcal{L}'' \vee \mathcal{L}^\circ) \leq \mathcal{E}'(\mathcal{L}'') = \mathcal{E}(\mathbf{y}') \leq \mathcal{E}(\mathbf{y})$.

Thus, for any optimal solution to Equation (4.8), there exists an optimal solution to Equation (4.8) with $\mathcal{L}(n-1) = H$. That is, whenever dom $(\mathcal{E}) \neq \emptyset$, there exists an optimal solution to Equation (4.8) with $\mathcal{L}(n-1) = H$. ■

According to Theorem 4.5, whenever $H \leq \sum_{x=0}^{n-1} t(x)$, Equation (4.8) can be solved by setting $\mathcal{L}(n-1) = H$. And setting $\mathcal{L}(n-1) = H$ makes Equation (4.8) an instance of convex cost integer dual network flow problem, which can be solved in time $\mathcal{O}(n^2 \log n \log(nH))$ for this case [1]. If $H > \sum_{x=0}^{n-1} t(x)$, it can be intuitively solved in linear time.

4.2.2 Solving CIBD with scaled local graph search

The algorithm we used for implementation is different from the one presented in section 4.2.1. Theoretically, CIBD problems can be solved in $\mathcal{O}(n^2 \log n \log(nH))$ with Ahuja's algorithm [1]. However, as mentioned by Kolmogorov *et al.*, this algorithm is complicated and is not expected to run fast in practice, another choice for solving Equation (4.8) is adopting the proximity scaling and local searching framework [34]. In this section, we introduced a specialized local step named Scaled Local Graph Search, which is inspired by graph search technique [70]. Each single local searching step takes $\mathcal{T}(n, n)$ which is the running time for a maximal flow on a graph with $\mathcal{O}(n)$ nodes and $\mathcal{O}(n)$ arcs. The overall running time for the latter algorithm is $n\big(n, n\big)$. In this work, we used a push-relabel implementation [24] and the whole algorithm runs in time $\mathcal{O}(n^3 \log n \log H)$. Although the theoretical complexity of the latter algorithm is worse than the previous one, it is easier to implement and is performing well in practice.

The scaled local graph search algorithm we introduced here is slightly generalized such that it works for any optimization that can be described by Equation (4.15).

$$\min \mathcal{E}(\mathbf{y}) = \sum_{(u,v)\in E'} f_{uv}(s\mathbf{y}_u - s\mathbf{y}_v - e'_{uv})$$

$$\text{s.t.} \quad s\mathbf{y}_u - s\mathbf{y}_v \leq e_{uv} \qquad \forall (u, v) \in E \tag{4.15a}$$

$$\mathbf{y}^{\circ} \preceq \mathbf{y} \preceq \mathbf{y}^{\circ} + \mathbf{1} \tag{4.15b}$$

where $f_{uv}(\cdot)$ is a convex function with $\arg\min f_{uv} = 0$ and $f_{uv}(0) \geq 0$. $\mathbf{y}^{\circ}$ is the lower bound of the local searching area and s is the scaling factor.

Recall that the essence of graph search technique is encoding the solution into a minimum s-excess problem and in this case minimum s-t cut problem as no unary term exists in the objective, and the graph construction for this problem is consisted of two parts: encoding hard constraints and encoding the objective.

The key point for encoding hard constraints into the graph is the mapping. This includes mapping feasible solutions into cuts with finite costs and mapping infeasible solutions into cuts with infinite costs. Consider a single constraint $s\mathbf{y}_u - s\mathbf{y}_v \leq e_{uv}$, variable $\mathbf{y}_u$ may choose from two values $\mathbf{y}_u^{\circ}$ or $\mathbf{y}_u^{\circ} + 1$, and the case for variable $\mathbf{y}_v$ is similar. Therefore, we have at most 4 different assignments for $\mathbf{y}_u$ and $\mathbf{y}_v$.

We distinguish 4 different cases based on the value of $\Delta_{uv} = s\mathbf{y}_u^{\circ} - s\mathbf{y}_v^{\circ} - e_{uv}$. A subgraph is constructed for each case as shown in Figure 4.5. There are three types of nodes in these subgraphs (i) S: source; (ii) T: sink; and (iii) $I(u, \mathbf{y}_u^{\circ})$: internal node locate at column u, with value assignment $\mathbf{y}_u = \mathbf{y}_u^{\circ}$. Dotted arcs stands for arcs with $+\infty$ costs.

1. $\Delta_{uv} \leq -s$. In this case, the constraint $s\mathbf{y}_u - s\mathbf{y}_v \leq e_{uv}$ will always be satisfied. Therefore, we only need a basic graph that can ensure all the interal nodes at

the lower level will be included in the source-side cut.

2. $-s < \Delta_{uv} \leq 0$. The only infeasible assignment in this case is $\mathbf{y}_u = \mathbf{y}_u^\circ + 1, \mathbf{y}_v = \mathbf{y}_v^\circ$. To make this case into an infinity cost s-t cut, we introduced an arc $I(u, \mathbf{y}_u^\circ + 1) \rightarrow I(v, \mathbf{y}_v^\circ + 1)$.
3. $0 < \Delta_{uv} \leq s$. $\mathbf{y}_u = \mathbf{y}_u^\circ, \mathbf{y}_v = \mathbf{y}_v^\circ + 1$ is the only feasible assignment in this case. Therefore, we add a source chain to include these two nodes: $S \rightarrow I(u, \mathbf{y}_u^\circ) \rightarrow I(v, \mathbf{y}_v^\circ + 1)$. And a sink link $I(u, \mathbf{y}_u^\circ + 1) \rightarrow T$ is used to exclude $\mathbf{y}_u = \mathbf{y}_u^\circ + 1$.
4. $\Delta_{uv} > s$. This is an infeasible case. The constraint can never be satisfied in any assignment. Therefore, we use a link $S \rightarrow T$ to show that it is always infeasible.

Objectives work like soft constraints. Instead of using $+\infty$ cost arcs, we use arcs with finite cost to penalize any value assignments that increase the objective. Simply speaking, we map a solution with objective value C into a minimal s-t cut with cost C. We achieve this goal by construct a subgraph for each term in the objective.

For each $(u, v) \in E'$, denote $\Delta'_{uv} = \mathbf{y}_u - \mathbf{y}_v - e'_{uv}$. Consider the term $f_{uv}(s\mathbf{y}_u - s\mathbf{y}_v - e'_{uv})$, the possible contributions of this term to the objective are listed in Table 4.1. As shown in table, variable $\mathbf{y}_u$ can take either $\mathbf{y}_u^\circ$ or $\mathbf{y}_u^\circ + 1$; while variable $\mathbf{y}_v$ can take either $\mathbf{y}_v^\circ$ or $\mathbf{y}_v^\circ + 1$. The 4 combinations yield 3 different objective values.

What we need to do is mapping these values to the corresponding variable assignments in the form of cuts. Again, like what we did for the hard constraints, we distinguish between 4 cases based on the value of Δ'_{uv}. A subgraph is constructed for

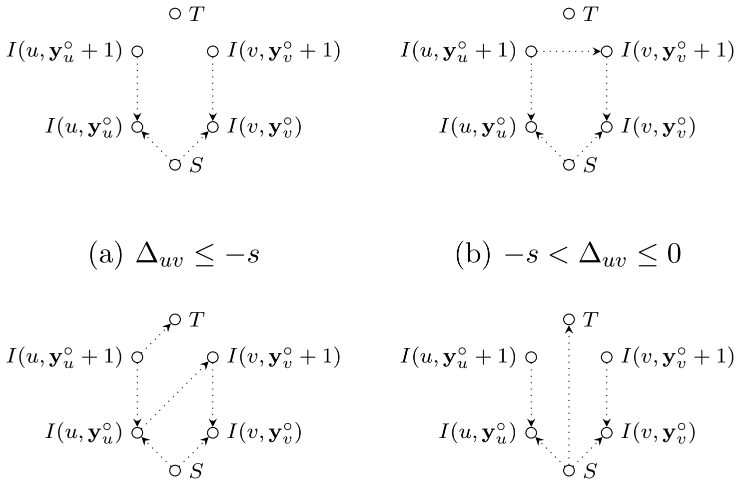

(a) $\Delta_{uv} \leq -s$ (b) $-s < \Delta_{uv} \leq 0$

(c) $0 < \Delta_{uv} \leq s$ (d) $\Delta_{uv} > s$

Figure 4.5: Encoding hard constraints in scaled local graph search. Each internal node $I(u, \mathbf{y}_u^\circ)$ stands for a variable assignment $\mathbf{y}_u = \mathbf{y}_u^\circ$. $s \geq 1$ is the scaling factor. S, T are special nodes stand for virtual source and sink. Dotted edges stand for arcs with $+\infty$ cost.

Table 4.1: Mapping between the objective values and the variable assignments.

		$\mathbf{y}_v$	
		$\mathbf{y}_v^\circ$	$\mathbf{y}_v^\circ + 1$
$\mathbf{y}_u$	$\mathbf{y}_u^\circ$	$f_{uv}(\Delta'_{uv})$	$f_{uv}(\Delta'_{uv} - s)$
	$\mathbf{y}_u^\circ + 1$	$f_{uv}(\Delta'_{uv} + s)$	$f_{uv}(\Delta'_{uv})$

each case as shown in Figure 4.6. The reason that we cannot use a universal subgraph for all 4 cases is: arc costs cannot be negative.

Take Figure 4.6(a) as an example. First, we need to verify whether every cost on the arcs are non-negative. It is easy to tell that $a3 = f_{uv}(\Delta'_{uv} + s) \geq f_{uv}(0) \geq 0$ according to our assumption. $a1 = a2 = f_{uv}(\Delta'_{uv}) - f_{uv}(\Delta'_{uv} + s) \geq 0$ because of $\Delta'_{uv} \leq \Delta'_{uv} + s \leq 0$, and f_{uv} is monotonically decreasing on interval $(-\infty, 0]$. We can also directly apply the convex property of f_{uv} to prove $a4 = f_{uv}(\Delta'_{uv} - s) + f_{uv}(\Delta'_{uv} + s) - 2f_{uv}(\Delta'_{uv}) \geq 0$. Proves for other graphs in Figure 4.6 are similar and the key points hinge on the convexity of f_{uv} and the fact $f_{uv}(0)$ is the global minimum of f_{uv}.

Then, we need to verify whether the cut values equal the corresponding objective values as shown in Table 4.1. The verification is straightforward:

1. $\mathbf{y}_u = \mathbf{y}_u^\circ$, $\mathbf{y}_v = \mathbf{y}_v^\circ$. The cut value is $a2 + a3 = f_{uv}(\Delta')$.
2. $\mathbf{y}_u = \mathbf{y}_u^\circ$, $\mathbf{y}_v = \mathbf{y}_v^\circ + 1$. The cut value is $a3 = f_{uv}(\Delta' + s)$.
3. $\mathbf{y}_u = \mathbf{y}_u^\circ + 1$, $\mathbf{y}_v = \mathbf{y}_v^\circ$. The cut value is $a1 + a2 + a3 + a4 = f_{uv}(\Delta' - s)$.
4. $\mathbf{y}_u = \mathbf{y}_u^\circ + 1$, $\mathbf{y}_v = \mathbf{y}_v^\circ + 1$. The cut value is $a1 + a3 = f_{uv}(\Delta')$.

The verifications are similar for the other graphs in Figure 4.6, therefore we omit the proofs here.

By encoding the hard constraints and the objective into a s-t min-cut problem, each local step in the proximity scaling and local search framework can be solved by solving a single maximal flow. Compared to the original graph search method, the scaled local graph search fully utilized the power of scaling and local search method, reducing the number of arcs between each column to $\mathcal{O}(1)$ and and makes the number of arcs become independent of the value e'_{uv}.

Experiments showed that CIBD algorithm can solve problems with $n = 72$ emission angles with around 1 second with $H = 10,000$ discrete time levels. [40]

4.3 Optimal sequencing with numerical optimization

While the algorithm introduced in section 4.2 can solve the optimal sequencing problems efficiently both theoretically and pragmatically, it has a drawback. The CIBD algorithm requires an explicit time limit on each dwell position. With this limitation, CIBD algorithm cannot guarantee a global solution if the time constraint is set as a sum over all dwell positions, which is a common practice in real cases. There is no current solution to extend CIBD algorithm into multiple dwell positions with global optimality guarantee, because the delivery time prediction Theorem 4.5 does not work for multiple dwell positions. To overcome this difficulty, an numerical approach will be used instead in this section.

Although CIBD cannot be applied to multiple dwell positions directly, several

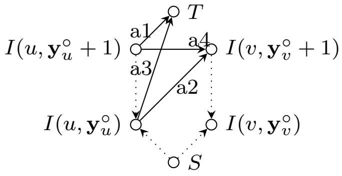

a1: $f_{uv}(\Delta'_{uv}) - f_{uv}(\Delta'_{uv} + s)$
a2: $f_{uv}(\Delta'_{uv}) - f_{uv}(\Delta'_{uv} + s)$
a3: $f_{uv}(\Delta'_{uv} + s)$
a4: $f_{uv}(\Delta'_{uv} - s) + f_{uv}(\Delta'_{uv} + s) - 2f_{uv}(\Delta'_{uv})$

(a) $\Delta'_{uv} \leq -s$

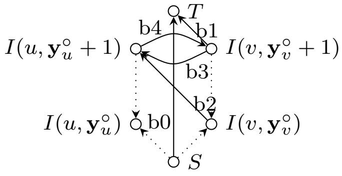

b0: $f_{uv}(0)$
b1: $f_{uv}(\Delta'_{uv}) - f_{uv}(0)$
b2: $f_{uv}(\Delta'_{uv}) - f_{uv}(0)$
b3: $f_{uv}(\Delta'_{uv} - s) + f_{uv}(0) - 2f_{uv}(\Delta'_{uv})$
b4: $f_{uv}(\Delta'_{uv} + s) - f_{uv}(0)$

(b) $-s < \Delta'_{uv} \leq 0$

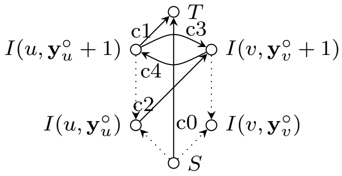

c0: $f_{uv}(0)$
c1: $f_{uv}(\Delta'_{uv}) - f_{uv}(0)$
c2: $f_{uv}(\Delta'_{uv}) - f_{uv}(0)$
c3: $f_{uv}(\Delta'_{uv} + s) + f_{uv}(0) - 2f_{uv}(\Delta'_{uv})$
c4: $f_{uv}(\Delta'_{uv} - s) - f_{uv}(0)$

(c) $0 < \Delta_{uv} \leq s$

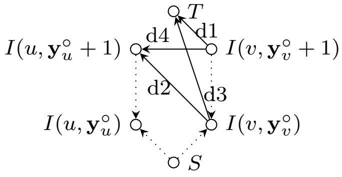

d1: $f_{uv}(\Delta'_{uv}) - f_{uv}(\Delta'_{uv} - s)$
d2: $f_{uv}(\Delta'_{uv}) - f_{uv}(\Delta'_{uv} - s)$
d3: $f_{uv}(\Delta'_{uv} - s)$
d4: $f_{uv}(\Delta'_{uv} - s) + f_{uv}(\Delta'_{uv} + s) - 2f_{uv}(\Delta'_{uv})$

(d) $\Delta_{uv} > s$

Figure 4.6: Encoding objectives in scaled local graph search. Each internal node $I(u, \mathbf{y}_u^\circ)$ stands for a variable assignment $\mathbf{y}_u = \mathbf{y}_u^\circ$. $s \geq 1$ is the scaling factor. S, T are special nodes stands for virtual source and sink. Dotted arcs stands for arcs with $+\infty$ cost. Arcs with finite costs are denoted by solid edges, and costs are marked beside the corresponding arcs.

conclusions can be still adopted. According to the study in section 4.2, for each dwell position, the sequencing can be determined by tracking the motion of the leading and trailing field edge. The optimal sequencing can make the following assumptions without affecting the delivery time or the dose distribution [40]: (i) the rotation of the leading and trailing field edge is limited to a single full rotation (360°), (ii) the leading field edge starts from 0°, and (iii) the rotation is counterclockwise.

Therefore, for any given dwell position $\vec{s}_j$, denote $x_{j,k}$, $y_{j,k}$ as the time points when the leading field edge and trailing field edge align with the azimuth $(k+1)\delta\varphi$, respectively. The dose received by sector$k$ (the region covered by beamlet $\dot{D}_i(j,k)$) is equivalent to the dose contribution from $\dot{D}_i(j,k)$ with dwell time $t_{j,k}$:

$$t_{j,k} = \begin{cases} x_{j,k} - y_{j,k}, & \text{if sector } k \text{ is not included in the initial opening} \\ x_{j,k} - y_{j,k} + T_j, & \text{otherwise} \end{cases} \tag{4.16}$$

where the initial opening refers to the region between the leading field edge and the trailing field edge at time point 0 for each dwell position, and T_j is the total dwell time at position $\vec{s}_j$. By allowing $y_{j,k} < 0$ and interpreted as $T_j - y_{j,k}$, the two cases are unified to: $t_{j,k} = x_{j,k} - y_{j,k}$. [40]

It is clear that if $t_{j,k} = \tau_{j,k}$ for all j and k, then the dose distribution of the anchor plan will be perfectly reproduced. Thus, an expedient treatment plan with a delivery time budget of T_{max} was rapidly generated from the anchor plan by solving the following optimization problem:

$$\min \sum_{j=0}^{J-1} \sum_{k=0}^{K-1} \left(\lambda_{j,k}^{-} H(\tau_{j,k} - t_{j,k}) + \lambda_{j,k}^{+} H(t_{j,k} - \tau_{j,k})\right) (t_{j,k} - \tau_{j,k})^2$$

$$\text{subject to } x_{j,k} \leq x_{j,k+1}, \forall j \in [0, J-1], k \in [0, K-2] \tag{4.17a}$$

$$y_{j,k} \leq y_{j,k+1}, \forall j \in [0, J-1], k \in [0, K-2] \tag{4.17b}$$

$$x_{j,k} \leq y_{j,k+w}, \forall j \in [0, J-1], k \in [0, K-w-1] \tag{4.17c}$$

$$x_{j,k} \leq y_{j,k+w-K} + T_j, \forall j \in [0, J-1], k \in [K-w, K-1] \tag{4.17d}$$

$$y_{j,k} \leq x_{j,k-1}, \forall j \in [0, J-1], k \in [1, K-1] \tag{4.17e}$$

$$y_{j,0} \leq 0, x_{j,0} \geq 0, x_{j,K-1} \leq T_j, \forall j \in [0, J-1] \tag{4.17f}$$

$$\sum_{j=0}^{J-1} T_j \leq T_{max} \tag{4.17g}$$

In Equation (4.17), constraints (4.17a) and (4.17b) refer to the non-decreasing nature of the time sequence; constraints (4.17c) and (4.17d) ensure that the resulting solution keeps the azimuthal emission angle less than the maximal azimuthal emission angle; constraint (4.17e) is used to exclude the case with azimuthal emission angle 0°; constraints (4.17f) and (4.17g) limit the delivery time below the given budget.

With a sufficient delivery time budget T_{max}, solving the optimal sequencing problem as described in Equation (4.17) can generate a perfect reproduction of the anchor plan. For example, if T_{max} is set to the delivery time of the corresponding anchor plan, the anchor plan itself is a trivial solution to Equation (4.17). However, as the delivery time budget T_{max} decreases, the solution to the optimal sequencing problem tends to use more beamlets with larger azimuthal emission angles and a perfect reproduction of the anchor plan may not be achieved in such cases. As a result, the expedient plan may be regarded as an approximation of the dose-volume optimized anchor plan. The delivery plan generated by solving Equation (4.17) is then scaled to make sure that no delivery time constraint and OAR tolerances are violated.

4.4 Results

The D-RSBT optimization took about 10 minutes including the time used to generate an anchor plan with ADOT, which is roughly the same level as S-RSBT which took 8 minutes. The IS+ICBT optimization took about 4 minutes.

The delivery efficiency curves for each patient plan using the D-RSBT and S-RSBT methods are shown in Figure 4.7, and the plans of IS+ICBT are explicitly labeled as such.

As shown in Figure 4.7, both D-RSBT and S-RSBT can achieve a higher D_{90} than IS+ICBT with a longer delivery time. Roughly speaking, D-RSBT has a better performance than S-RSBT with sufficient delivery time ~20 min/fx. However, it may not be a good choice if less than 20 min/fx is required. More specifically, with delivery time 20–25 min/fx, D-RSBT achieves 1 Gy higher D_{90} than S-RSBT; with delivery time 25–30 min/fx, the D_{90} increase becomes 10 Gy (see Table 4.7) And more detailed quantitative results are shown in Tables 4.2 – 4.6.

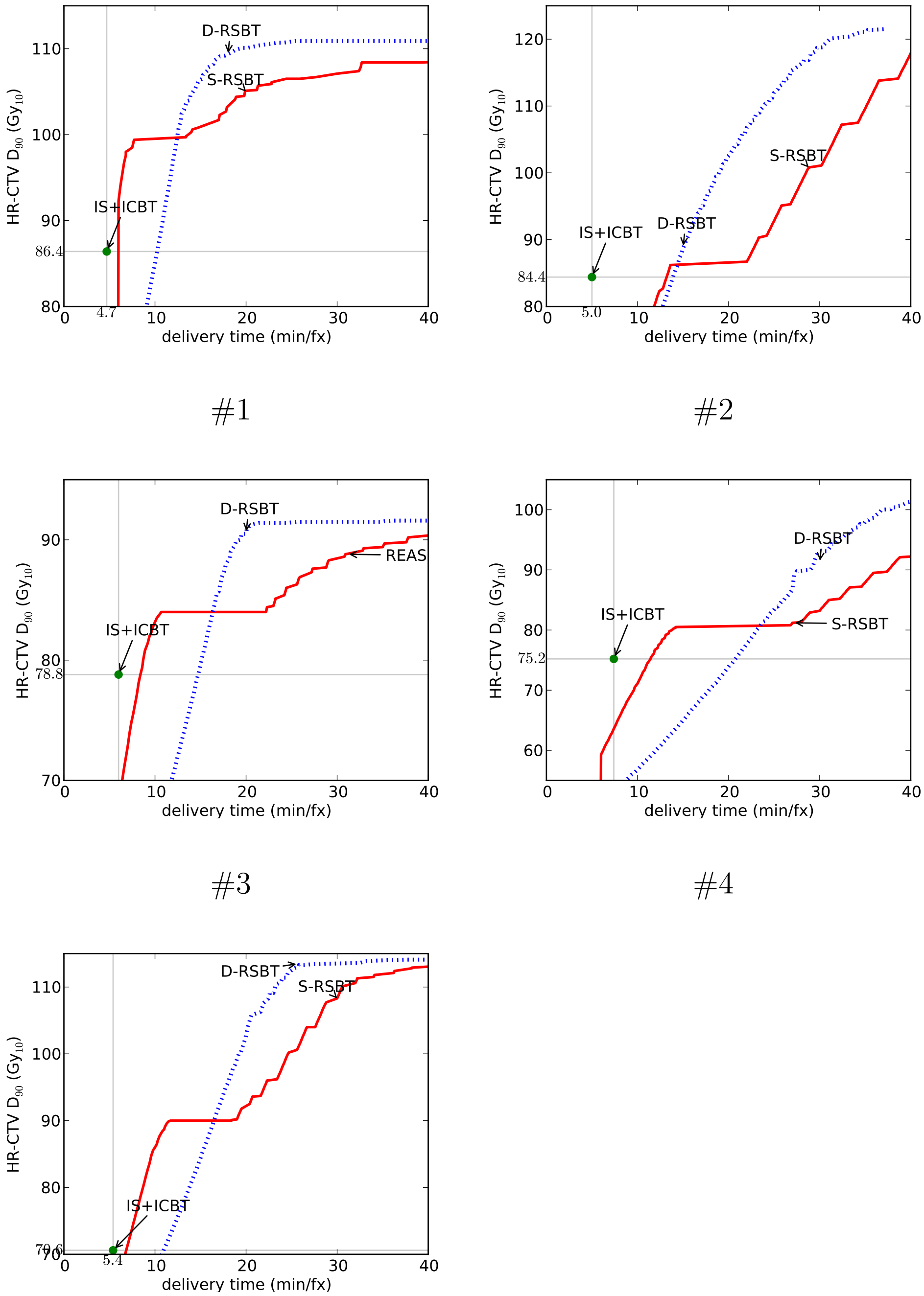

#1

#2

#3

#4

#5

Figure 4.7: Delivery efficiency curves for five clinical cases by using D-RSBT and S-RSBT with REAS. IS+ ICBT plans are also marked on the plot with help lines to indicate the corresponding HR-CTV D$_{90}$ and delivery times.

Table 4.2: Dosimetric comparison for case #1 between S-RSBT and D-RSBT.

Time budget (min/fx)		HR-CTV D_{90} (Gy)	Bladder D_{2cc} (Gy)	Sigmoid D_{2cc} (Gy)	Rectum D_{2cc} (Gy)	Delivery Time	$\Delta\varphi$
10	S-RSBT	99.4	89.7	66.6	75	7.7	245°
	D-RSBT	65.1	79.1	51.8	65.1	10.0	
15	S-RSBT	100.8	88.9	67.5	75	14.7	130°
	D-RSBT	74.2	89.4	56.4	69.4	15	
20	S-RSBT	105.1	84.6	64.3	75	19.9	100°
	D-RSBT	84.3	89.1	59.2	68	20	
25	S-RSBT	106.5	84.6	63.3	75	24.4	85°
	D-RSBT	97.6	88.8	61.4	72.1	25	
30	S-RSBT	107.1	85.5	62.7	75	30	70°
	D-RSBT	104.9	89.3	61.1	75	29.7	

Table 4.3: Dosimetric comparison for case #2 between S-RSBT and D-RSBT.

Time budget (min/fx)		HR-CTV D_{90} (Gy)	Bladder D_{2cc} (Gy)	Sigmoid D_{2cc} (Gy)	Rectum D_{2cc} (Gy)	Delivery Time	$\Delta\varphi$
10	S-RSBT	74.7	88.7	61.4	57.4	10	205°
	D-RSBT	69.7	64.3	61.3	51.3	10.0	
15	S-RSBT	86.2	90	73.6	64.7	13.6	190°
	D-RSBT	87.7	78.3	74.6	56.5	15	
20	S-RSBT	86.2	90	73.6	64.7	13.6	190°
	D-RSBT	101.3	77.6	75	56.1	19.8	
25	S-RSBT	92.8	74	73.4	53	25	105°
	D-RSBT	111	79.3	75	57.5	25.0	
30	S-RSBT	100.8	77.6	75	54.5	28.8	100°
	D-RSBT	117.8	83	75	59.5	29.7	

Table 4.4: Dosimetric comparison for case #3 between S-RSBT and D-RSBT.

Time budget (min/fx)		HR-CTV D_{90} (Gy)	Bladder D_{2cc} (Gy)	Sigmoid D_{2cc} (Gy)	Rectum D_{2cc} (Gy)	Delivery Time	$\Delta\varphi$
10	S-RSBT	83	90	60.7	73.8	9.9	265°
	D-RSBT	64.6	61.7	52.8	57.9	10.0	
15	S-RSBT	84	90	61.7	74.9	10.7	250°
	D-RSBT	78.8	77.9	60.4	70.4	15	
20	S-RSBT	84	90	61.7	74.9	10.7	250°
	D-RSBT	90.1	85.3	62	74.7	20	
25	S-RSBT	86	86.8	61.1	75	24.4	110°
	D-RSBT	91.4	86.1	62.2	75	24.4	
30	S-RSBT	88.3	86	61.2	75	29.1	95°
	D-RSBT	91.5	86.1	62.2	75	29.8	

Table 4.5: Dosimetric comparison for case #4 between S-RSBT and D-RSBT.

Time budget (min/fx)		HR-CTV D_{90} (Gy)	Bladder D_{2cc} (Gy)	Sigmoid D_{2cc} (Gy)	Rectum D_{2cc} (Gy)	Delivery Time	$\Delta\varphi$
10	S-RSBT	71.1	88.8	63.6	57.8	10	285°
	D-RSBT	56.3	65.4	51.2	47.8	10.0	
15	S-RSBT	80.5	90	74	66.5	14.2	235°
	D-RSBT	64.1	85.3	57.4	51	15	
20	S-RSBT	80.5	90	74	66.5	14.2	235°
	D-RSBT	72.7	88.7	66.8	57	20	
25	S-RSBT	80.5	90	74	66.5	14.2	235°
	D-RSBT	82.4	89.4	74.3	62.5	25	
30	S-RSBT	83.2	87.6	66.2	60.6	30	120°
	D-RSBT	90.8	88.5	75	65.6	29.9	

Table 4.6: Dosimetric comparison for case #5 between S-RSBT and D-RSBT.

Time budget (min/fx)		HR-CTV D_{90} (Gy)	Bladder D_{2cc} (Gy)	Sigmoid D_{2cc} (Gy)	Rectum D_{2cc} (Gy)	Delivery Time	$\Delta\varphi$
10	S-RSBT	86	84	74.7	60.6	10	265°
	D-RSBT	66.7	60.5	57	50.8	10	
15	S-RSBT	90	79.8	75	63.4	11.7	230°
	D-RSBT	82.6	75.5	68.6	56.6	15	
20	S-RSBT	91.8	84.4	75	60	19.5	135°
	D-RSBT	100.2	86.6	75	61.6	19.9	
25	S-RSBT	100.2	85.6	75	62	24.7	120°
	D-RSBT	111.4	89.1	75	63.4	24.6	
30	S-RSBT	108.3	88.1	74	64.8	30	105°
	D-RSBT	113.5	89.2	75	63.3	29.5	

4.5 Discussion

Both the visual and quantitative comparison confirms that D-RSBT is a superior delivery method relative to the S-RSBT and IS+ICBT technique, provided that there is sufficient delivery time. Trading a longer delivery time for a higher dose-quality may be desirable, depending on the clinical goal. For example, a previous study by Dimopoulos *et al.* [12] showed that treatment plans with a HR-CTV D_{90} less than 87 Gy may result in poor treatment outcomes, especially when treating large tumors. Based on the five cases studied in this work, the average D_{90} achieved by IS+ICBT is 79 Gy and the average delivery time required is 5.7 min/fx. Note that we cannot increase the D_{90} to 87 Gy by increasing the delivery time in IS+ICBT as at least one of the OARs has already reached the dose limit. If no additional delivery time is allowed, then IS+ICBT is a better choice than both S-RSBT and D-RSBT.

Table 4.7: Average D_{90} comparison between S-RSBT and D-RSBT on different delivery time ranges with 5 clinical cases.

Time range		#1	#2	#3	#4	#5	Avg
10–15	S-RSBT	99.7	81.8	83.9	77.1	89.3	86.4
	D-RSBT	70.4	78.6	71.4	60.1	74.4	71.0
15–20	S-RSBT	102.4	86.2	84.0	80.5	90.3	88.7
	D-RSBT	79.4	94.9	85.5	68.4	91.6	84.0
20–25	S-RSBT	105.8	88.5	84.6	80.5	95.7	91.0
	D-RSBT	90.8	106.4	91.2	77.5	106.5	94.5
25–30	S-RSBT	106.6	97.4	87.3	81.5	104.5	95.5
	D-RSBT	102.0	114.5	91.5	86.6	113.1	101.5
10–30	S-RSBT	103.6	88.5	85.0	79.9	95.0	90.4
	D-RSBT	85.7	98.6	84.8	73.2	96.3	87.7

[1] The time ranges are measured with minutes per fraction (min/fx) and the D_{90} are measured with Gy(EQD2).

[2] The averages over delivery time were computed with 0.2 min/fx spacing.

However, if 15 min/fx (which is about 10 min/fx additional compared to IS+ICBT) delivery time is allowed, then S-RSBT may be the best method as it can boost the average D_{90} to 88.3 Gy. D-RSBT can achieve 81.3 Gy on average within the same delivery time frame. If 25 min/fx is allowed, then D-RSBT can achieve the highest average D_{90} of 98.8 Gy. For S-RSBT, the average D_{90} is 93.2 Gy.

The reason that S-RSBT and D-RSBT tend to achieve better D_{90} with longer delivery time is due to the use of the optimal sequencing algorithms. The optimal sequencing algorithms compute the "best" way to approximate the dose distribution of anchor plans with the constraint of delivery time. The anchor plans are obtained using very fine emission angles, yielding high theoretical D_{90} values. However, the delivery of an anchor plan in clinical practice is not realistic due to the prohibited long delivery time. That is the reason why we need to introduce the sequencing algorithm to compute the "best" approximated plan to the anchor plan for a given clinically reasonable delivery time. The compromise between plan quality and delivery time mainly depends on the emission angles that the RSBT technique can use. As the delivery time increases, the quality of the approximated plan tends to be increasing, since RSBT can use more small emission angles for delivery.

There are several possible ways to improve the D-RSBT technique.

1. Use a more sophisticated D-RSBT applicator design. For example, with the same set of 5 clinical cases and the same anchor plans, if three layers of shielding could be used, the azimuthal emission angle range can be extended from 0°–240°, higher D_{90} at the same delivery time can be expected. [38] But, on the

other hand, it complicates the structure of the applicator and increases the applicator size.

2. Generate anchor plans with a higher quality. Higher quality refers to a higher D_{90} with a smoother dwell time sequence in this application. This claim has already been verified in chapter 2.
3. Design properly weighted objective function for the optimal sequencing algorithm. In this work, we include in the optimization objective a weighted error function to incorporate the dose-volume information for the sequencing problem. The experiments showed that it outperformed the unweighted version with respect to the quality of the computed plans. Our experiments also showed that by using the weighted objective function the quality of the anchor plan was able to be well preserved for reduced delivery time even with less demanding smoothness of the dwell time sequences. However, we noticed that only incorporating the dose-volume information was not adequate. A more sophisticated design of the weighting function may be necessary.

4.6 Conclusion

Patients who need to be treated with HDR-BT may benefit from the D-RSBT technique. Compared to the existing interstitial brachytherapy methods, D-RSBT generate less invasive plans with better dose distributions at the expense of longer delivery times. D-RSBT is also likely to yield better plans in cases where S-RSBT has difficulty in striking a balance between dose quality and delivery time.

CHAPTER 5
PADDLE ROTATING-SHIELD BRACHYTHERAPY

5.1 Introduction

In this chapter, paddle rotating-shield brachytherapy (P-RSBT) is considered as another non-invasive, conformal brachytherapy technique for bulky tumor treatment. Simply speaking, P-RSBT uses a set of independently operated shield paddles, each of which covers a sector of radiation field, to achieve intensity modulation. Specifically, the modulation comes from the insertion/retraction of the shield paddles, as well as the rotation and translation of the whole applicator (Figure 1.4). It is expected that the P-RSBT can combine the advantages from S-RSBT and D-RSBT, thus performs better than both S-RSBT and D-RSBT in the sense of balancing the treatment time and dose quality. A conceptual prototype with shield-paddles for IMBT was proposed in 2010, [53] however, no subsequent study was performed with it to reveal its details and demonstrate its potential in clinical practice. Dynamic modulated brachytherapy (DMBT) might be considered as another IMBT method that utilize shield paddles for intensity modulation. [69, 67, 66] Unlike the P-RSBT model, which is going to be studied in this thesis, the DMBT uses single paddle instead of the barrel-like design for P-RSBT. Therefore, the DMBT applicator behaves much like S-RSBT with 45° azimuthal emission angle. Conversely, there are some similarities between the groove-shielding (GS) applicator design and P-RSBT in the sense of producing radially discontinuous high-dose-regions, despite no paddle is used in GS. [68] However, the GS applicators are static in nature. This makes them easier to implement but limits the capacity to delivery conformal dose distributions. Moreover, the current multi-channel design makes it difficult to use the nice beamlet-superpositioning properties to efficiently produce high-quality deliverable plans, as described in S-RSBT [39] and D-RSBT [38, 40].

5.2 Materials and methods

5.2.1 System overview

The P-RSBT system proposed in this work uses tungsten alloy shield paddles. As shown in Figure 1.4, N shield paddles are arranged into a cylindrical tube and each paddle shields a division of $N/360°$. The shields of P-RSBT were assumed capable of rotation inside a curved applicator and each rotation stride is equal to $\delta\varphi = 5°$, which is also called is the micro-azimuth-angle. It is also assumed that the paddle size is $w\delta\varphi$, i.e. an integer multiple of the micro-azimuth-angle. The paddles can be inserted/retracted independently of each other, forming sectorial high-dose-regions which are called beams. Thus, the P-RSBT applicators are capable to azimuthally modulate the dose intensity. The source, the shield material and the thickness of shields of S-RSBT and D-RSBT, as discussed in chapters 3 and 4, are assumed to be same as P-RSBT.

During the P-RSBT delivery, the P-RSBT applicator will travel through a catheter inserted in the tumor via intracavitary catheters. The applicator will be located at several dwell positions along the central path with spacing $\Delta\lambda$. At each dwell position, the paddles are operated to be retracted or inserted independently to form a set of different beams in an optimized fashion, and rotations are applied when necessary. This procedure can be considered as an analogous of the multi-leaf collimation in the IMRT (intensity modulated radiation therapy). [63, 64, 65]

5.2.2 Radiation source model and dose calculation

An beam $\dot{D}_{i,j}(p)$ in P-RSBT, is defined as the dose rate at the point $\vec{r}_i$ due to a paddle arrangement with source at dwell position $\vec{s}_j (j = 0, \ldots, J-1)$. The arrangement of the paddles can be represented by a binary string p of length $K = 360°/\delta\varphi$, with 0 representing the corresponding sector of size $\delta\varphi$ being shielded by some paddle, and 1 otherwise. Beams can be obtained by multiplying unshielded 3-D dose rate distributions obtained using the TG-43 dose calculation model of Rivard *et al.* (2006) [48] by a binary function that was zero at all points blocked by the shield and unity at all other points.

Considering the different combinations of retracted or inserted paddles with rotations, for each dwell position, the number of different beams can be formed by a P-RSBT applicator is $w2^{K/w}$. As optimizing a deliverable plan directly with paddle arrangements that is exponential of K is impractical, the two-stage inverse planning framework with anchor plans is adopted from the previous RSBT studies. [38, 39, 40] The first step in the two-stage inverse planning is the anchor plan optimization. An anchor plan is an optimized deliverable plan based on an abstract delivery model as described in chapter 2. In the abstract delivery model, the radiation source is placed sequentially along the central path of the applicator which is the same as the P-RSBT delivery. The difference is that, the shield holding the radiation source has only one emission window with fixed azimuthal and zenith emission angles. And the azimuthal emission angle is equal with the micro-azimuth-angle $\delta\varphi$. The beams in the abstract model are called beamlets. As each rotating stride is also equal with $\delta\varphi$, there is no overlapping between the adjacent beamlets at the same dwell position. Mathematically speaking, a beamlet is a beam $\dot{D}_{i,j}(p)$ with p that contains exactly a single 1 bit. Obviously, anchor plans cannot be directly delivered by a P-RSBT apparatus unless $w = 1$.

5.2.3 Generating deliverable plans

The P-RSBT optimal sequencing model was established by the following observation: any P-RSBT deliverable plans can be dosimetric-equivalently substituted by an S-RSBT deliverable plan with azimuthal emission angle equivalent to the paddle size $w\delta\varphi$, yet with shorter delivery time. The optimal sequencing model is shown in Equation (5.1).

$$\min \sum_{j=0}^{J-1} \sum_{k=0}^{K-1} \left(\lambda^{-}_{j,k} H(\tau_{j,k} - t_{j,k}) + \lambda^{+}_{j,k} H(t_{j,k} - \tau_{j,k})\right) (t_{j,k} - \tau_{j,k})^2$$

$$\text{subject to } t_{j,k} = \sum_{p=0}^{w-1} x_{j,(k-p)\%K}, \quad \forall j \in [0, J-1], k \in [0, K-1] \tag{5.1a}$$

$$x_{j,k} \geq 0, \quad \forall j \in [0, J-1], k \in [0, K-1] \tag{5.1b}$$

$$\sum_{j=0}^{J-1} \sum_{q=0}^{w-1} \max_{p=0}^{\frac{k}{w}-1} x_{j,pw+q} \leq T_{max} \tag{5.1c}$$

where $t_{j,k}$ is called the equivalent dwell time for beamlet $\dot{D}_{i,j}(\underbrace{0\ldots0}_{k-1}1\underbrace{0\ldots0}_{K-k})$ in the P-RSBT deliverable plan, and $x_{j,k}$ is the time for a paddle that shields from $k\delta\varphi$ to $(k+w)\delta\varphi$ being retracted at dwell position $\vec{s}_j$. The aim of the optimal sequencing is to minimize the weighted sum of square errors between the fluence maps (i.e. the matrix of dwell times) in the anchor plan and the deliverable plan for all beamlets. $H(x)$ is a Heaviside function introduced for considering the difference between overdosing and underdosing. And $\lambda^{+}_{j,k}, \lambda^{-}_{j,k}$ are the corresponding coefficients for overdosing and underdosing penalties. Equation (5.1a) describes the way of calculating the equivalent dwell time for beamlets from a deliverable plan which is the same as the method described in S-RSBT, [39] and Equation (5.1b) is a constraint to exclude negative dwell times. The difference between P-RSBT and S-RSBT is the calculation of delivery time in Equation (5.1c). Instead of summing $x_{j,k}$ over all j and k, the P-RSBT arranges all compatible, i.e. can be delivered simultaneously, w-beams together to reduce the delivery time.

Equation (5.1) was formulated to a quadratic programming problem and solved by an in-house CPLEX-based optimizer. [10]

5.2.4 Experiment design

The performance of P-RSBT, S-RSBT and D-RSBT were evaluated by the quality of the deliverable plans, and the quality of deliverable plans were illustrated by delivery efficiency curves. [39, 38]

For each of the five clinical cases, a fluence map with $\delta\varphi = 5°$ was generated with an ADOT optimizer. And the same fluence maps were used for all the delivery method studied in this work.

Two sets of comparison experiments were designed.

In the first set of experiments, P-RSBT delivery with different paddles sizes were simulated to study the impact of the paddle sizes on the quality of deliverable plans. The paddle sizes tested varied from 5° to 120°. To distinguish between P-RSBT with different paddle sizes, we denote the P-RSBT delivery with paddle size of $X°$ as P-RSBTX.

In the second set of experiments, S-RSBT and D-RSBT were simulated. S-RSBT uses beams with a fixed azimuthal emission angle during the whole delivery process, while the emission angles of the beams used in D-RSBT can be varying. S-RSBT strives to find an azimuthal emission angle that achieves the best quality of the output deliverable plan. D-RSBT, in fact, finds the best combination of various azimuthal emission angles to deliver the anchor plan aiming to best approximate it. The maximum emission angle that can be used with D-RSBT in our experiment is 180°.

5.3 Results

As shown by the delivery efficiency curves in Figure 5.1, in all five cases tested, the P-RSBT technique is relatively insensitive to the paddle size within a certain range ($\leq 90°$), and it could achieve higher D_{90} than both S-RSBT and D-RSBT, especially with the time range 10-20 min/fx.

For the paddle sizes verified in this chapter, the impact of the paddle size change was marginal for paddle sizes less than 90°. Take delivery time 15 min/fx as an example, while the D_{90} tends to decrease as the paddle size increases, the average drop on D_{90} for P-RSBT30 (the number stands for the shield paddle size, measured in degree) compared to P-RSBT5 is 0.08 Gy. Further increasing on the paddle size resulted in a 0.64 Gy decrease for P-RSBT60 compared to P-RSBT5. The decrease can be magnified to 2.52 Gy with P-RSBT90. However, if the paddle size is increase to 120°, the decrease will be $\sim$ 12 Gy. The detailed quantitative comparison is shown in Table 5.1.

The quantitative comparison between P-RSBT and S-RSBT/D-RSBT can be also read from Table 5.1. Assume the paddle size of P-RSBT is 60° (i.e. P-RSBT60), compared to S-RSBT, the average D_{90} increases on 5 cases were 2.2, 8.3, 12.6, 11.9 and 9.1Gy with delivery time 10, 15, 20, 25 and 30 min/fx. The increases compared to D-RSBT were 16.6, 12.9, 7.2, 3.7 and 1.7 Gy, respectively. For P-RSBT90, the average D_{90} increases on 5 cases compared to S-RSBT were 2.0, 7.7, 10.8, 8.8 and 4.9 Gy with delivery time 10, 15, 20, 25 and 30 min/fx. The increases compared to D-RSBT were 16.4, 12.3, 5.5, 0.6 and -2.5 Gy, respectively.

Take case #3 with delivery time 15 min/fx as an example, the dose distributions comparison for P-RSBT with paddle sizes 5°, 60°, 90° and 120° are shown in Figure 5.2, and the DVHs are shown in Figure 5.3. It can be observed in the dose distribution plots in Figure 5.2 that, the isodose contours become less conformal to the HR-CTV boundary as the paddle size increases. However, the changes are

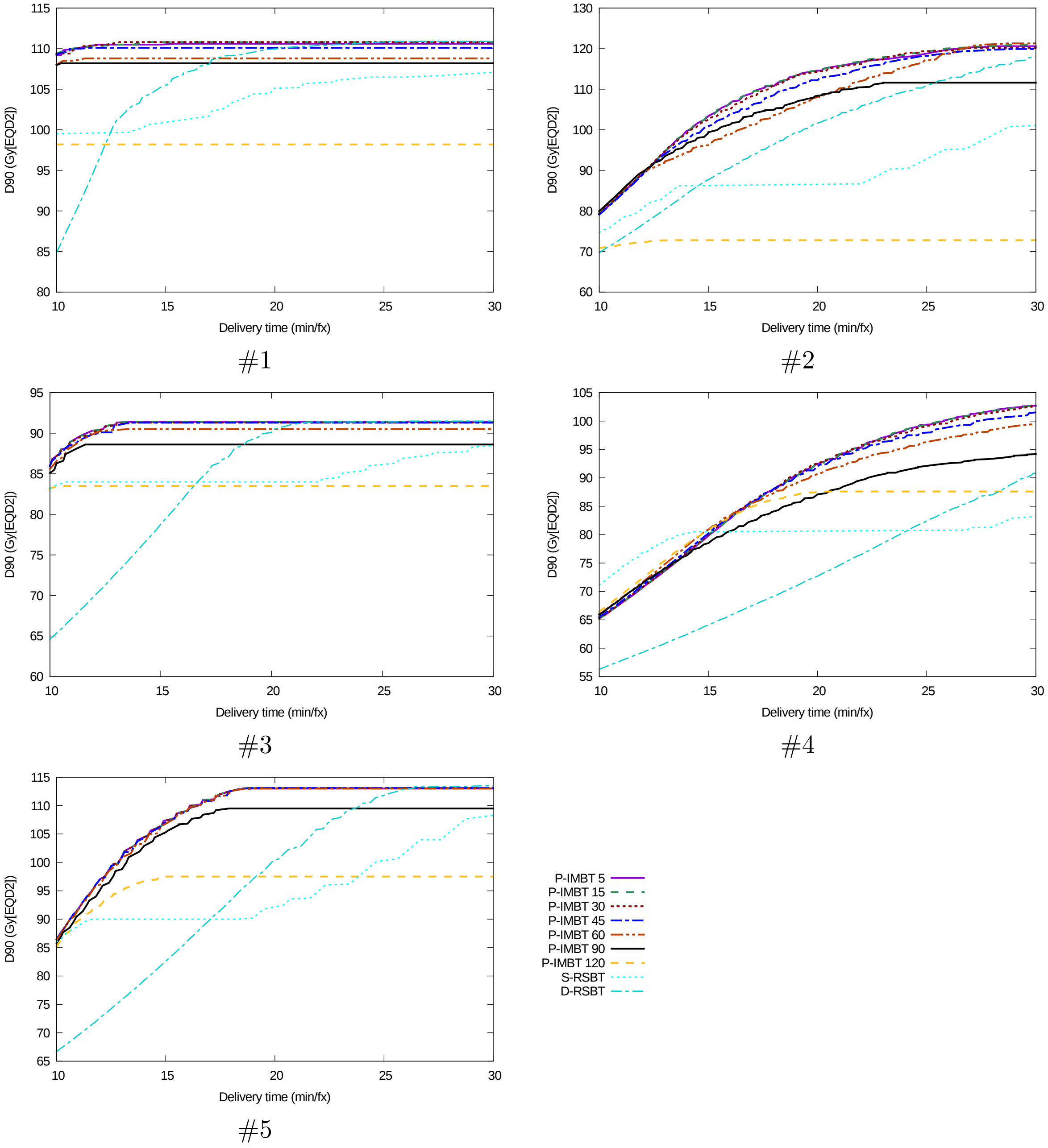

#1

#2

#3

#4

#5

Figure 5.1: Delivery efficiency curves comparison between P-RSBT with different paddle sizes, S-RSBT and D-RSBT on 5 different clinical cases. A point on a delivery efficiency curve stands for the maximal D_{90} (y-axis) can be achieved with the corresponding delivery method with given delivery time (x-axis).

Table 5.1: D_{90} (Gy_{10}) comparison between P-RSBT with different paddle sizes, S-RSBT and D-RSBT on 5 different clinical cases under different delivery time limits.

Case	Time (min/fx)	P-RSBT							S-RSBT	D-RSBT
		5°	15°	30°	45°	60°	90°	120°		
#1	10	109	109	109	109	108	108	98	99	85
	15	111	111	111	110	109	108	98	101	105
	20	111	111	111	110	109	108	98	105	110
	25	111	111	111	110	109	108	98	107	111
	30	111	111	111	110	109	108	98	107	111
#2	10	79	79	79	79	80	80	71	75	70
	15	103	103	103	101	96	99	73	86	88
	20	115	114	114	112	108	108	73	86	101
	25	119	119	119	118	117	112	73	93	111
	30	121	121	120	120	121	112	73	101	118
#3	10	86	86	86	86	85	85	83	83	65
	15	91	91	91	91	91	89	84	84	79
	20	91	91	91	91	91	89	84	84	90
	25	91	91	91	91	91	89	84	86	91
	30	91	91	91	91	91	89	84	88	92
#4	10	65	65	65	66	66	66	67	71	56
	15	80	80	80	80	81	79	81	81	64
	20	92	92	92	92	90	87	87	81	73
	25	99	99	99	98	96	92	88	81	82
	30	103	103	103	101	100	94	88	83	91
#5	10	87	87	87	87	86	86	85	86	67
	15	107	107	107	107	107	105	98	90	83
	20	113	113	113	113	113	110	98	92	100
	25	113	113	113	113	113	110	98	100	111
	30	113	113	113	113	113	110	98	108	114
Avg	10	85	85	85	85	85	85	81	83	68
	15	98	99	98	98	97	96	87	88	84
	20	104	104	104	104	102	100	88	90	95
	25	107	107	107	106	105	102	88	93	101
	30	108	108	108	107	107	102	88	98	105

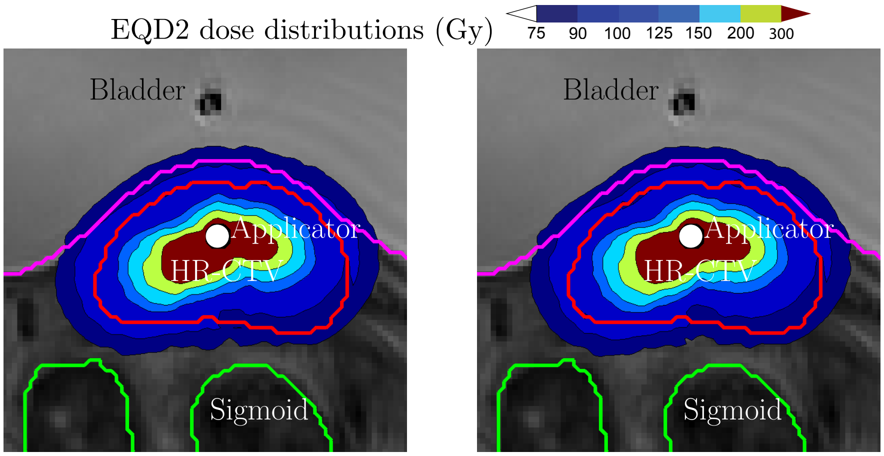

(a) P-IMBT5 D_{90} = 91.4 Gy (b) P-IMBT60 D_{90} = 90.5 Gy

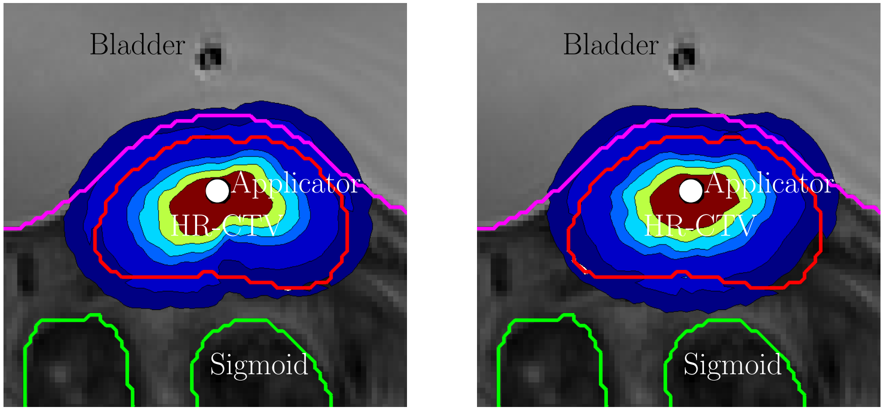

(c) P-IMBT90 D_{90} = 88.6 Gy (d) P-IMBT120 D_{90} = 83.5 Gy

Figure 5.2: EQD2 dose distributions for case #3 with delivery time 15 min/fx for P-RSBT with paddle sizes of 5°, 60°, 90° and 120°.

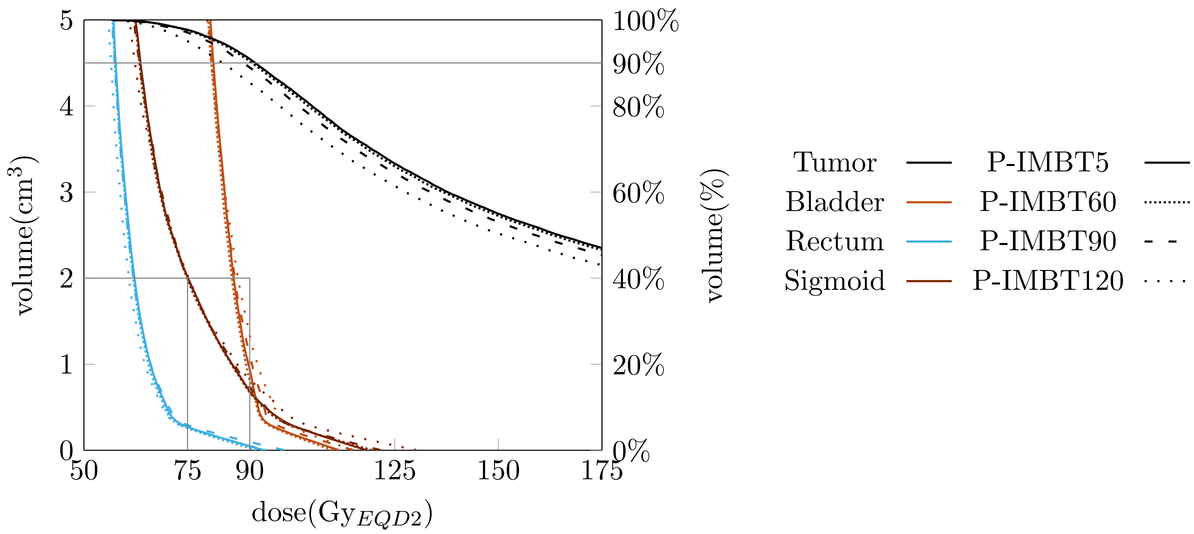

Figure 5.3: DVH plots for case #3 with delivery time 15 min/fx for P-RSBT with paddle sizes of 5°, 60°, 90° and 120°.

marginal. According to Figure 5.3, while the DVH curves for OARs remains about the same, the separation between the DVH curves for HR-CTV are not significant as well. The D_{90} of these four different P-RSBT deliveries are 91.4, 90.5, 88.6 and 83.5 Gy, correspondingly.

Using the same case #3 as the example, the differences of dose distributions (Figure 5.4) and the DVHs (Figure 5.5) are easier to perceive in the comparison between S-RSBT, D-RSBT, P-RSBT60 and P-RSBT90. The D_{90} are 84.0, 78.8, 88.6 and 83.5 Gy, correspondingly.

5.4 Discussion

Compared to the previously proposed techniques, P-RSBT performs better than S-RSBT since the dose distribution produced by P-RSBT can be regards as a

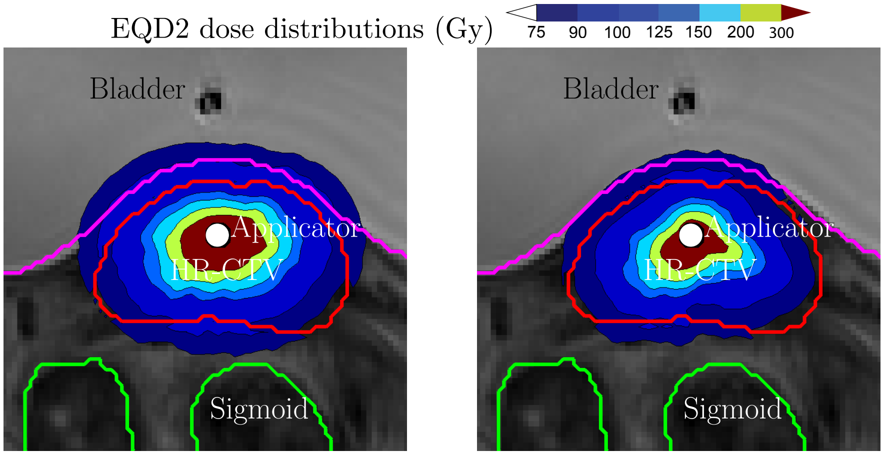

(a) S-RSBT D_{90} = 84.0 Gy (b) D-RSBT D_{90} = 78.8 Gy

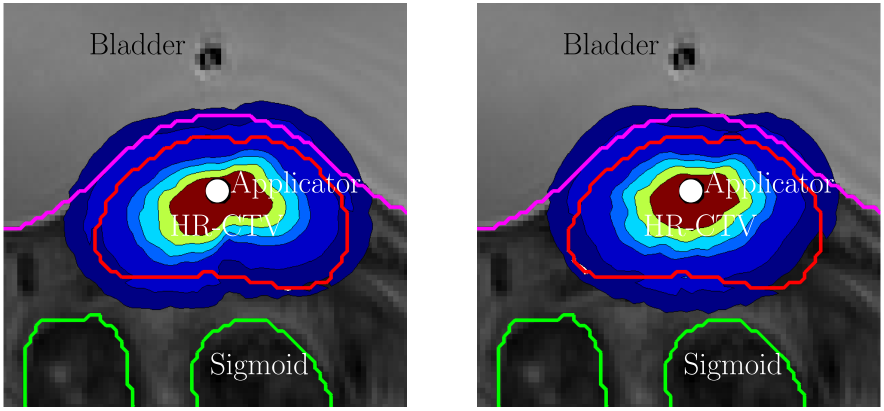

(c) P-IMBT90 D_{90} = 88.6 Gy (d) P-IMBT120 D_{90} = 83.5 Gy

Figure 5.4: EQD2 dose distributions for case #3 with delivery time 15 min/fx for S-RSBT, D-RSBT, P-RSBT with paddle sizes of 90° and 120°.

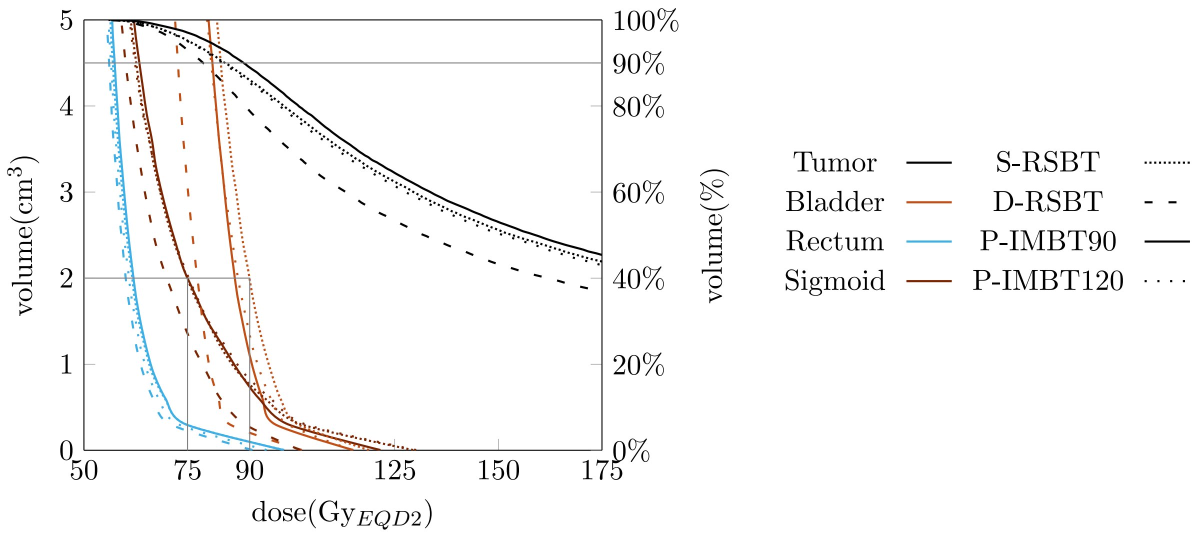

Figure 5.5: DVH plots for case #3 with delivery time 15 min/fx for S-RSBT, D-RSBT, P-RSBT with paddle sizes of 90° and 120°.

distribution produced by an S-RSBT with a small azimuthal emission angle (equal to the paddle size) yet with much less delivery time. According to the previous study on S-RSBT, [39] the dose distribution quality tends to increase as the azimuthal emission angle decreases, however, the delivery time tends to increase. On the contrary, P-RSBT delivery does not suffer from the delivery time increase that much as the paddle size decreases given that the paddle size less than 90°. The reason for this difference hinges on the models of optimal sequencing in these two delivery models. While the S-RSBT can only combine a fixed number of neighboring beamlets to form a beam, the P-RSBT can use different numbers of beamlets to form a beam, and these beamlets do not have to be adjacent to each other. Therefore, compared to S-RSBT with small azimuthal emission angles, the P-RSBT is superior as it can form beams with larger coverage without scarifying the dose quality much; and compared to S-RSBT with large azimuthal emission angles, P-RSBT is superior as it can form beams with fine-tuned coverage when necessary.

P-RSBT also performs better than D-RSBT mainly because it is able to form beams with larger coverage. It does not have significant advantage over D-RSBT in forming beams with fine-tuned coverage, thus it is not much better than D-RSBT with sufficiently large delivery time (∼30min/fx). With 30 min/fx delivery time, the P-RSBT achieved less than 3 Gy more than D-RSBT on average. Roughly speaking, for these three techniques studied in this work or other delivery technique under the beamlets-superposition equivalence assumption, the ability of forming small beams helps on improving the dose distribution quality; and the ability of forming large beams helps on reducing the delivery time. While it is relatively easier to achieve large beams in S-RSBT and easier to achieve small beams in D-RSBT, P-RSBT technique proposed a possible way to combine these two powers together. Yet, at the price of more complex apparatus designs. While reducing the paddle size theoretically improves the performance of P-RSBT, it increases the number of paddles to form a P-RSBT applicator. Both the increase in the number of paddles and the decrease on the paddle size complicate the manufacturing of the P-RSBT applicator. Thus, it is preferred to keep the size of the paddles reasonably large. According to the result shown in this chapter, it is predicted that four paddles with 90° might be a good tradeoff between the delivery quality and the manufacturing complexity.

5.5 Conclusion

P-RSBT can be considered as one of the most promising intensity modulation technique for brachytherapy, in the sense of balancing the treatment time and the dose quality. Using the techniques introduced in this study, the P-RSBT can keep the loss of plan quality in reduced treatment time, measured by the HR-CTV D_{90}, at a low level. Compared to the existing S-RSBT and D-RSBT technique, P-RSBT can boost the HR-CTV D_{90} by 7.7 and 12.3 Gy on average with delivery time 15 min/fx for S-RSBT and D-RSBT using 90° paddles .

CHAPTER 6
CONCLUSION AND FUTURE WORK

In this chapter, we conclude the thesis and discuss some of the possible directions in which we may used to extend our current research.

6.1 Summary of research results

In this thesis, we studied a series of problems that arise in rotating-shield brachytherapy (RSBT). More specifically, we modeled and solved the problems for anchor plan optimization, optimal sequencing for single rotating-shield brachytherapy (S-RSBT), dynamic rotating-shield brachytherapy (D-RSBT) and paddle rotating-shield brachytherapy (P-RSBT). We implemented all the algorithm proposed in this work and experimented them with real medical data. The following is a summary of our research result.

6.1.1 Anchor plan optimization

We demonstrated that the "smoothness" of the fluence map (quantified by total-variations) is important factor for improving the quality of anchor plans. By incorporating the total-variation into the dose optimization for anchor plans, we proposed a novel model named *asymmetric dose-volume optimization with total-variation control*(ADOT). The ADOT model features with asymmetric cost functions for overdosing and underdosing, position-aware cost functions and weighted total-variation control. As the model is convex, it can be solved efficiently with less than 3 minutes for all the cases studied. Experiments show that the ADOT achieves comparable dose quality in anchor plans compared to time-consuming inverse-planning by simulated-annealing (IPSA), and achieves ∼10 Gy higher D_{90} for deliverable plans in S-RSBT and D-RSBT in the time range of interest (10–30 min/fx).

6.1.2 Single rotating-shield brachytherapy

By using the rapid emission angle selection (REAS) algorithm, the dose optimization step, including the anchor plan optimization and the optimal sequencing, can be finished within 10 minutes. Compared exhaustive replanning with volume optimization (ERVO), which theoretically generates the best results, REAS achieves slighter better result when there is a 3-minutes limited on each call to the dose-volume optimizer. However, the speed of REAS is about 30 times faster than ERVO. Compared to another exhaustive planning method: exhaustive replanning with surface optimization (ERSO), REAS still has its speed advantage. It runs 2 times faster than ERSO. Moreover, it provides ∼10% D_{90} boost compared to ERSO.

6.1.3 Dynamic rotating-shield brachytherapy

We proposed a combinatorial approach named as CIBD to solve the optimal sequencing problem. We proved that the CIBD algorithm can solve the optimal sequencing problem efficiently theoretically to the global optimum and the complexity is proved to be $\mathcal{O}(n^2 \log n \log(nH))$. Experiment shows the algorithm runs efficiently with both phantom and clinical cases as well. Although the CIBD algorithm has a shortcoming in solving D-RSBT optimal sequencing problem with multiple dwell positions, the study in CIBD still paves the way for us to model the D-RSBT optimal sequencing with multiple dwell positions. We proposed a numerical optimization method to solve the case when multiple dwell positions is involved. The experiments showed that D-RSBT has its advantage over S-RSBT, when the delivery time is relatively sufficient for its delivery, i.e. 20–30 min/fx. This is caused by the maximal azimuthal emission angle used by D-RSBT. While using larger azimuthal emission angle helps reducing the delivery time, an maximal angle constraint makes D-RSBT become inferior with limited delivery times.

6.1.4 Paddle intensity-modulated brachytherapy

We showed that the optimal sequencing problem for P-RSBT is similar to the one used in S-RSBT, albeit with a quite different way of computing the delivery times. The experiments validated our prediction, the P-RSBT outperforms S-RSBT and D-RSBT in most of the cases. We also showed that, P-RSBT is relatively insensitive to the size of the paddles with paddle sizes $\leq 90°$. And this is a good news for potential P-RSBT applications, as that means, P-RSBT with about 4–6 paddle might be enough for the real clinical applications.

6.2 Future works

The successful completion of this project moves the RSBT a big step forward towards its application in the clinic, triggering a new era in brachytherapy delivery, which will have a widespread impact on the whole radiation oncology field. The methods and tools developed in this work will fundamentally shift the current HDR-BT treatment paradigm for many cancer sites, including cervical cancers, rectal cancers and prostate cancers. It may be also expected that RSBT will have dramatically lower cost than other treatments such as proton therapy. As an brachytherapy technique, RSBT will be insensitive to patient motion, thus the delivery accuracy will be superior to that of external radiation therapy. All these benefits would contribute the the elimination of death and suffering from cancer, improving quality of life for millions of cancer patients.

To finally make the RSBT available in clinic and to make more cancer patients benefited from the develop of RSBT, the future works may includes:

1. Making smaller applicators. Further reducing the size of applicators may indicate thinner shields. Thinner shields may deny the safe assumption of zero-transmission through the shield. While large transmissions such as 50% cannot be used for RSBT, transmission within a proper range may even help to reduce the delivery time of RSBT with the help of properly designed treatment planning system.
2. Considering multiple channels. While single channel RSBT can help to improve dose conformity, in some cases, multiple channel RSBT might be demanded to further improve the dose conformity or to help to reduce the hot spots that is intrinsic in single channel RSBT. However, with the additional degree of freedoms come from multiple channels, there is a even higher demand on efficient anchor plan optimization technique.
3. Developing new prototypes of RSBT apparatus. Although three different RSBT

delivery prototypes were studied in this thesis, there might be more techniques that can be used to improve the RSBT delivery. Future prototypes of RSBT apparatus may reduce the complexity of manufacturing the real equipments, or may introduce new methods of intensity modulation that can improve the dose distribution with limited delivery time, or can be used in more cancer sites.

REFERENCES

[1] R. K Ahuja, D. S Hochbaum, and J. B Orlin. Solving the convex cost integer dual network flow problem. *Management Science*, 49(7):950964, 2003.

[2] M Alber and F Nüsslin. Intensity modulated photon beams subject to a minimal surface smoothing constraint. *Physics in Medicine and Biology*, 45(5):N49–N52, May 2000.

[3] G. P. Ashkar and J. W. Modestino. The contour extraction problem with biomedical applications. *Computer Graphics and Image Processing*, 7(3):331–355, June 1978.

[4] Stephen R. Bowen, Ryan T. Flynn, Sren M. Bentzen, and Robert Jeraj. On the sensitivity of IMRT dose optimization to the mathematical form of a biological imaging-based prescription function. *Physics in Medicine and Biology*, 54(6):1483, March 2009.

[5] Sheree Brown, Mark McLaughlin, Doyle Keith Pope, Kenneth Haile, Lorie Hughes, Philip Z. Israel, and Maureen Lyden. A dosimetric comparison of the contura multilumen balloon breast brachytherapy catheter vs. the single-lumen MammoSite balloon device in patients treated with accelerated partial breast irradiation at a single institution. *Brachytherapy*, 10(1):68–73, January 2011.

[6] Kevin A. Camphausen and R. C. Lawrence. Principles of radiation therapy. *Cancer Management: A Multidisciplinary Approach*, 11, 2008.

[7] D. Chassagne, A. Dutreix, D. Ash, W. F. Hanson, A. G. Visser, and J. F. Wilson. Dose and volume specification for reporting interstitial therapy. *ICRU Report no58*, 1997.

[8] Danny Chen, Jie Wang, and Xiaodong Wu. Image segmentation with monotonicity and smoothness constraints. In Peter Eades and Tadao Takaoka, editors, *Algorithms and Computation*, volume 2223 of *Lecture Notes in Computer Science*, pages 467–479. Springer Berlin / Heidelberg, 2001.

[9] Robert A. Cormack. Image-guided brachytherapy. In Ferenc A. Jolesz, editor, *Intraoperative Imaging and Image-Guided Therapy*, pages 385–395. Springer New York, January 2014.

[10] IBM ILOG CPLEX. V12. 1: Users manual for CPLEX. *International Business Machines Corporation*, 46(53):157, 2009.

[11] J.C.A. Dimopoulos, S. Lang, C. Kirisits, E.F. Fidarova, D. Berger, P. Georg, W. Dörr, and R. Pötter. DoseVolume histogram parameters and local tumor control in magnetic resonance ImageGuided cervical cancer brachytherapy. *International Journal of Radiation Oncology* Biology* Physics*, 75(1):5663, 2009.

[12] J.C.A. Dimopoulos, R. Pötter, S. Lang, E. Fidarova, P. Georg, W. Dörr, and C. Kirisits. Doseeffect relationship for local control of cervical cancer by magnetic resonance image-guided brachytherapy. *Radiotherapy and oncology*, 93(2):311315, 2009.

[13] Johannes C.A. Dimopoulos, Christian Kirisits, Primoz Petric, Petra Georg, Stefan Lang, Daniel Berger, and Richard Pötter. The vienna applicator for combined intracavitary and interstitial brachytherapy of cervical cancer: Clinical feasibility and preliminary results. *International Journal of Radiation Oncology*Biology*Physics*, 66(1):83–90, September 2006.

[14] AnthonyV. DAmico, Robert Cormack, ClareM. Tempany, Sanjaya Kumar, George Topulos, HanneM. Kooy, and C. Norman Coleman. Real-time magnetic resonance image-guided interstitial brachytherapy in the treatment of select patients with clinically localized prostate cancer. *International Journal of Radiation Oncology*Biology*Physics*, 42(3):507–515, October 1998.

[15] M A Ebert. Possibilities for intensity-modulated brachytherapy: technical limitations on the use of non-isotropic sources. *Physics in Medicine and Biology*, 47(14):2495–2509, July 2002.

[16] M. A. Ebert. Potential dose-conformity advantages with multi-source intensity-modulated brachytherapy (IMBT). *Australasian Physics & Engineering Sciences in Medicine*, 29(2):165–171, June 2006.

[17] R. T. Flynn, D. L. Barbee, T. R. Mackie, and R. Jeraj. Comparison of intensity modulated x-ray therapy and intensity modulated proton therapy for selective subvolume boosting: a phantom study. *Physics in Medicine and Biology*, 52(20):6073, October 2007.

[18] R. T. Flynn, M. W. Kissick, M. P. Mehta, G. H. Olivera, R. Jeraj, and T. R. Mackie. The impact of linac output variations on dose distributions in helical tomotherapy. *Physics in Medicine and Biology*, 53(2):417, January 2008.

[19] Ryan T. Flynn, Stephen R. Bowen, Sren M. Bentzen, T. Rockwell Mackie, and Robert Jeraj. Intensity-modulated x-ray (IMXT) versus proton (IMPT) therapy for theragnostic hypoxia-based dose painting. *Physics in Medicine and Biology*, 53(15):4153, August 2008.

[20] J. F Fowler, J. S Welsh, and S. P Howard. Loss of biological effect in prolonged fraction delivery. *International journal of radiation oncology, biology, physics*, 59(1):242249, 2004.

[21] James M. Galvin, Gary Ezzell, Avraham Eisbrauch, Cedric Yu, Brian Butler, Ying Xiao, Isaac Rosen, Julian Rosenman, Michael Sharpe, and Lei Xing. Implementing IMRT in clinical practice: a joint document of the american society for therapeutic radiology and oncology and the american association of physicists in medicine. *International Journal of Radiation Oncology* Biology* Physics*, 58(5):16161634, 2004.

[22] Alain Gerbaulet and Alain Gerbaulet. *The GEC ESTRO handbook of brachytherapy*. Estro Brussels, 2002.

[23] Eli Glatstein, Allen S. Lichter, Benedick A. Fraass, Barbara A. Kelly, and Jan van de Geijn. The imaging revolution and radiation oncology: Use of CT, ultrasound, and nmr for localization, treatment planning and treatment delivery. *International Journal of Radiation Oncology*Biology*Physics*, 11(2):299–314, February 1985.

[24] A V Goldberg and R E Tarjan. A new approach to the maximum flow problem. In *Proceedings of the eighteenth annual ACM symposium on Theory of computing*, STOC '86, page 136146, New York, NY, USA, 1986. ACM.

[25] Christine Haie-Meder, Richard Pötter, Erik Van Limbergen, Edith Briot, Marisol De Brabandere, Johannes Dimopoulos, Isabelle Dumas, Taran Paulsen Hellebust, Christian Kirisits, Stefan Lang, Sabine Muschitz, Juliana Nevinson, An Nulens, Peter Petrow, and Natascha Wachter-Gerstner. Recommendations from gynaecological (GYN) GEC-ESTRO working group (i): concepts and terms in 3D image based 3D treatment planning in cervix cancer brachytherapy with emphasis on MRI assessment of GTV and CTV. *Radiotherapy and Oncology*, 74(3):235–245, March 2005.

[26] G.E. Hanks, D.F. Herring, and S. Kramer. Patterns of care outcome studies results of the national practice in cancer of the cervix. *Cancer*, 51(5):959967, 1983.

[27] Zhihong Hu, Xiaodong Wu, Yanwei Ouyang, Yanling Ouyang, and Srinivas R. Sadda. Semiautomated segmentation of the choroid in spectral-domain optical coherence tomography volume scans. *Investigative Ophthalmology & Visual Science*, 54(3):1722–1729, March 2013. PMID: 23349432.

[28] Dayee Jacob, Adam Raben, Abhirup Sarkar, Jimm Grimm, and Larry Simpson. Anatomy-based inverse planning simulated annealing optimization in high-dose-rate prostate brachytherapy: Significant dosimetric advantage over other optimization techniques. *International Journal of Radiation Oncology*Biology*Physics*, 72(3):820–827, November 2008.

[29] Ina M. Jürgenliemk-Schulz, Robbert J. H. A. Tersteeg, Judith M. Roesink, Stefan Bijmolt, Christel N. Nomden, Marinus A. Moerland, and Astrid A. C. de Leeuw. MRI-guided treatment-planning optimisation in intracavitary or combined intracavitary/interstitial PDR brachytherapy using tandem ovoid applicators in locally advanced cervical cancer. *Radiotherapy and Oncology*, 93(2):322–330, November 2009.

[30] Faiz M. Khan. *The Physics of Radiation Therapy*. Lippincott Williams & Wilkins, May 2009.

[31] Hojin Kim, Tae-Suk Suh, Rena Lee, Lei Xing, and Ruijiang Li. Efficient IMRT inverse planning with a new l1-solver: template for first-order conic solver. *Physics in Medicine and Biology*, 57(13):4139, July 2012.

[32] Taeho Kim, Lei Zhu, Tae-Suk Suh, Sarah Geneser, Bowen Meng, and Lei Xing. Inverse planning for IMRT with nonuniform beam profiles using total-variation regularization (TVR). *Medical Physics*, 38(1):57–66, December 2010.

[33] Christian Kirisits, Stefan Lang, Johannes Dimopoulos, Daniel Berger, Dietmar Georg, and Richard Pötter. The vienna applicator for combined intracavitary and interstitial brachytherapy of cervical cancer: Design, application, treatment planning, and dosimetric results. *International Journal of Radiation Oncology*Biology*Physics*, 65(2):624–630, June 2006.

[34] Vladimir Kolmogorov and Akiyoshi Shioura. New algorithms for convex cost tension problem with application to computer vision. *Discrete Optimization*, 6(4):378–393, November 2009.

[35] Bernard Lachance, Dominic Bliveau-Nadeau, Étienne Lessard, Mario Chrtien, I. Chow Joe Hsu, Jean Pouliot, Luc Beaulieu, and Éric Vigneault. Early clinical experience with anatomy-based inverse planning dose optimization for high-dose-rate boost of the prostate. *International Journal of Radiation Oncology*Biology*Physics*, 54(1):86–100, September 2002.

[36] Liyong Lin, Rakesh R. Patel, Bruce R. Thomadsen, and Douglass L. Henderson. The use of directional interstitial sources to improve dosimetry in breast brachytherapy. *Medical Physics*, 35(1):240–247, December 2007.

[37] Yunlong Liu, Ryan T. Flynn, Yusung Kim, and Xiaodong Wu. Dynamic-shield intensity modulated brachytherapy (IMBT) for cervical cancer. *International Journal of Radiation Oncology* Biology* Physics*, 81(2):S201, 2011.

[38] Yunlong Liu, Ryan T. Flynn, Yusung Kim, Wenjun Yang, and Xiaodong Wu. Dynamic rotating-shield brachytherapy. *Medical Physics*, 40(12):121703, November 2013.

[39] Yunlong Liu, Ryan T. Flynn, Wenjun Yang, Yusung Kim, Sudershan K. Bhatia, Wenqing Sun, and Xiaodong Wu. Rapid emission angle selection for rotating-shield brachytherapy. *Medical Physics*, 40(5):051720, April 2013.

[40] Yunlong Liu and Xiaodong Wu. Solving circular integral block decomposition in polynomial time. In Kun-Mao Chao, Tsan-sheng Hsu, and Der-Tsai Lee, editors, *Algorithms and Computation*, number 7676 in Lecture Notes in Computer Science, pages 342–351. Springer Berlin Heidelberg, January 2012.

[41] Lijun Ma. Smoothing intensity-modulated treatment delivery under hardware constraints. *Medical Physics*, 29(12):2937–2945, December 2002.

[42] Thomas Martin, Dimos Baltas, Ralf Kurek, Sandra Röddiger, Marina Kontova, Georgios Anagnostopoulos, Thomas Dannenberg, Thomas Buhleier, Georgies Skazikis, Ulf Tunn, and Nikolaos Zamboglou. 3-d conformal HDR brachytherapy as monotherapy for localized prostate cancer. *Strahlentherapie und Onkologie*, 180(4):225–232, April 2004.

[43] Gerard C. Morton, Raxa Sankreacha, Patrick Halina, and Andrew Loblaw. A comparison of anatomy-based inverse planning with simulated annealing and graphical optimization for high-dose-rate prostate brachytherapy. *Brachytherapy*, 7(1):12–16, January 2008.

[44] Kazuo Murota. *Discrete Convex Analysis*. SIAM, 2003.

[45] NCI. *SEER cancer incidence public use database (2000-2007)*. National Cancer Institute, Bethesda, MD, 2011.

[46] R. Pötter, J. Dimopoulos, P. Georg, S. Lang, C. Waldhäusl, N. Wachter-Gerstner, H. Weitmann, A. Reinthaller, T.H. Knocke, S. Wachter, et al. Clinical impact of MRI assisted dose volume adaptation and dose escalation in brachytherapy of locally advanced cervix cancer. *Radiotherapy and oncology*, 83(2):148155, 2007.

[47] Richard Pötter, Christine Haie-Meder, Erik Van Limbergen, Isabelle Barillot, Marisol De Brabandere, Johannes Dimopoulos, Isabelle Dumas, Beth Erickson, Stefan Lang, An Nulens, Peter Petrow, Jason Rownd, and Christian Kirisits. Recommendations from gynaecological (GYN) GEC ESTRO working group (II): concepts and terms in 3D image-based treatment planning in cervix cancer brachytherapy3D dose volume parameters and aspects of 3D image-based anatomy, radiation physics, radiobiology. *Radiotherapy and Oncology*, 78(1):67–77, January 2006.

[48] Mark J. Rivard, Stephen D. Davis, Larry A. DeWerd, Thomas W. Rusch, and Steve Axelrod. Calculated and measured brachytherapy dosimetry parameters in water for the xoft axxent x-ray source: An electronic brachytherapy sourcea). *Medical Physics*, 33(11):4020–4032, October 2006.

[49] D. W. O. Rogers, B. A. Faddegon, G. X. Ding, C.-M. Ma, J. We, and T. R. Mackie. BEAM: a monte carlo code to simulate radiotherapy treatment units. *Medical physics*, 22(5):503524, 1995.

[50] Francesc Salvat, Jos M. Fernndez-Varea, and Josep Sempau. PENELOPE-2006: a code system for monte carlo simulation of electron and photon transport. In *Workshop Proceedings*, volume 4, page 7, 2006.

[51] Chengyu Shi, Bingqi Guo, Chih-Yao Cheng, Carlos Esquivel, Tony Eng, and Niko Papanikolaou. Three dimensional intensity modulated brachytherapy (IMBT): dosimetry algorithm and inverse treatment planning. *Medical Physics*, 37(7):3725, 2010.

[52] Timmy Siauw, Adam Cunha, Alper Atamtürk, I.-Chow Hsu, Jean Pouliot, and Ken Goldberg. IPIP: a new approach to inverse planning for HDR brachytherapy by directly optimizing dosimetric indices. *Medical Physics*, 38(7):4045–4051, June 2011.

[53] Peter C. Smith, Michael Klein, Heike Hausen, and Paul A. Lovoi. United states patent: 7686755 - radiation therapy apparatus with selective shielding capability, March 2010.

[54] Milan Sonka, Vaclav Hlavac, and Roger Boyle. *Image processing, analysis, and machine vision*, volume 3. Thomson Toronto, 2008.

[55] Edward S. Sternick. *The Theory and Practice of Intensity Modulated Radiation Therapy: Proceedings of the 1st NOMOS IMRT Workshop, Held in Durango, Colorado*. Advanced Medical Publishing, 1997.

[56] A. M. Nisar Syed, Ajmel A Puthawala, Nashwa Nazmy Abdelaziz, Mervat el Naggar, Philip Disaia, Michael Berman, Krishnansu S Tewari, Anil Sharma, Adina Londrc, Supriya Juwadi, Joel M Cherlow, Steven Damore, and Yi-Jen Chen. Long-term results of low-dose-rate interstitial-intracavitary brachytherapy in the treatment of carcinoma of the cervix. *International Journal of Radiation Oncology*Biology*Physics*, 54(1):67–78, September 2002.

[57] K. Tanderup, S.K. Nielsen, G.B. Nyvang, E.M. Pedersen, L. RU00F8hl, T. Aagaard, L. Fokdal, and J.C. Lindegaard. From point a to the sculpted pear: MR image guidance significantly improves tumour dose and sparing of organs at risk in brachytherapy of cervical cancer. *Radiotherapy and Oncology*, 94(2):173180, 2010.

[58] D.R. Thedens, David J. Skorton, and S.R. Fleagle. Methods of graph searching for border detection in image sequences with applications to cardiac magnetic resonance imaging. *IEEE Transactions on Medical Imaging*, 14(1):42–55, March 1995.

[59] Jing Tian, Pina Marziliano, Mani Baskaran, Tin Aung Tun, and Tin Aung. Automatic segmentation of the choroid in enhanced depth imaging optical coherence tomography images. *Biomedical Optics Express*, 4(3):397–411, March 2013.

[60] International Commission on Radiation Units and Measurements. *Dose and Volume Specification for Reporting Intracavitary Therapy in Gynecology; Repr.* International Commission on Radiation Units and Measurements, 1991.

[61] Akila N. Viswanathan, Sushil Beriwal, Jennifer F. De Los Santos, D. Jeffrey Demanes, David Gaffney, Jorgen Hansen, Ellen Jones, Christian Kirisits, Bruce Thomadsen, and Beth Erickson. American brachytherapy society consensus guidelines for locally advanced carcinoma of the cervix. part II: high-dose-rate brachytherapy. *Brachytherapy*, 11(1):47–52, January 2012.

[62] David E. Wazer, Lisa Berle, Roger Graham, Maureen Chung, Janice Rothschild, Theresa Graves, Blake Cady, Kenneth Ulin, Robin Ruthazer, and Thomas A. DiPetrillo. Preliminary results of a phase I/II study of HDR brachytherapy alone for T1/T2 breast cancer. *International Journal of Radiation Oncology*Biology*Physics*, 53(4):889–897, July 2002.

[63] S. Webb. *Intensity-modulated radiation therapy.* Inst of Physics Pub Inc, 2001.

[64] S. Webb, G. Hartmann, G. Echner, and W. Schlegel. Intensity-modulated radiation therapy using a variable-aperture collimator. *Physics in Medicine and Biology*, 48(9):1223, May 2003.

[65] Steve Webb. Concepts for shuttling multileaf collimators for intensity-modulated radiation therapy. *Physics in Medicine and Biology*, 46(3):637, March 2001.

[66] M. Webster, D. Scanderbeg, T. Watkins, J. Stenstrom, J. Lawson, and W. Song. SU-F-BRA-11: dynamic modulated brachytherapy (DMBT): concept, design, and application. *Medical Physics*, 38:3702, 2011.

[67] Matthew J. Webster, Slobodan Devic, Te Vuong, Dae Yup Han, Justin C. Park, Dan Scanderbeg, Joshua Lawson, Bongyong Song, W. Tyler Watkins, Todd Pawlicki, and William Y. Song. Dynamic modulated brachytherapy (DMBT) for rectal cancer. *Medical Physics*, 40(1):011718, December 2012.

[68] Matthew J. Webster, Slobodan Devic, Te Vuong, Dae Yup Han, Dan Scanderbeg, Dongju Choi, Bongyong Song, and William Y. Song. HDR brachytherapy of rectal cancer using a novel grooved-shielding applicator design. *Medical Physics*, 40(9):091704, August 2013.

[69] M.J. Webster, D.J. Scanderbeg, W.T. Watkins, J. Stenstrom, J.D. Lawson, and W.Y. Song. Dynamic modulated brachytherapy (DMBT): concept, design, and system development. *Brachytherapy*, 10:S33S34, 2011.

[70] X. Wu and D. Z Chen. Optimal net surface problems with applications. *Lecture notes in computer science*, page 10291042, 2002.

[71] Ping Xia and Lynn J. Verhey. Multileaf collimator leaf sequencing algorithm for intensity modulated beams with multiple static segments. *Medical Physics*, 25(8):1424–1434, August 1998.

[72] L. Xing, Y. Chen, G. Luxton, J. G. Li, and A. L. Boyer. Monitor unit calculation for an intensity modulated photon field by a simple scatter-summation algorithm. *Physics in Medicine and Biology*, 45(3):N1, March 2000.

[73] Wenjun Yang, Yusung Kim, Xiaodong Wu, Qi Song, Yunlong Liu, Sudershan K. Bhatia, Wenqing Sun, and Ryan T. Flynn. Rotating-shield brachytherapy for cervical cancer. *Physics in Medicine and Biology*, 58(11):3931, June 2013.

[74] Rui Yao, Alistair K. Templeton, Yixiang Liao, Julius V. Turian, Krystyna D. Kiel, and James C. H. Chu. Optimization for high-dose-rate brachytherapy of cervical cancer with adaptive simulated annealing and gradient descent. *Brachytherapy*, December 2013.

[75] Lei Zhu, Louis Lee, Yunzhi Ma, Yinyu Ye, Rafe Mazzeo, and Lei Xing. Using total-variation regularization for intensity modulated radiation therapy inverse planning with field-specific numbers of segments. *Physics in Medicine and Biology*, 53(23):6653, December 2008.

[76] Lei Zhu and Lei Xing. Search for IMRT inverse plans with piecewise constant fluence maps using compressed sensing techniques. *Medical Physics*, 36(5):1895–1905, April 2009.